A SPECTRAL ANALYSIS OF MICROEARTHQUAKES THAT OCCUR IN THE SOUTHEASTERN UNITED STATES

A THESIS

Presented to

The Faculty of the Division of Graduate

Studies and Research

By

George Eugene Marion

In Partial Fulfillment

of the Requirements for the Degree

Master of Science in Geophysical Sciences

Georgia Institute of Technology

February, 1977

A SPECTRAL ANALYSIS OF MICROEARTHQUAKES

THAT OCCUR IN THE SOUTHEASTERN

UNITED STATES

Approved:

Dr. Leland Timothy Long, Chairman

Dr. G. Lafayette Maynard

Dr. J. Marion Wampler

Date approved by Chairman 02/09/77

ACKNOWLEDGMENTS

This thesis is the result of the efforts of a number of people. The suggestion of the basic idea for this thesis is accredited to Dr. Leland Timothy Long, who also served as the major director of this research. Dr. Long's guidance, support, and advice during the researching and writing of this thesis are greatly appreciated. Dr. G. Lafayette Maynard and Dr. J. Marion Wampler served on my thesis reading committee. Their suggestions were of a constructive nature, which resulted in the clarity and continuity of this thesis being greatly improved. Their efforts are greatly appreciated.

I wish to thank Mr. S. R. (Rutt) Bridges (and whoever helped you) for the Clark Hill Reservoir data that I inherited. Mr. H. E. Denman, Jr. worked on recording the Maryville, Tennessee, data. Other members have been of great help to me by team working the various problems encountered (e.g. field work, computer programs, etc.). They are (alphabetically) Mr. David M. Dunbar, Mr. Stewart A. Guinn, Mr. Helmut Y. A. Hsiao, Mr. J. P. (Jimmy) Marion (my brother), and Mr. W. R. (Bill) Volz. I also wish to thank Mr. Lew Allen Wyatt, Mr. M. G. (Mike) Bailey, and Mr. J. R. (Rick) Lane. These gentlemen are the technicians who built and maintained the equipment described in this thesis. To be completely fair, one must point out that Mr. R. E. (Rick) Deery, Jr. J. K. (Jim) Fulford, Mr. David K. Heller, and the department in general made themselves useful (depending on how one defines the term) by performing the "throwing" tasks (throwing the frisbee, throwing parties, etc.).

A special note is due at this point. I would probably have gone blind and mad from doing the tedious, boring digitizing if my brother had not come over during the summer break and helped me. Also, I must not forget to mention my parents, because they instilled in me, when I was younger, the attitude that is required to do this type of work. Also, I wish to point out that Helmut Y. A. Hsiao and I have worked together on several projects during our studies at Tech, and I have enjoyed working with Helmut in each case.

A note of thanks is in order to Duke Power Company for being so cooperative during the monitoring of the Jocassee Reservoir. The Army Corps of Engineers at the Clark Hill Reservoir is to be thanked, especially for helping coordinate blasts. The Department of Geophysics supplied transportation in the form of both trucks and a power boat.

This research was supported by the United States Nuclear Regulatory Commission, grant number AT(49-24)-0210, and by the National Science Foundation, Earth Sciences Section, NSF grant number DES75-15756. The final draft of this thesis was typed by Peggy Weldon. I especially want to express my appreciation to the Chevron Oil Company, Geophysical Division, for allowing me to take all of the time that I needed to complete this study.

TABLE OF CONTENTS

TABLE OF CONTENTS (Continued)

LIST OF TABLES

LIST OF ILLUSTRATIONS

LIST OF ILLUSTRATIONS (Continued)

SYMBOLS AND ABBREVIATIONS

A	Area of the ruptured surface.
α	P-wave propagation velocity.
b_c	The damping of the L-4C geophone (Appendix A).
b_o	The damping of the L-4C geophone without a shunt (Appendix A).
b_t	The total damping of the L-4C geophone (Appendix A).
β	S-wave velocity.
c	The seismic wave propagation velocity.
CHRA	Clark Hill Reservoir Area.
γ	The order of decay of amplitude with increasing frequency.
db	Decibel.
δx_n	The deviation in the nth measurement.
E	Energy density.
E_R	Energy radiated as seismic waves.
ε	A term used in the correction factor $F(\varepsilon)$.
f_c	The corner frequency, which is also referred to as f_p or f_s when referring to the P- or S-wave corner frequencies.
$F(\varepsilon)$	The correction for partial stress drop.
h	Wave amplitude.
$G(\frac{\omega}{\omega_o})$	The spectral shape function.
H	The Heaviside step function.
I	The integral $\int_0^\infty \left\lvert G(\frac{\omega}{\omega_o})\cdot\omega\right\rvert^2 d\omega$.
θ	Azimuth measured from the normal to the fault plane.

JRA	Jocassee Reservoir Area.
k	The constant of proportionality for the f_c to r relation.
K	The total number of measurements.
m	Mass.
M_L	Local magnitude.
M_o	Seismic moment.
MTA	Maryville, Tennessee, Area.
μ	Shear modulus.
N	The correction factor for the conversion of waveforms.
π	Pi.
Q	The quality factor used in determining seismic amplitude attenuation as a function of distance.
Q_p	P-wave Q-value.
Q_s	S-wave Q-value.
r	The effective fault radius.
R	The hypocentral distance.
R_c	The coil resistance of the L-4C geophone.
R_s	The shunt resistance.
$\mathcal{R}^{ps}_{\theta\phi}$	The radiation pattern correction.
ρ	Mass density.
s	Standard deviation.
S_v	Fractional standard deviation of a product.
σ	Effective stress. It is related to the amount of stress available to produce rupture and accelerate the sides of a fault.
$\Delta\sigma$	Effective stress drop. It is the amount of effective stress relaxed by the faulting process. In the case of a complete stress drop, the effective stress drop equals the effective stress.

t	Time in the near-field.
T_o	The driving shear force.
τ	Time in the far-field.
U	Particle displacement.
$\dot{U}$	Particle velocity.
$\ddot{U}$	Particle acceleration.
$\bar{U}_d$	Average fault displacement.
U_{max}	Maximum fault displacement.
V_r	Rupture velocity.
ϕ	Azimuth measured in the plane of the fault.
ω	Angular frequency.
Ω_{ps}	Spectral amplitude (also referred to as spectral density).
x	Distance along the X-axis.
Y	A convolution used in the energy equations.

SELECT DEFINITIONS

Azimuth	The orientation of the fault plane in three-dimensional space.
Far-field	Distances large with respect to the dimensions of the ruptured area.
Fault	The immediate rupture zone.
Origin	The point of first rupture.
P-wave	A longitudinal wave.
Seismic pulse	The energy envelope as recorded by seismic instruments.
Subsonic	Rupture velocity less than the S-wave velocity.
S-wave	A transverse body wave.
Transonic	Rupture velocity greater than the S-wave velocity.

SUMMARY

Records of the vertical component of 93 microearthquakes are used to calculate 165 body-wave displacement spectra. These microearthquakes were recorded on calibrated portable magnetic tape seismic recorders at hypocentral distances of 0.7 km to 20.0 km while monitoring ground motions near three epicentral areas. The Clark Hill Reservoir area and the Jocassee Reservoir area represent seismically active regions of the Piedmont Province with the former area spectra representing shallow focus microearthquakes occurring in the epicentral area of the $M_L = 4.8$ earthquake of August 2, 1974 and the latter area spectra representing microearthquakes probably triggered by reservoir impounding. Microearthquakes recorded during the immediate aftershock sequence of the $M_L = 4.6$ earthquake of November 30, 1973, which occurred near Maryville, Tennessee, are used to represent microearthquakes possibly occurring in the sedimentary rocks of the folded Appalachian Mountains. The displacement spectra are interpreted in terms of distinct properties by comparison to curves derived from theoretical considerations of source models. Displacement spectra of the Clark Hill Reservoir area and the Jocassee Reservoir area typically show an ω^{-3} amplitude decay at high frequencies; sharp, well defined spectral corners often at frequencies greater than 100 Hz; and P-wave spectral corner frequencies higher than corresponding S-wave spectral corner frequencies. The Maryville, Tennessee, area spectra typically show an ω^{-2} to $\omega^{-2.5}$ amplitude decay at high frequencies, rounded spectral corners, and S-wave spectral corner frequencies higher than P-wave spectral corner frequencies. The Clark Hill Reservoir area and the Jocassee Reservoir area spectra show properties which suggest a transonic model (i.e. effective rupture velocity greater than the S-wave velocity) while the properties of the Maryville, Tennessee, area spectra are best described by a subsonic model. Values of the effective fault displacement, the effective fault radius, the effective stress drop, the seismic energy, and a local magnitude are also calculated. Quality factors of $Q_p = 500$ and $Q_s = 250$ are determined for the Clark Hill Reservoir area by applying the spectral ratio method to local quarry explosion spectra. Errors and uncertainties in the displacement spectra are related to the choice of the portion of the seismic trace digitized and to the response of the instruments used.

CHAPTER I

INTRODUCTION

Although the study of large earthquakes is an ancient science, the study of microearthquakes ($M_L \leq 3$) is a relatively new science which began only after the development of portable seismographs capable of being placed close to an earthquake epicenter. The most common instrument used during close-in field monitoring of earthquakes is a portable, helical-recording, smoked-paper seismograph. However, this instrument does not lend itself to a spectral analysis of the data because the trace is typically operated with a drum speed of 10- to 120-mm/min which is too slow a recording rate to resolve the high frequencies encountered with southeastern United States microearthquakes. The computation of microearthquake displacement spectra became practical only after the development of portable magnetic-tape seismic recorders capable of recording frequencies in the seismic band. Microearthquake data, recorded on magnetic-tape seismic recorders, has been available at Georgia Tech since 1973.

The theory of seismic displacement spectra received only slight attention until the 1960's when technological advances made the application of the theory more practical. Because of the extreme complexity of the analytical solution to the three dimensional dynamic case, theoreticians were effectively forced to base their models on a greatly simplified two dimensional case, which greatly restricted the applicability of the theories. However, developments in computer technology within the last decade now make possible the study of three-dimensional models by use of numerical methods. As a result, the last couple of years have witnessed a veritable flood of new spectral theories and studies. Thus, a need exists to review recent theoretical developments and to apply these new methods to the microearthquakes which occur in the southeastern United States for the purpose of determining information on the processes that cause earthquakes. This study uses microearthquakes because they are much more common than are larger earthquakes.

The objective of this thesis is to calculate and catalogue body-wave displacement spectra (both P- and S-wave) for the microearthquakes recorded in the Southeast, to review recent theoretical developments, and to discuss implications of the observed spectral data in terms of the theory presented. This study is significant because it is the first attempt at a major spectral study of the microearthquakes which occur in the southeastern United States.

CHAPTER II

DATA REGIONS

The three data regions for this study are the Clark Hill Reservoir area (CHRA), the Jocassee Reservoir area (JRA), and the Maryville, Tennessee, area (MTA) (Figure 1).

The Clark Hill Reservoir Area

The epicentral area of the $M_L = 4.8$ earthquake of August 2, 1974, in the CHRA comprises the first data region of this study (Figure 2). The epicenter is located in the northern portion of the Clark Hill Reservoir area. The reservoir is located along the Georgia-South Carolina border on the Savannah River south of the Hartwell Reservoir and approximately 50 kilometers north of August, Georgia. The definitive study of the aftershock sequence of the August 2, 1974, earthquake was prepared by Bridges (1975). Careful attention has since been paid to the activity of the region in general and to the epicentral area in particular. The CHRA is located in the Piedmont Province. A petrographic study of a portion of the area has been prepared by Paris (1976). A geologic-geophysical study of the area was prepared by Denman (1974), and a geologic-geophysical study of the immediate epicentral area has been prepared by Scheffler (1976). The microearthquake data obtained from this region are important because they provide information on microearthquakes which occur in the crystalline rocks of the Southeast. The data for the displacement spectra were obtained during numerous monitoring sessions of the area.

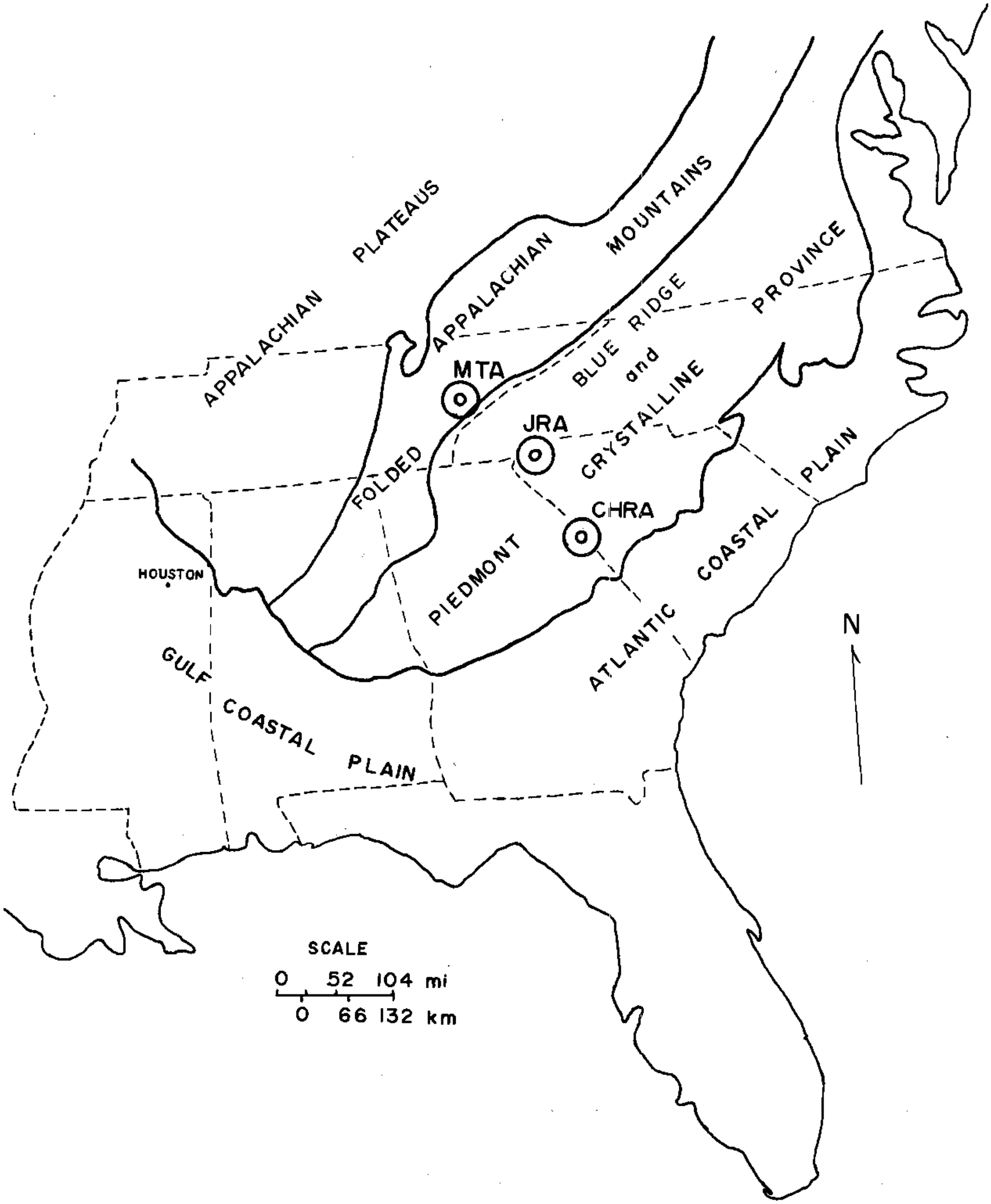

Figure 1. Regional Map of the Southeastern United States (Raisz, 1970).

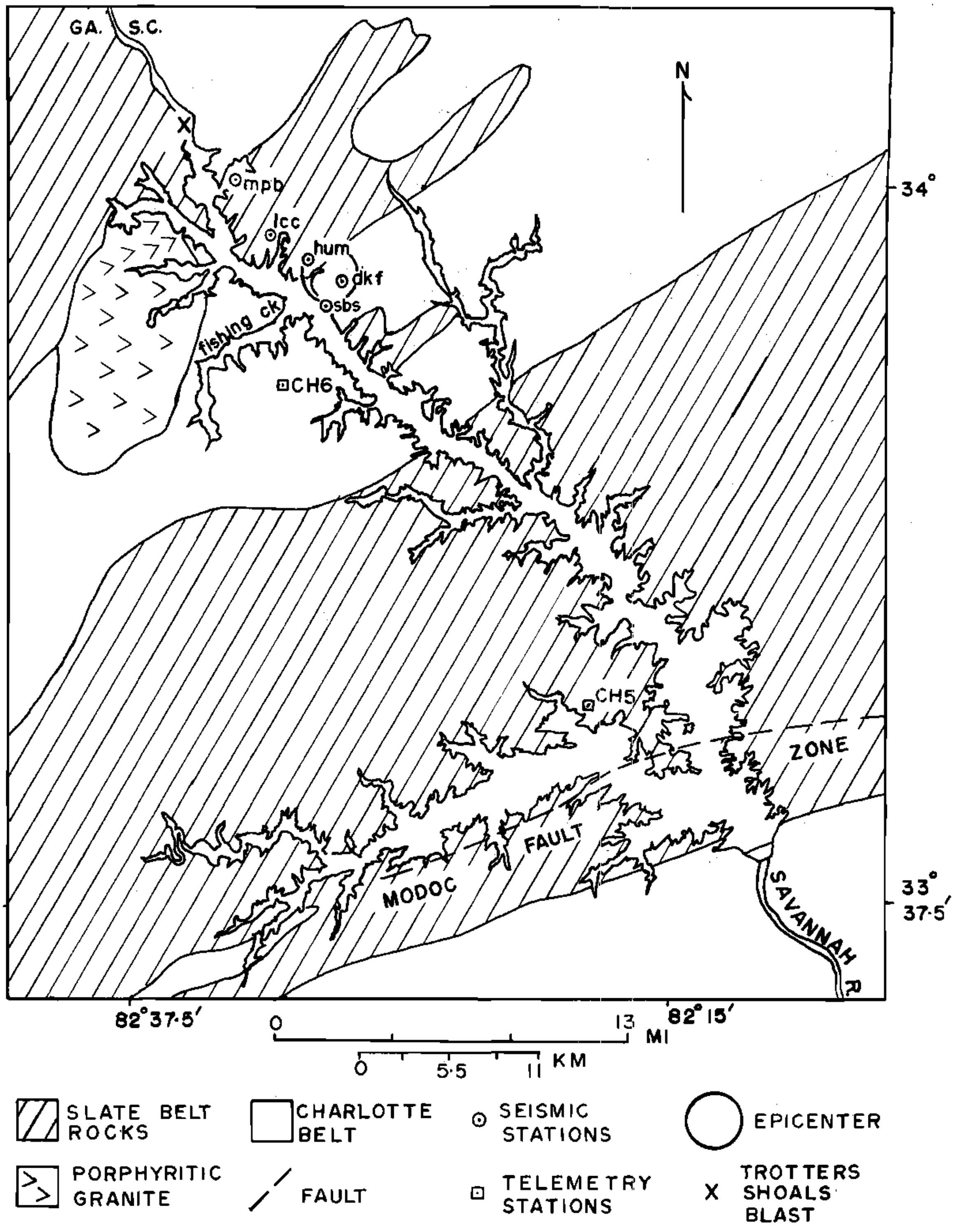

Figure 2. The Clark Hill Reservoir Area (Chowns, 1976).

The Jocassee Reservoir Area

The JRA comprises the second data region of this study (Figure 3). The reservoir is located in northwestern South Carolina on the Keowee River near the South Carolina-North Carolina border. The dam is constructed on the Henderson granite gneiss southeast of the Brevard Zone. The majority of the microearthquakes are centered near the deepest portion of the reservoir which has a depth of 125 meters. The reservoir was filled during the winter of 1974-1975. Microearthquake monitoring began in November, 1975. Law Engineering Testing Company (in conjunction with the University of South Carolina) was contracted by Duke Power Company to provide continuous close-in monitoring of the area from December, 1975 to July, 1976. Georgia Tech provided additional monitoring on three occasions for the purpose of obtaining data for the calculation of displacement spectra. The data obtained from this region are an important addition to the study because the earthquakes are probably induced by reservoir impounding (Fogle et al., 1976).

The Maryville, Tennessee Area

The MTA (Figure 4) is located approximately 25 kilometers south of Knoxville, Tennessee, and is the epicentral area of the $M_L = 4.6$ earthquake of November 30, 1973 (Bollinger et al., 1976). A period of approximately 36 hours of close-in aftershock monitoring was provided by an expedition from Georgia Tech. The epicentral area is located in the Valley and Ridge Province. The predominant surface rocks of the area are dolomites, limestones, and clay shales. The region includes numerous Paleozoic thrust faults which strike northeast. The MTA data set is important to this study because it provides information about microearthquakes which

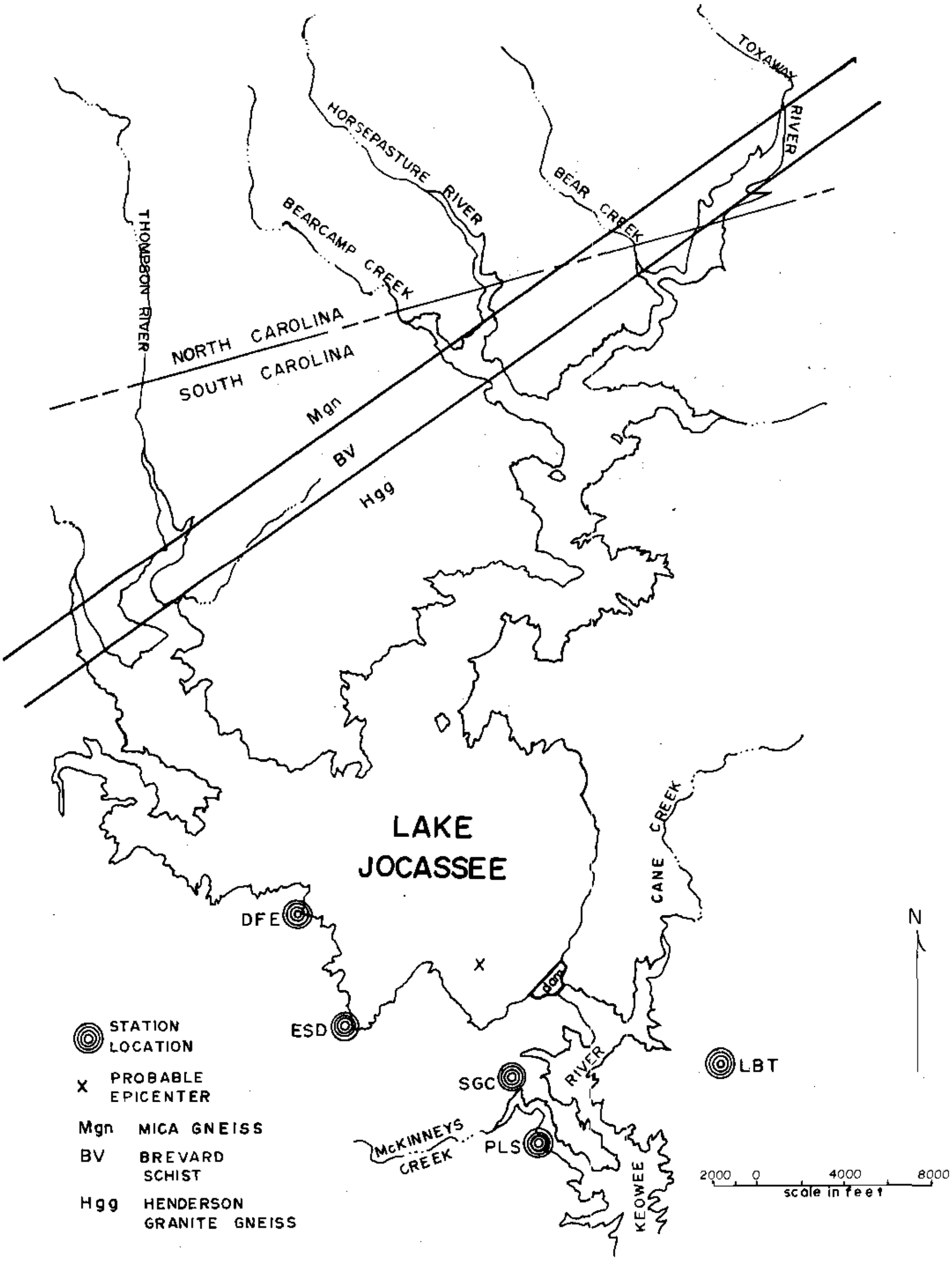

Figure 3. The Jocassee Reservoir Area.

(Geology Is from Overstreet and Bell, 1961.)

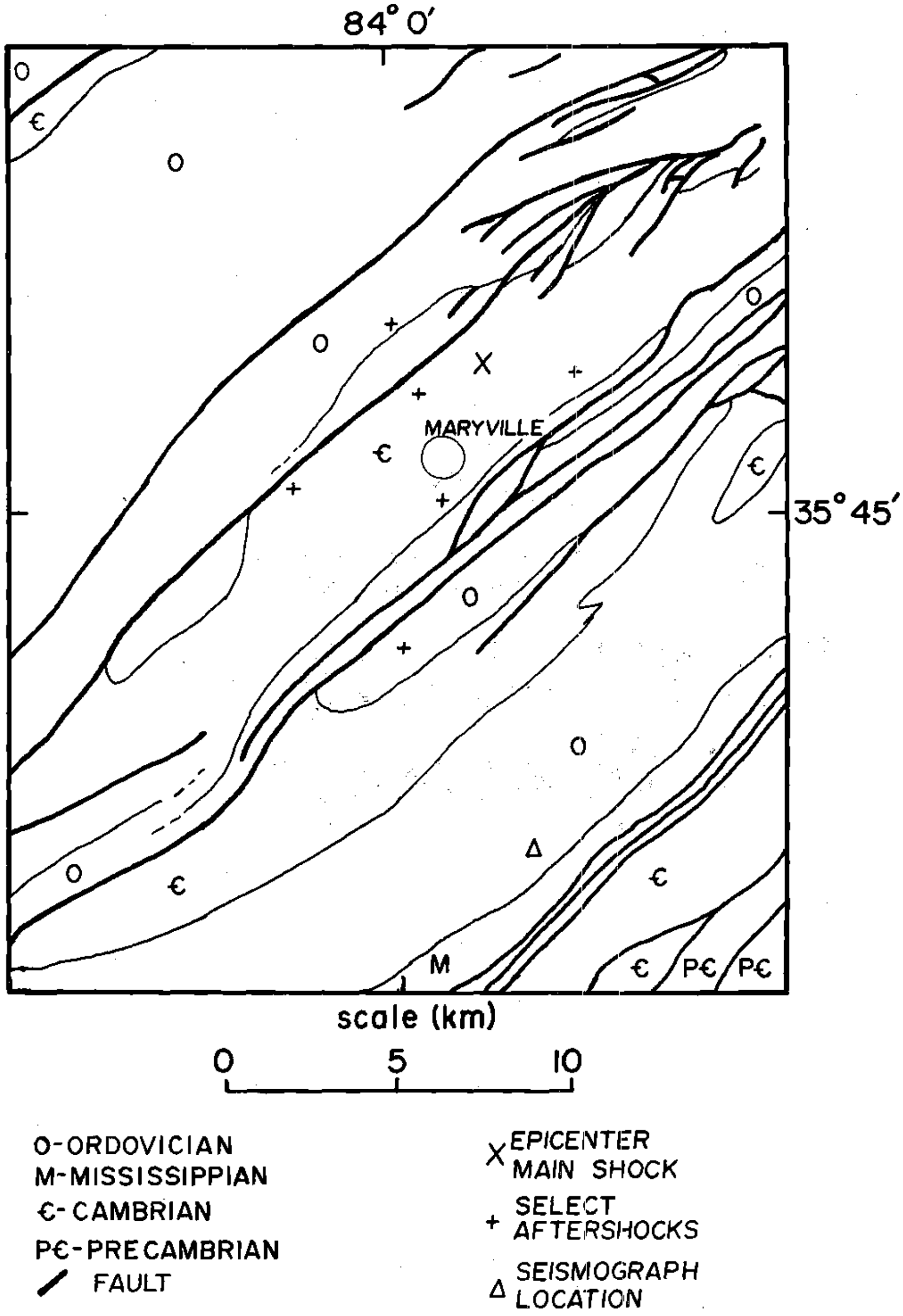

Figure 4. The Maryville, Tennessee, Area. (Basic Map Is from Bollinger et al., 1976.)

may have occurred in the sedimentary rocks which overlie the crystalline basement rocks.

CHAPTER III

INSTRUMENTATION

This study was possible only because instrumentation capable of resolving seismic spectra were available. The instruments were designed and constructed at the School of Geophysical Sciences at Georgia Institute of Technology. The instrumentation used for spectral studies consists of a portable, magnetic tape, seismic recorder for field operations and a playback system for laboratory operations. The instrumentation and the calibration process are discussed in this chapter.

Field Instrumentation

The portable, magnetic tape, seismic recorder system is composed of a tape deck, a geophone-amplifier system, a WWV radio receiver, and a signal mixing and filtering unit (Figure 5). The tape deck is a Sony model TC-800B reel-to-reel recorder which has been modified to operate from an external twelve volt battery. To maximize the duration of recording, the unit is operated at 15/16 ips with 0.25 mil magnetic tape. This combination allows approximately eight hours of continuous recording between record changes. The geophone is a 15 Hertz exploration geophone which has been modified by the installation of a X1000-gain amplifier inside the geophone case. The seismic signal, which contains very little or no information above 500 Hertz, is recorded without filtering. The WWV radio signal provides second and minute pulses which are returned with sufficient volume to allow the determination of the exact time. The

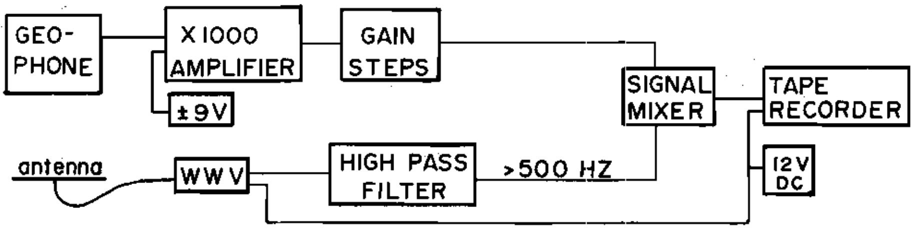

Figure 5. The Field Instrumentation.

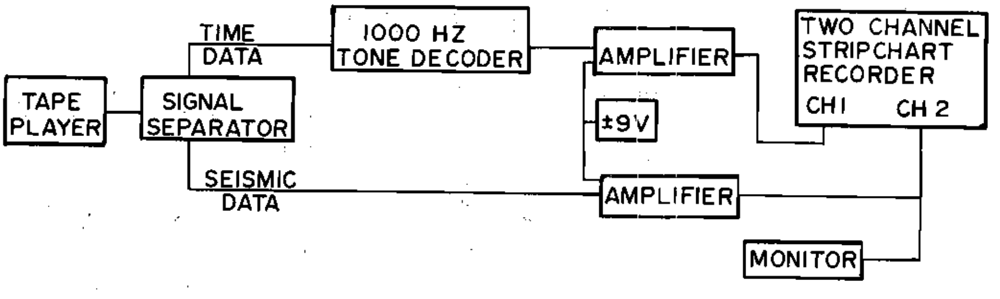

Figure 6. The Laboratory Instrumentation.

radio signal is filtered to remove frequencies below 500 Hertz. Consequently, the seismic and WWV signals can be mixed without significant interference on a single channel.

Laboratory Instrumentation

The laboratory playback system consists of a tape deck from one of the field units, a signal separator, a high-speed stripchart recorder, a smoked paper helical monitor recorder, and a second calibrated tape unit (Figure 6). The tape deck is used to play tapes through the signal separator system. The signal separator recreates the seismic signal and decodes the WWV signal into second and minute pulses. An option for a mixed output which superimposes the decoded WWV signal onto the seismic signal has been built into the system. The high-speed strip-chart recorder has a maximum paper speed of 125 mm/sec. A second calibrated tape deck is used to record filtered events onto a catalogue tape for future reference. Examples of stripcharts are presented in Appendix I.

Calibration of the Total System

For purposes of calibration, the total system is grouped into the following subsystems:

a) the geophone-amplifier subsystem.
b) the portable tape deck subsystem.
   1) recording response (includes the signal mixer unit)
   2) playback response
c) the signal separator stripchart recorder subsystem.

The response of each subsystem is determined independently. A suspended platform is used to calibrate the geophone-amplifier subsystem, the response of which is presented in Figure 7. The tape recorder subsystem is adjusted to unit calibration, which means that the output voltage equals

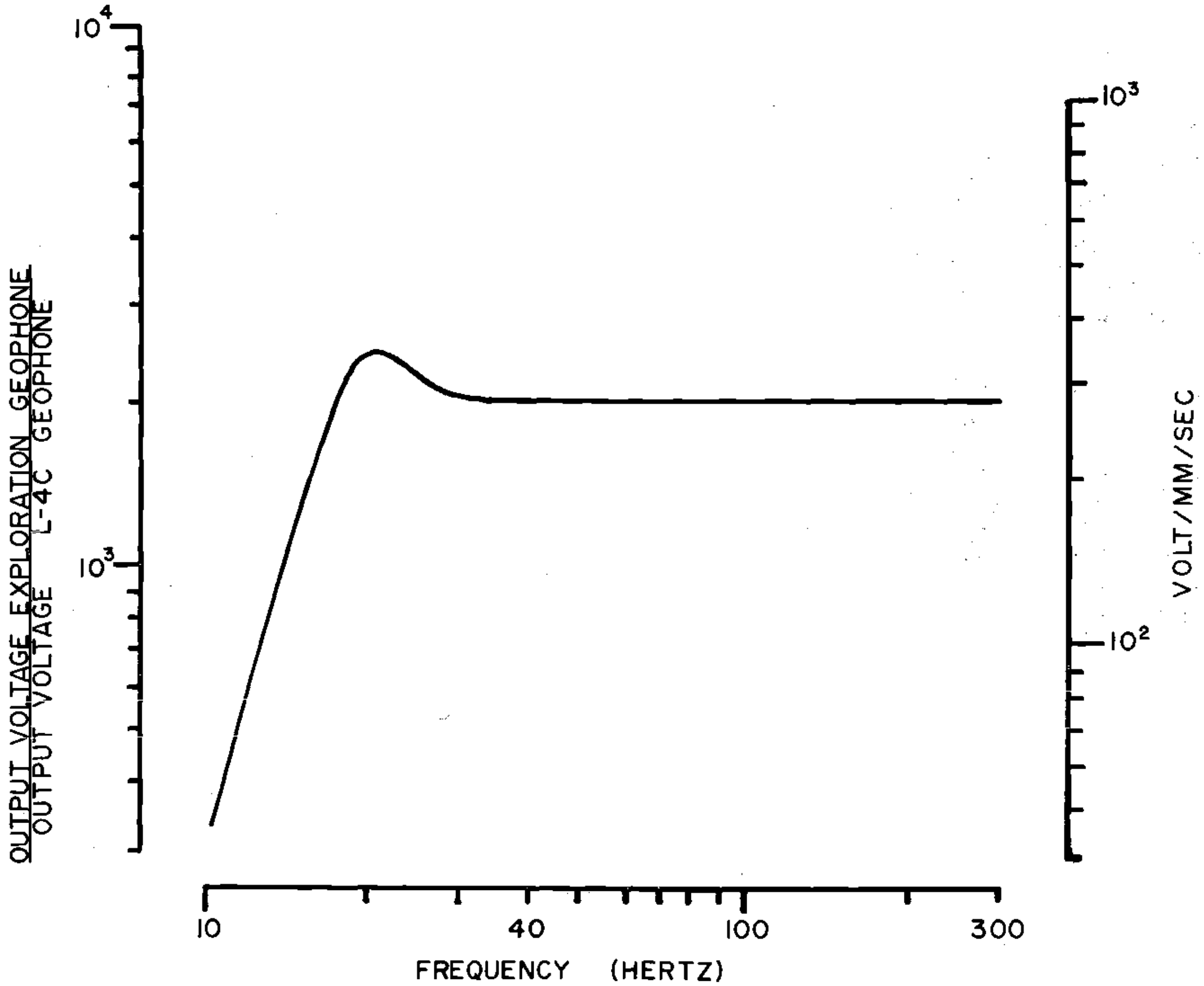

Figure 7. The Exploration Geophone - Amplifier Subsystem Velocity Response.

the input voltage at 100 Hertz. The response of this subsystem is shown in Figure 8. Figure 9 presents the response of the signal separator-stripchart recorder subsystem. The combination of the subsystem response curves gives the particle velocity response for the total system (Figure 10). The particle displacement amplitude response curve (Figure 11) for the total system is, de facto, obtained by multiplying the velocity response curve by the angular frequencies. This description has over-simplified the relationship between a velocity response and a displacement response. Additional subsystem response curves, as well as a detailed accounting on the calibration procedure, are presented in Appendix A. An error analysis of the process is given in Appendix C.

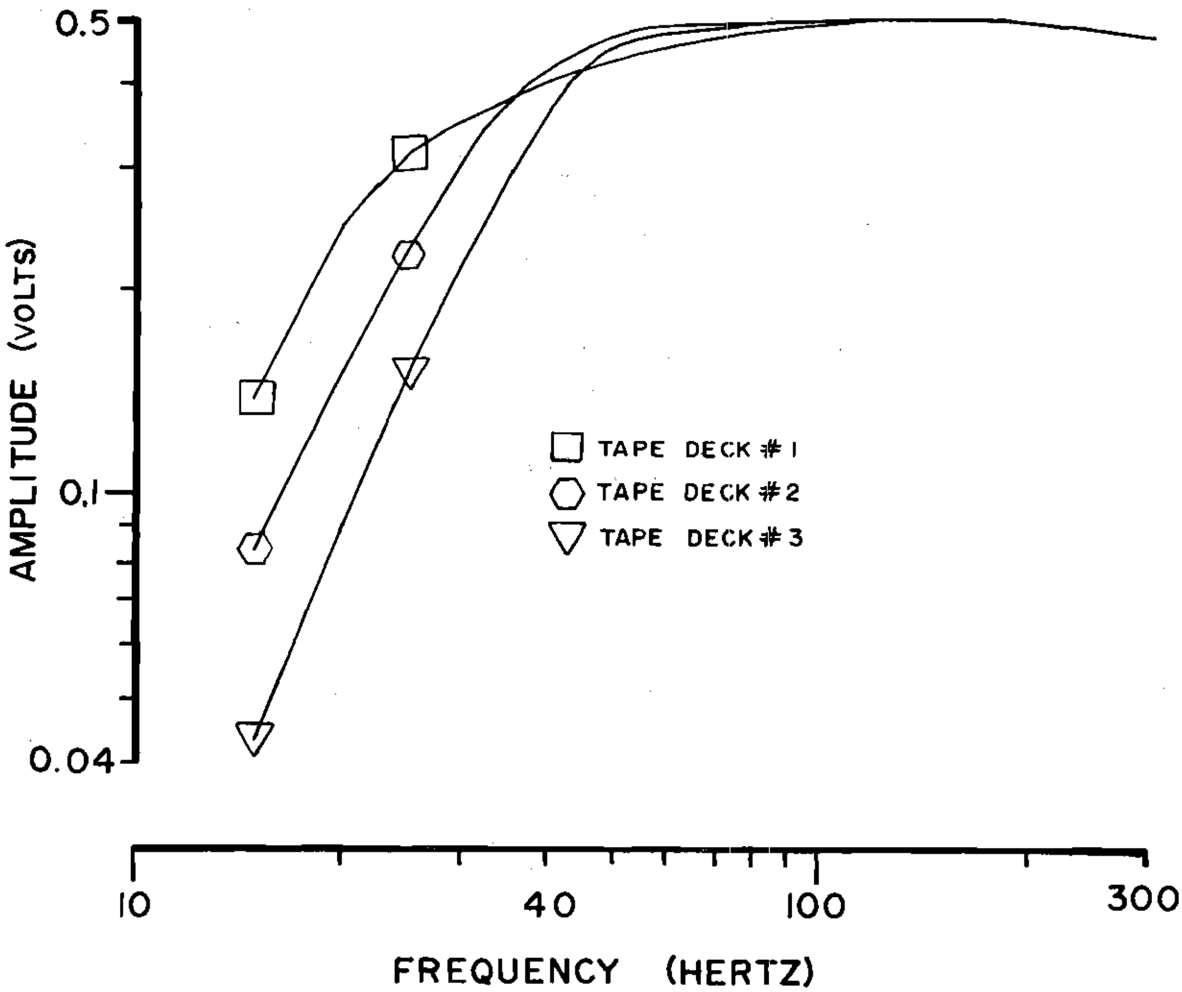

Figure 8. The Tape Recorder Subsystem Amplitude Response. (The curves show the maximum deviation between instruments.)

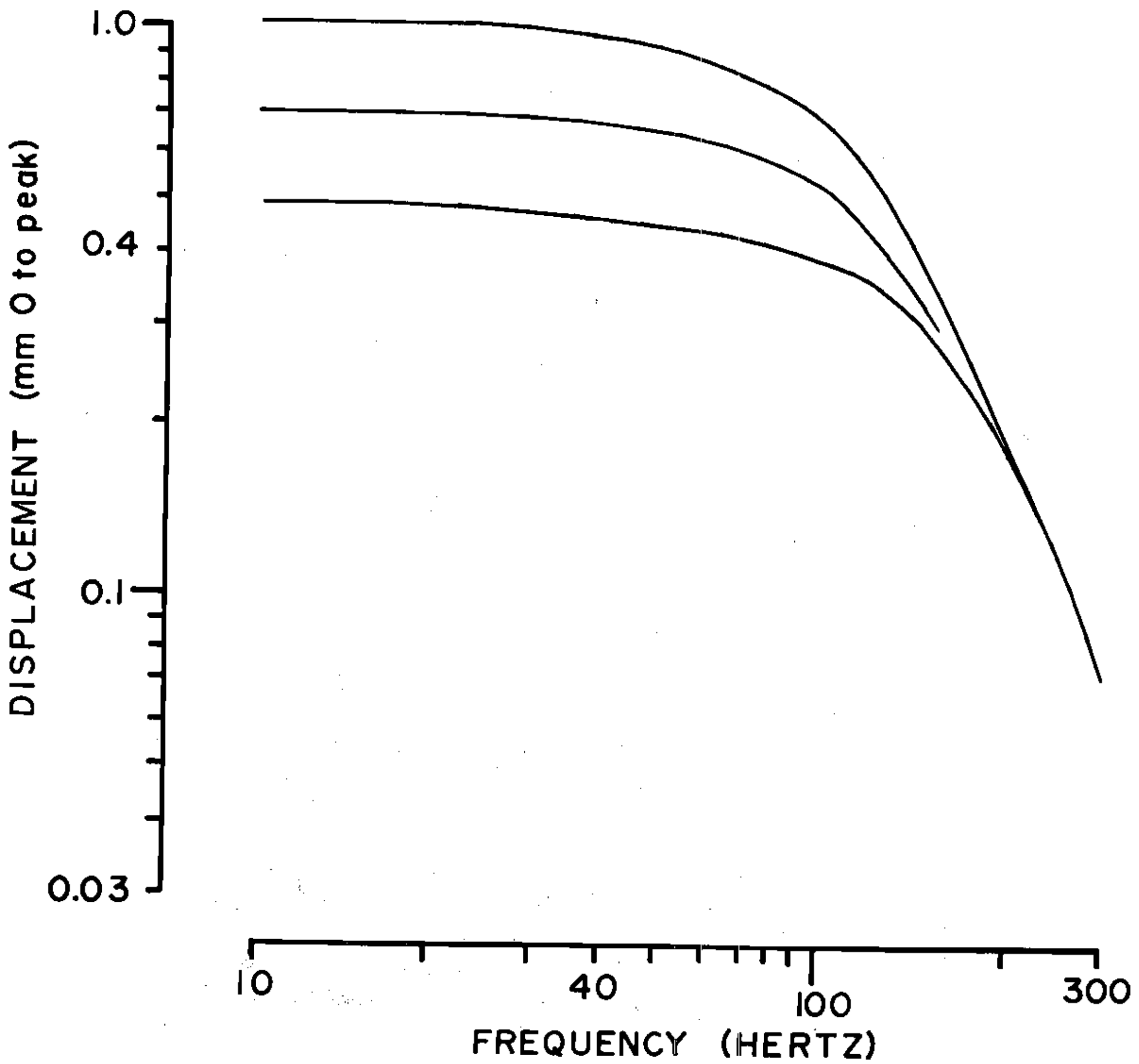

Figure 9. The Signal Separator - Stripchart Recorder Displacement Response.

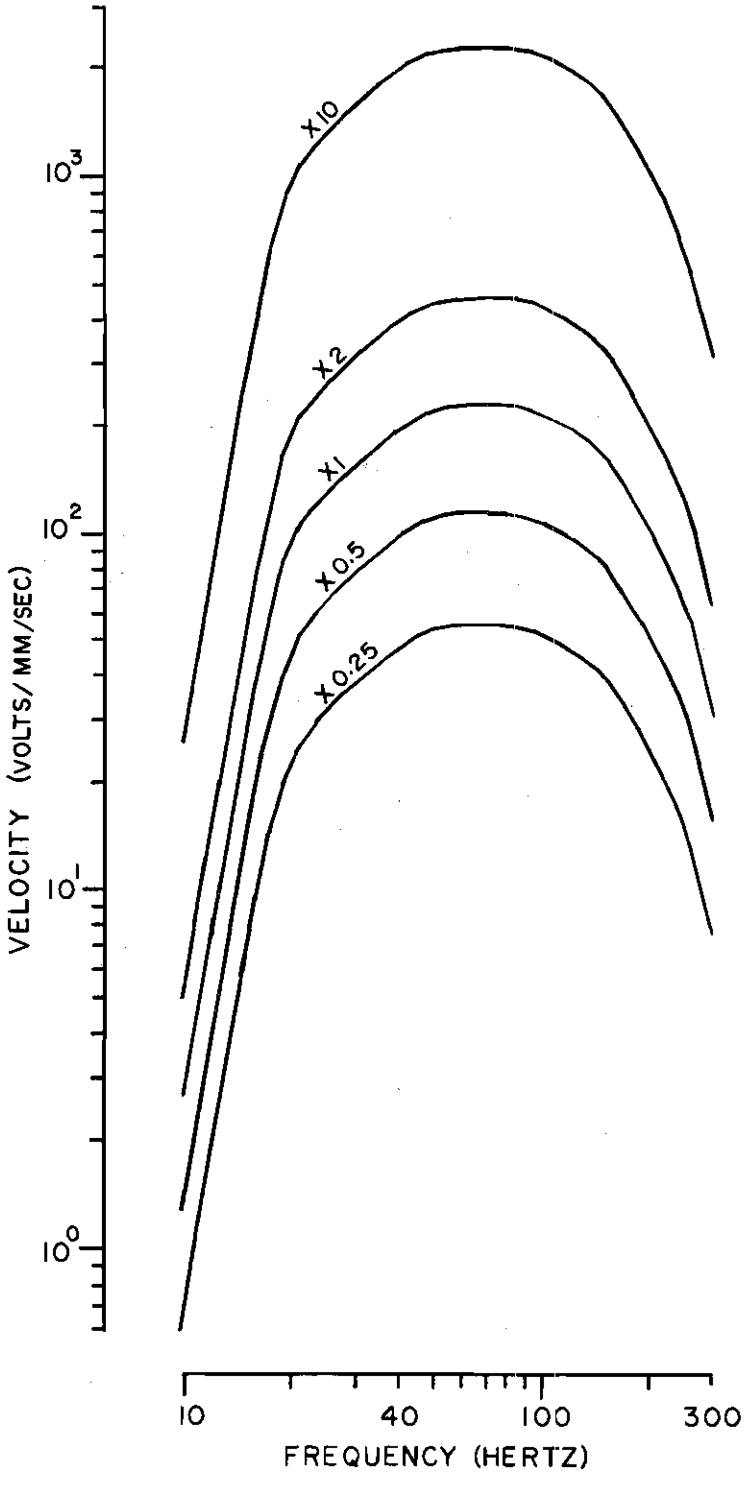

Figure 10. The Velocity Response of the Total System. (The different curves apply for different gain settings of the geophone-amplifier system.)

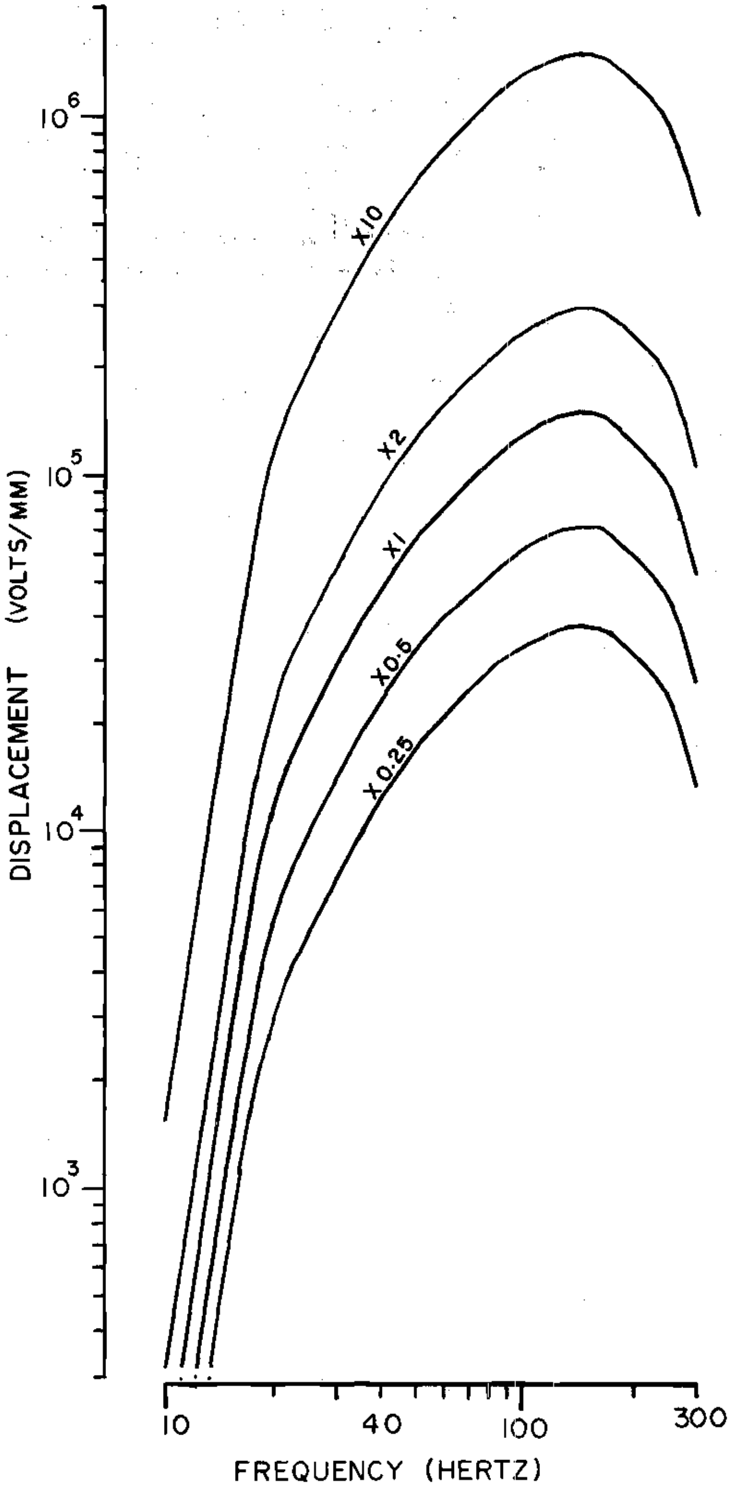

Figure 11. The Displacement Response of the Total System. (The different curves apply for the different gain settings of the geophone amplifier.)

CHAPTER IV

PROCEDURE

Field Procedure

An optimum array used in obtaining microearthquake data involved the deploying of three tape units in a three station close-in array and smoked paper units in a larger array which enclosed the tape units (Figure 12). The smoked paper units served as monitors for the tape units as well as providing a means of improving the locations of epicenters. Only data obtained from the magnetic tape units could be used for spectral studies. Field expeditions were typically for periods of three to five days. A telemetry system installed in the CHRA served as a monitor of the activity level. A period of relatively high activity was sufficient incentive to justify a field monitoring session; as was news of the initiation of activity at the Jocassee Reservoir. A monitoring session was terminated when the field technician decided that the seismic activity had fallen below a profitable level as determined by examination of the smoked paper monitors. Results of field trips are presented in Appendix F.

Laboratory Procedure

The purpose of the laboratory procedure is to transcribe the data onto a visible record and to preserve the data in a format that will be useful in the future. In order to search for seismic events, the magnetic tapes are played through the playback system and the seismic data recorded on a helical smoked paper recorder. When an event is found,

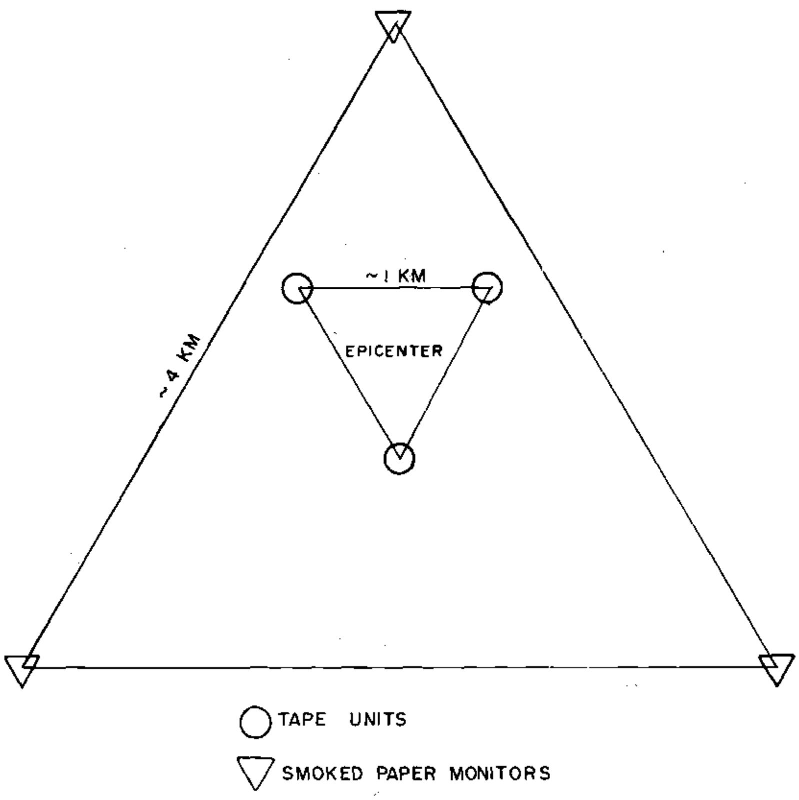

Figure 12. An Ideal Field Array.

the event is replayed onto a two-channel high-speed stripchart recorder. At the same time that the event is played onto the strip chart recorder, one may also play the event onto another tape recorder for later reference and analysis. All events from an expedition are played onto one tape and catalogued as to their location on the tape by the tape footage.

The data are digitized to facilitate the computation of displacement spectra. The Fourier integral transformation assumes that the function is continuous and infinitely periodic. However, because a seismic wave trace is digitized at a finite interval, frequencies higher than the Nyquist frequency will introduce lower frequencies into the spectrum if they have sufficient amplitude. This is called aliasing. To minimize aliasing, the digitizing interval is chosen sufficiently small such that the trace is effectively continuous. The portion of the wave trace digitized is chosen as nearly periodic as possible in order to avoid the presence of a step function when the trace is repeated with itself during the Fourier transformation. The wave trace is digitized by measuring amplitudes at equal time intervals. However, the time interval chosen varies from one waveform to the next depending upon the point spacing required to resolve both the highest frequency and all the peaks. An alternative method is to measure amplitudes at unequal time intervals and interpolate by using a linear or cosine function between points. In either case, amplitude and time are measured in convenient units and are corrected to units of millimeters and seconds during the spectral calculation. For this thesis, waveforms were always digitized with at least five points per wavelength. Nine points per wavelength were used whenever resolution required. The Nyquist (or folding) frequency is the maximum frequency resolvable and is defined as being one-half the digitizing rate (Kanasewich, 1975). This study used a maximum digitizing rate of 2940 counts per second, which gives a Nyquist frequency of 1470 Hertz and a frequency of 368 Hertz for the case of nine points per wavelength, indicating that the resolution available is more than sufficient. The digitized data are stored in the form of punched cards for future use. Thus, the data are preserved in three forms: magnetic tape, stripchart trace, and punched cards.

CHAPTER V

RESULTS

Calculation of the Spectra

Earth motion during an earthquake is a transient phenomenon which can contain energy at all frequencies. The information contained in the wave trace can be presented in many formats. The format chosen for this study is a plot of log-displacement amplitude versus log-frequency. A seismogram trace is prepared for the calculation of a displacement spectrum by fitting a least squares best-fit straight line to the digitized data. This line defines a base line which is subtracted from the value of the amplitude of each point. The magnitude of each residual is Fourier transformed into the frequency domain and corrected for the displacement response of the total system. Amplitude in the time domain has units of millimeters, which when transformed, becomes spectral amplitude (also referred to as spectral density) with units of mm-sec.

Presentation of the Spectra

The spectra presented in this study have been calculated from microearthquake data recorded on calibrated instrumentation and are limited only by the errors related to the digitizing process (e.g. noise, truncation, etc.) and errors in the corrections applied to the original data (e.g. instrument response and base line fit). In each case, as much of the phase (P or S) was digitized as was reasonably possible to avoid loss of information. The spectra are presented independent of interpretation, because once interpretation is applied to the data, they are no longer free from possible bias and misinterpretation. For ease of comparison, identification information and a reconstructed wave trace of the digitized data used to calculate the spectrum are included with each plot. Ergo, the displacement spectra are presented as the principal results of this study. A representative sample of the displacement spectral plots are presented in the main text (Figures 13-20) with the majority of the spectra being presented in Appendix G.

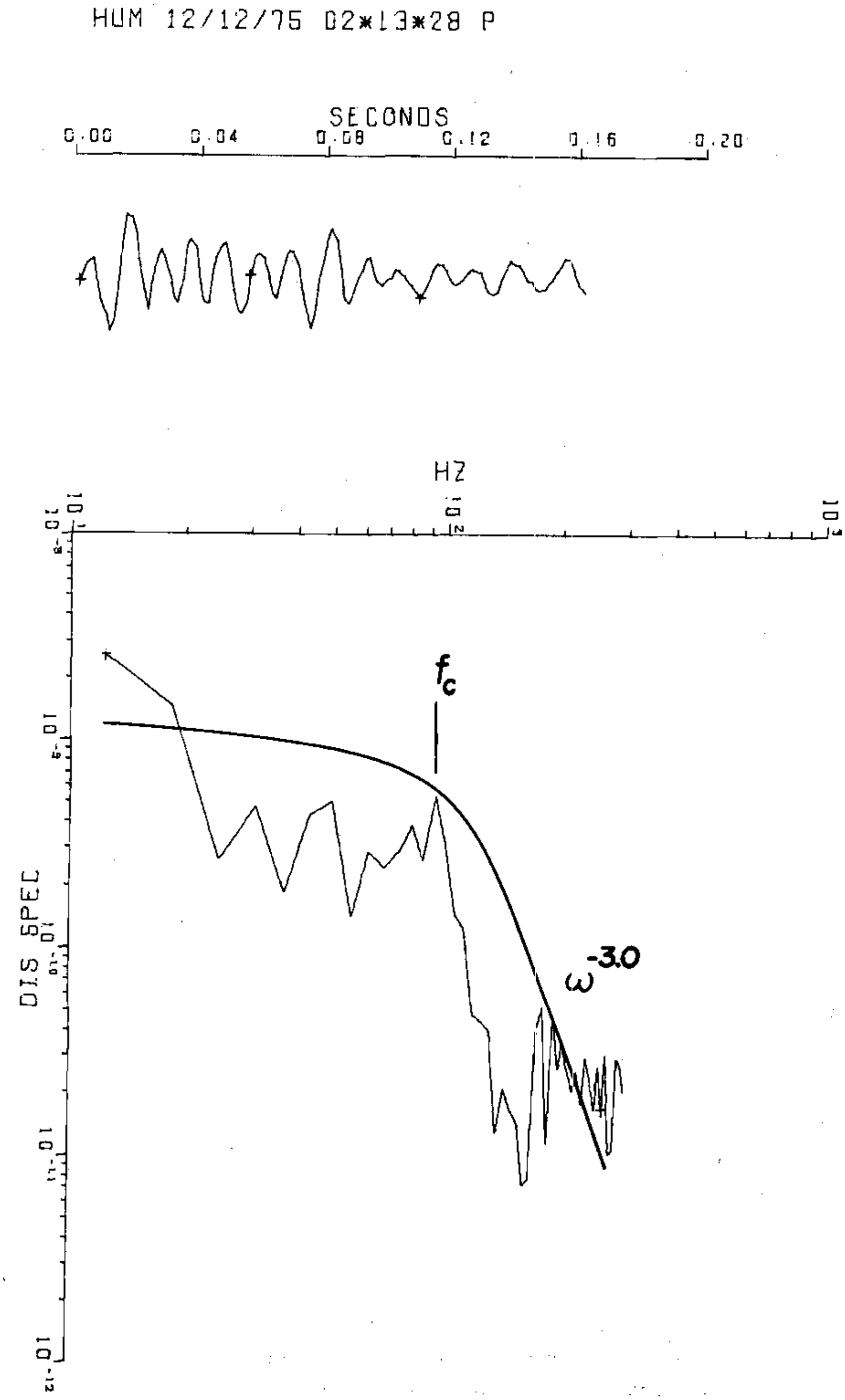

Figure 13. A Representative CHRA P-wave spectrum. (The title gives the station (HUM), the date (12/12/75), and the Universal Coordinated Time (02:13:28).) (This is number 56 of Table 1.)

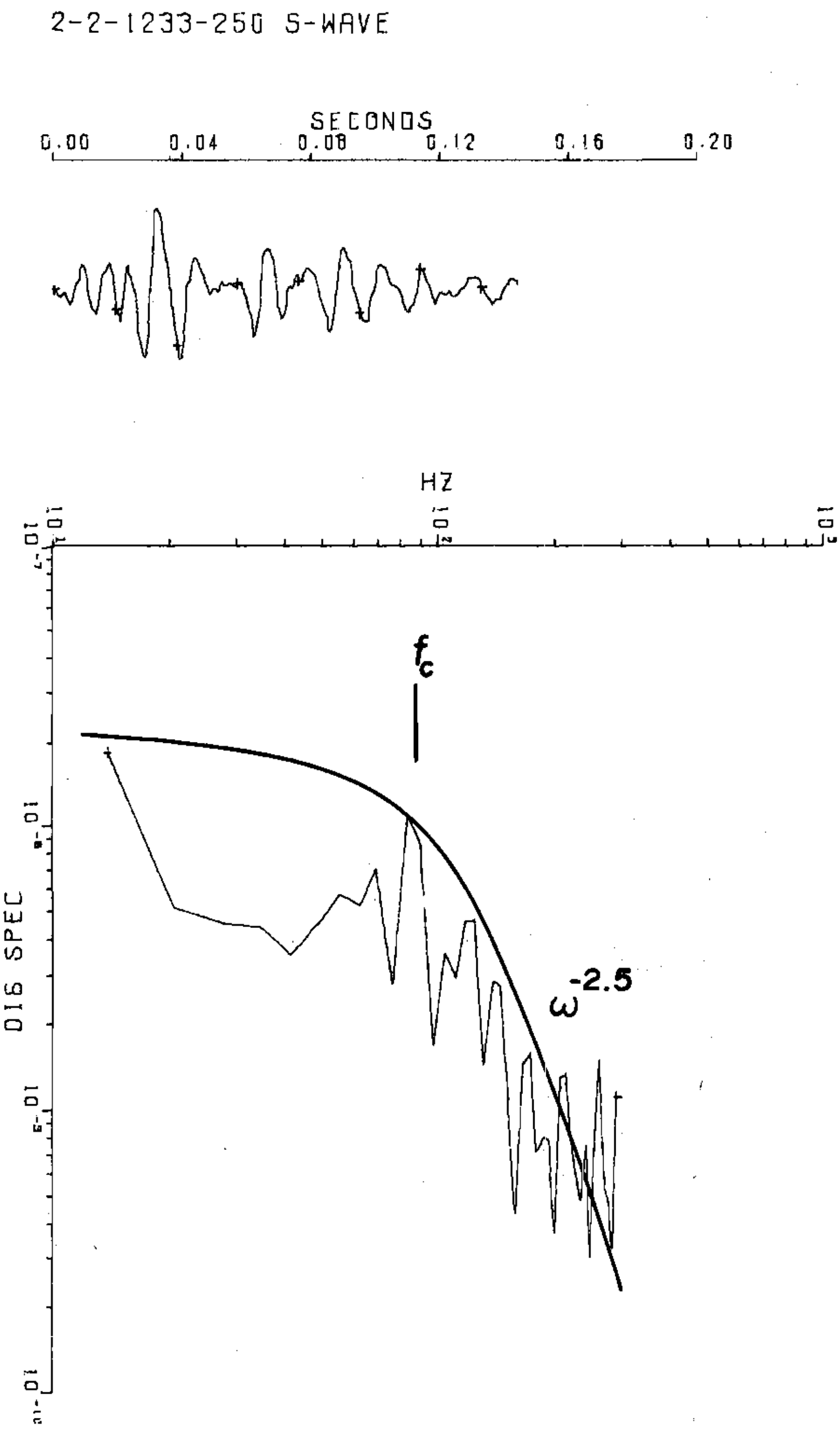

Figure 14. A Representative CHRA S-wave Spectrum. (The title refers to tape number two, side two, footage 1233, and record speed of 250 mm/sec.) (This is number 75 of Table 1.)

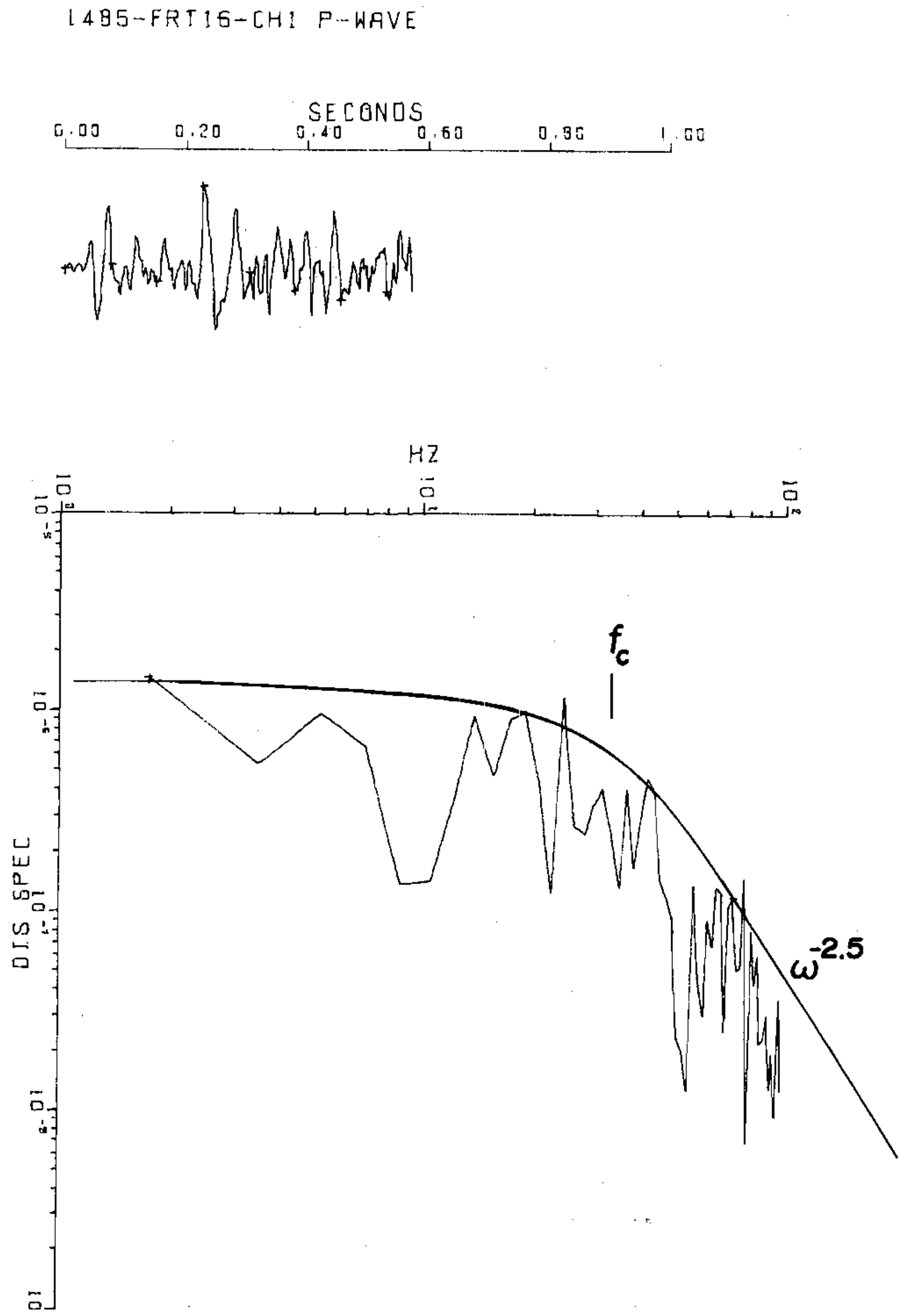

Figure 15. The P-wave Spectrum of a Relatively Large CHRA Microearthquake. (This is number 150 of Table 1.)

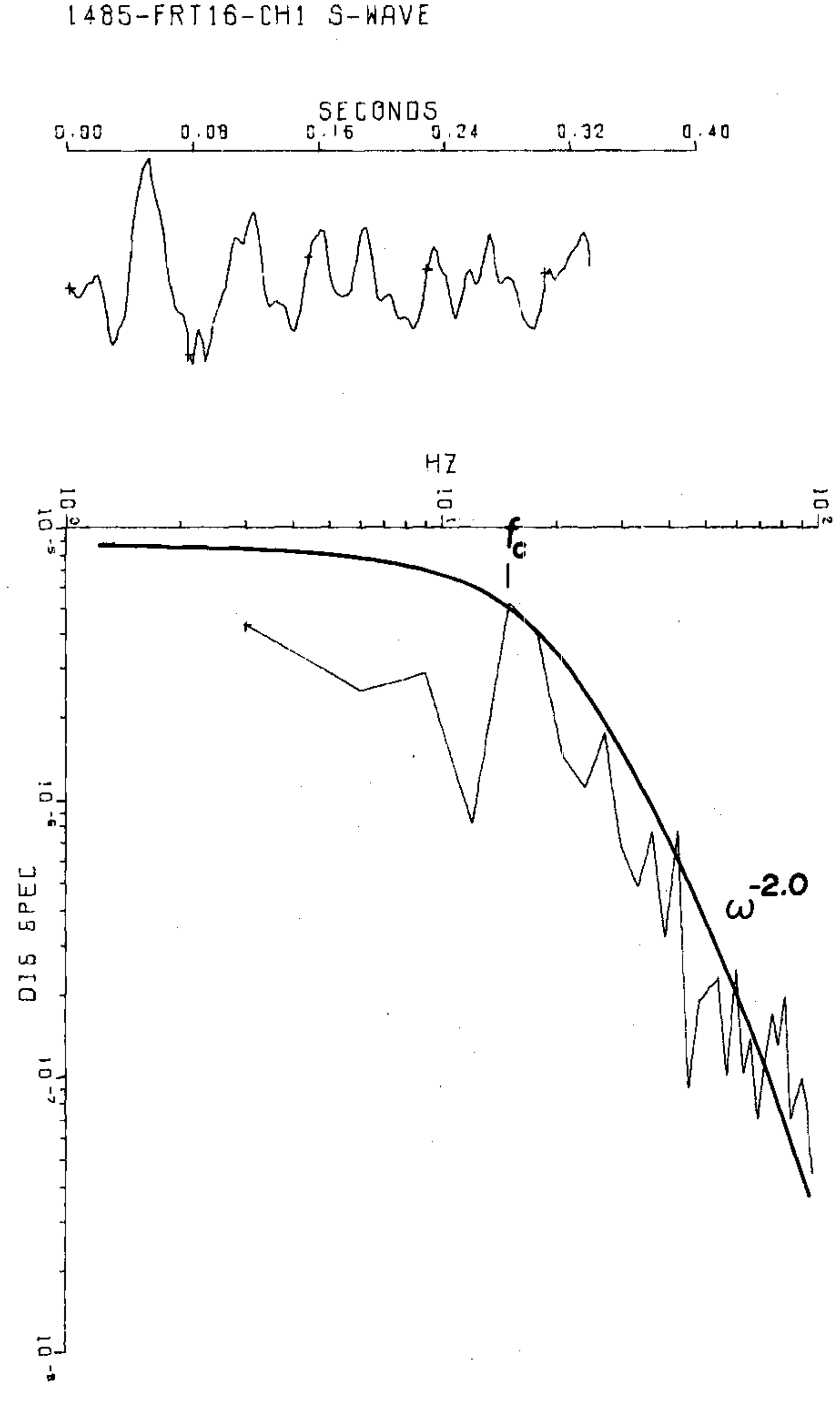

Figure 16. The S-wave Spectrum of a Relatively Large CHRA Microearthquake. (This is number 151 of Table 1.)

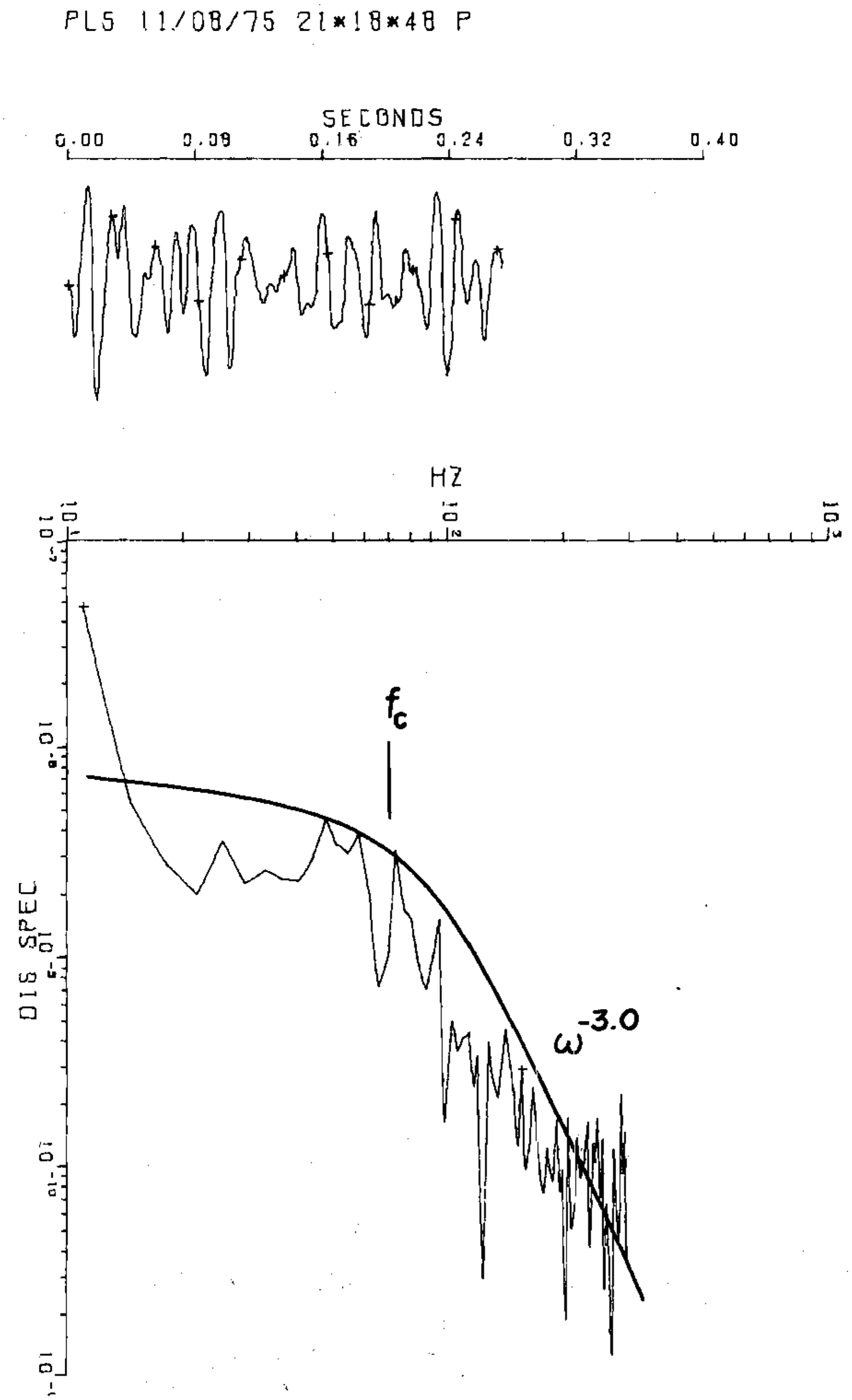

Figure 17. A Typical JRA P-wave Spectrum. (This is number 11 of Table 1.)

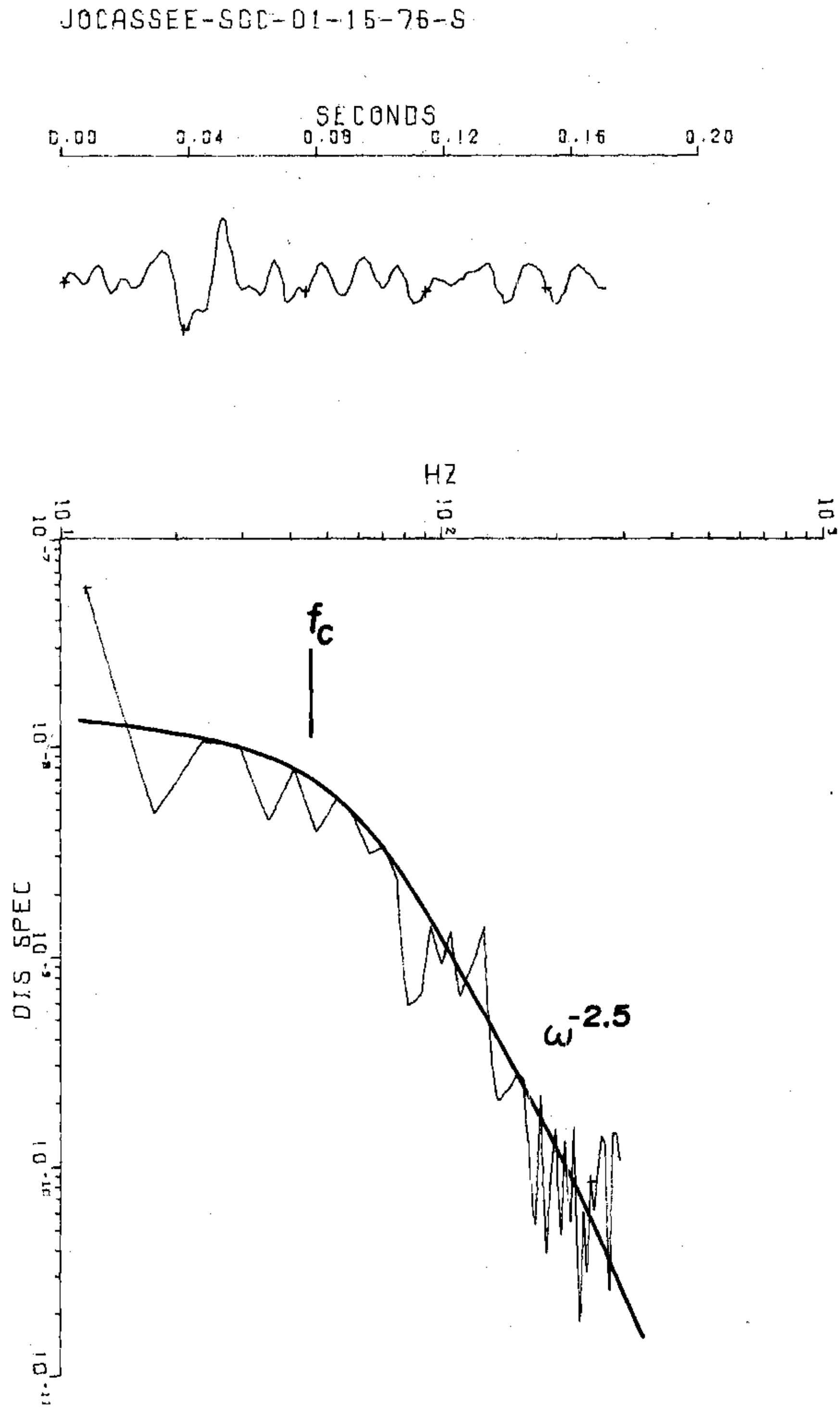

Figure 18. A Typical JRA S-wave Spectrum. (This is number 8 of Table 1.)

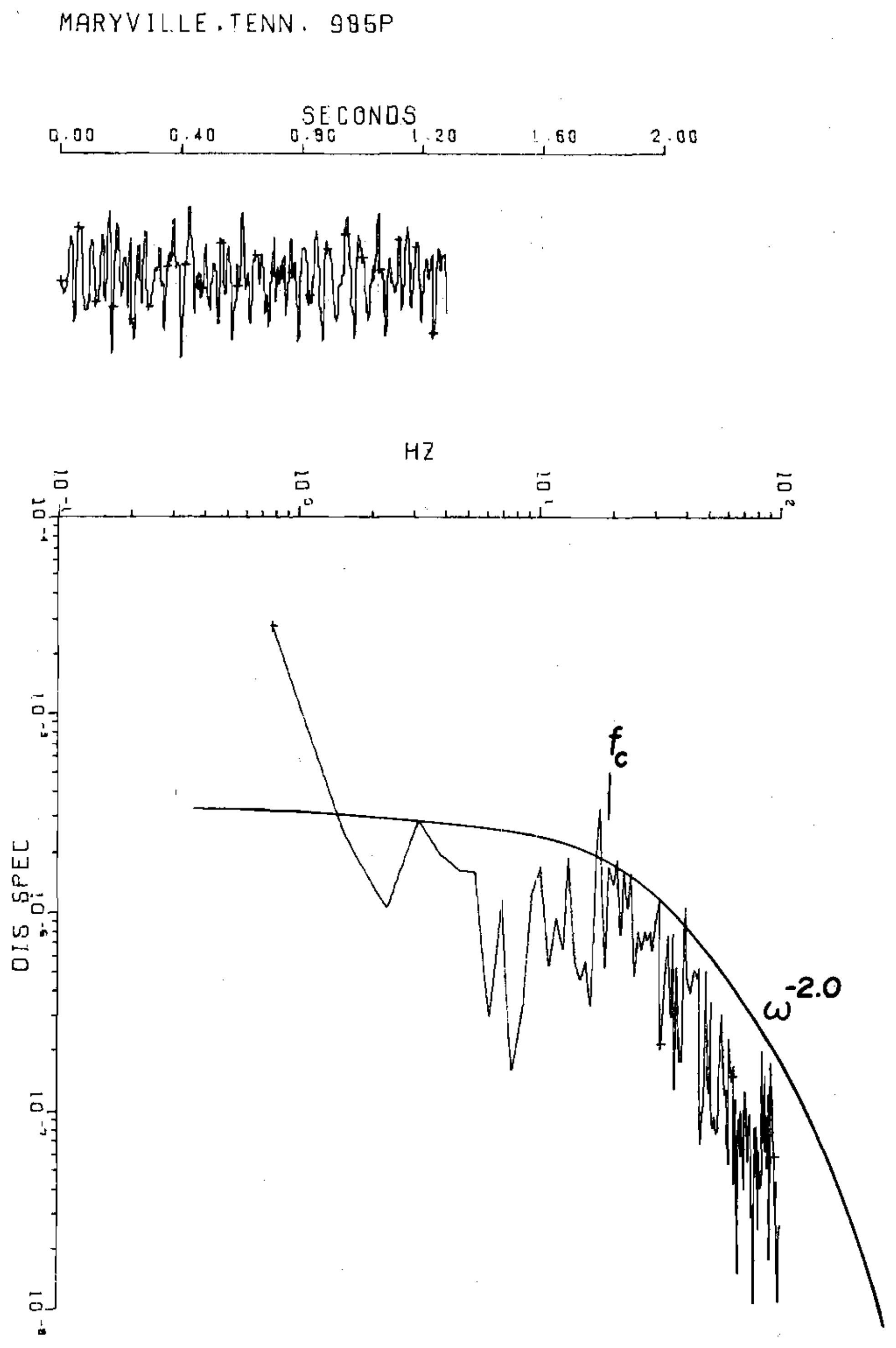

Figure 19. P-wave Spectrum of a MTA Microearthquake. (The title gives the location and tape footage.) (This is number 165 of Table 1.)

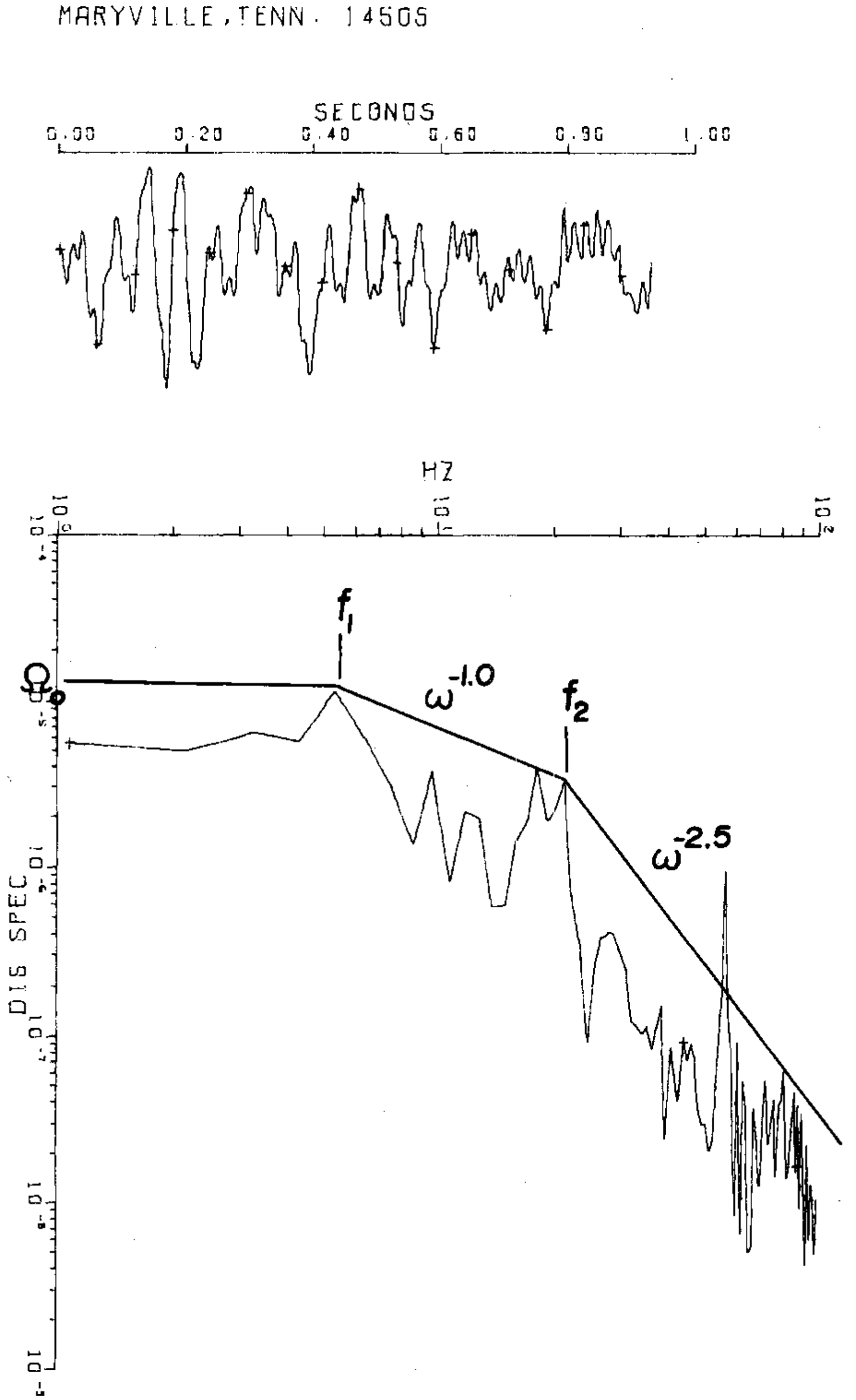

Figure 20. S-wave Spectrum of a MTA Microearthquake.
(This is number 164 of Table 1.)

CHAPTER VI

THEORY

Qualitative Analysis of Models

Displacement spectra are usually interpreted by comparison to spectra calculated from theoretical models which attempt to reproduce the important processes that occur during an earthquake. Most models of the seismic source are based on the concept of relaxation of stress. These models are usually developed in terms of either a tangential shear dislocation (Brune, 1970) or a change within a volume [e.g. volume changes, Randall (1964); phase transitions, Randall (1966); etc.]. The seismic source is assumed to be embedded in an infinite, homogeneous, isotropic, perfectly elastic medium. Tangential shear dislocation models are developed from assumptions concerning the shape of the rupture area, the rupture velocity, the duration of slip, the slip-time function, the effective stress drop, and the azimuth. Three types of solutions to the tangential shear dislocation are: the static solution (e.g. Keilis-Borok, 1959, 1960); the kinematic solution (e.g. Haskell, 1964; Savage, 1965, 1966, 1972, 1974); and the dynamic solution (e.g. Brune, 1970; Madariaga, 1976). The analytical solution to the static model is presented by Keilis-Borok (1959, 1960). The static solution uses a rupture velocity of zero and gives results which must show reasonable agreement with the kinematic and dynamic models when the long period limit is envoked. The kinematic case considers the effects of a realistic rupture velocity but does not concern itself with the transient aspects of fault plane stress. The dynamic solution relates the forces acting on the fault to the transient properties of the mechanics of faulting. Of the three solutions, the dynamic case is the most desirable; however, the mathematical computation of the three dimensional case is so unwieldy that a complete analytical solution has not yet been presented. Perhaps the most physically realistic dynamic solution presented thus far is given by Burridge and Halliday (1971), but it is strictly limited to two dimensions. Fortunately, computer capabilities have advanced to the point that three dimensional models can be considered by using numerical methods (e.g. Madariaga, 1976; Molnar et al., 1973).

The rupture velocity plays an important role in determining properties of the displacement spectra. The rupture velocity is the velocity at which the rupture front propagates, V_r, and is not to be confused with the particle velocity, $\dot{U}$. Rupture velocity may vary from zero in the static case to the P-wave velocity for the case of slip occurring along a pre-existing fault lacking cohesion (Burridge and Levy, 1974). Laboratory experiments (e.g. Mogi, 1973) demonstrate that a real crack propagating in a previously unfractured rock will propagate at a velocity no greater than the Rayleigh wave velocity which is 0.9 times the S-wave velocity. This velocity cannot be exceeded because that would require that propagation of the crack tip be an energy producing process (Fossum and Freund, 1975). Burridge and Levy (1974) demonstrate that the total stress acting during rupture is 5.357 times T_o, where T_o is the driving shear force. Thus, in order for the rupture velocity to be limited to the S-wave velocity, the static friction must be at least 5.357 times T_o. However, if cohesion is absent, rupture can propagate at the P-wave velocity (Burridge and Levy, 1974). These conditions suggest defining rupture velocities less than the S-wave velocity as being subsonic and rupture velocities greater than the S-wave velocity as being transonic. A subsonic model corresponds to fracture in previously unfractured rock and to slip on faults showing sufficient friction. A transonic model corresponds to slippage along pre-existing faults with slight cohesion.

Under certain conditions, a subsonic rupture can produce a spectrum characteristic of a transonic rupture. If all points along the fault surface radiate as a unit, then one observes an effective transonic rupture (Molnar et al., 1973) independently of the actual rupture velocity. The form in which this concept is used by Brune (1970-71) defies causality by requiring an instantaneous application of stress at all points along the fault surface. This requires that the particle velocity behaves as a step function in time, which requires an infinite particle acceleration (i.e. a "spike" or Delta function) at the instant that the stress pulse is applied uniformally over the surface. Even so, this extreme case is useful in a theoretical analysis because, although the acceleration goes to infinity, the forces acting remain finite as a result of the mass being zero in the limit (Brune, 1970). To justify using this theory, one must describe a physical case that is equivalent. The explanation is simply that most of a fault surface radiates simultaneously (Molnar et al., 1973) which is possible if the center continues to radiate at least until the edges begin radiating and the total duration of radiation is small with respect to the fault dimensions.

One of the distinctive properties of a displacement spectrum is the presence of spectral corners. A spectral corner occurs in a spectrum whenever a finite quantity in the time domain is transformed into the frequency domain. A working definition of a spectral corner is the transition point between two amplitude decay trends. Standard practice is to locate the corner at the intersection of best-fit lines asymptotically fitted to the decay trends. The frequency corresponding to the point of intersection is referred to as the corner frequency (Figure 20). Two spectral corners dominate the spectral analysis of earthquakes. Spectral corners may be explained in terms of characteristic phases (Savage, 1965, 1966A) and/or destructive interference patterns (Molnar _et al_., 1973).

Characteristic phases exist because a changing rupture velocity produces an energy content different from that of a constant rupture velocity. All of the models considered assume rupture velocity to be constant at all times except during initiation and termination of rupture. Thus, a characteristic phase produces an anomalous portion in a seismogram which is associated with either the initiation or termination of rupture. Constant velocity models can be generalized to a variable velocity but improvement in the results is not enough to justify the extra effort. Characteristic phases associated with the initiation of rupture are determined by the rise-time function and the type of nucleation. Savage (1972) notes that these two properties are essentially independent of each other and that a function containing both terms can be formed by a convolution in the time domain. One expects slippage to occur as a linear function of time, t^1, because a linear discontinuity corresponds to a finite change in the particle velocity (Randall, 1973B). The dimensions of a fault that nucleates at a point should initially increase as a t^1 discontinuity in time (Savage, 1966A). Consequently, the initiation of rupture is normally expected to occur as a quadratic discontinuity which transforms into an inverse cubic decay of amplitude with increasing frequency. The corner frequency corresponding to the inverse of the duration of the rise-time function is designated as f_2 (Figure 20). Characteristic phases associated with the termination of rupture are referred to as stopping phases and are produced by deceleration of the rupture edge (Savage, 1965, 1966A). The stopping phases are a measure of the far-field seismic pulse. The far-field seismic pulse is the duration between the time that the first point begins to radiate and the time that the last point ceases to radiate as measured in the far-field (Figure 21). The far-field seismic pulse is related to the dimensions of the fault rupture zone and is expressed as the seismic moment divided by the shear modulus, M_o/μ, which can predict all of the time properties of the far-field seismic trace (Madariaga, 1976).

The most realistic models are those that consider rupture to initiate at a point and spread radially. The center point continues to radiate until the stopping phases from the edges reach it. In this model the center of the fault slips more and radiates longer than any other point. The corner frequency, f_1, (Figure 20) corresponding to the far-field seismic pulse does not necessarily equal the inverse of the duration of radiation. Rather, the duration of the interval between arrivals of stopping phases is measured (Figure 21). The inverse of the time interval

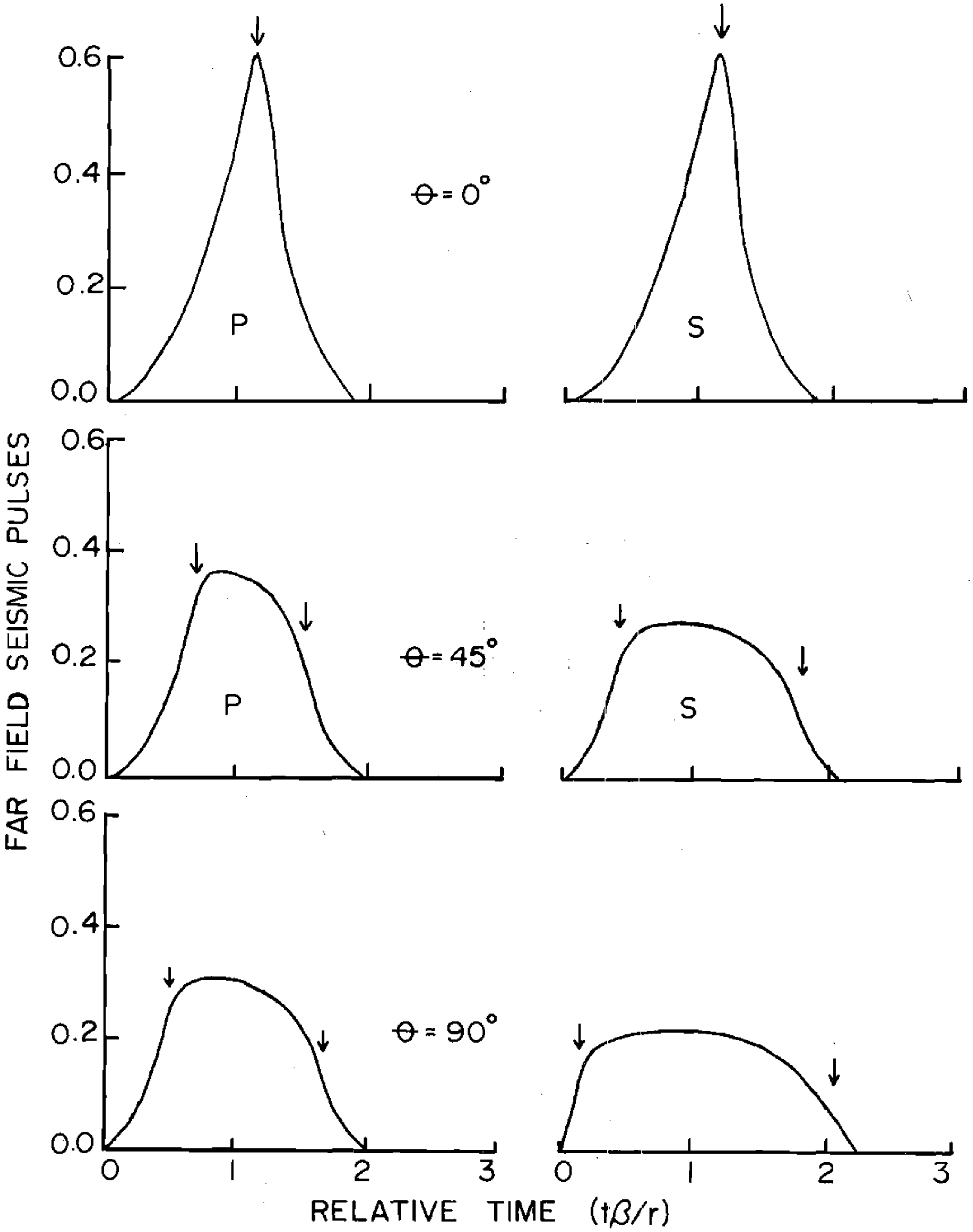

Figure 21. The Far-field Seismic Pulse as a Function of Azimuth. (The arrows indicate the arrival of stopping phases in the far-field.) (Diagram is from Madariaga, 1976.)

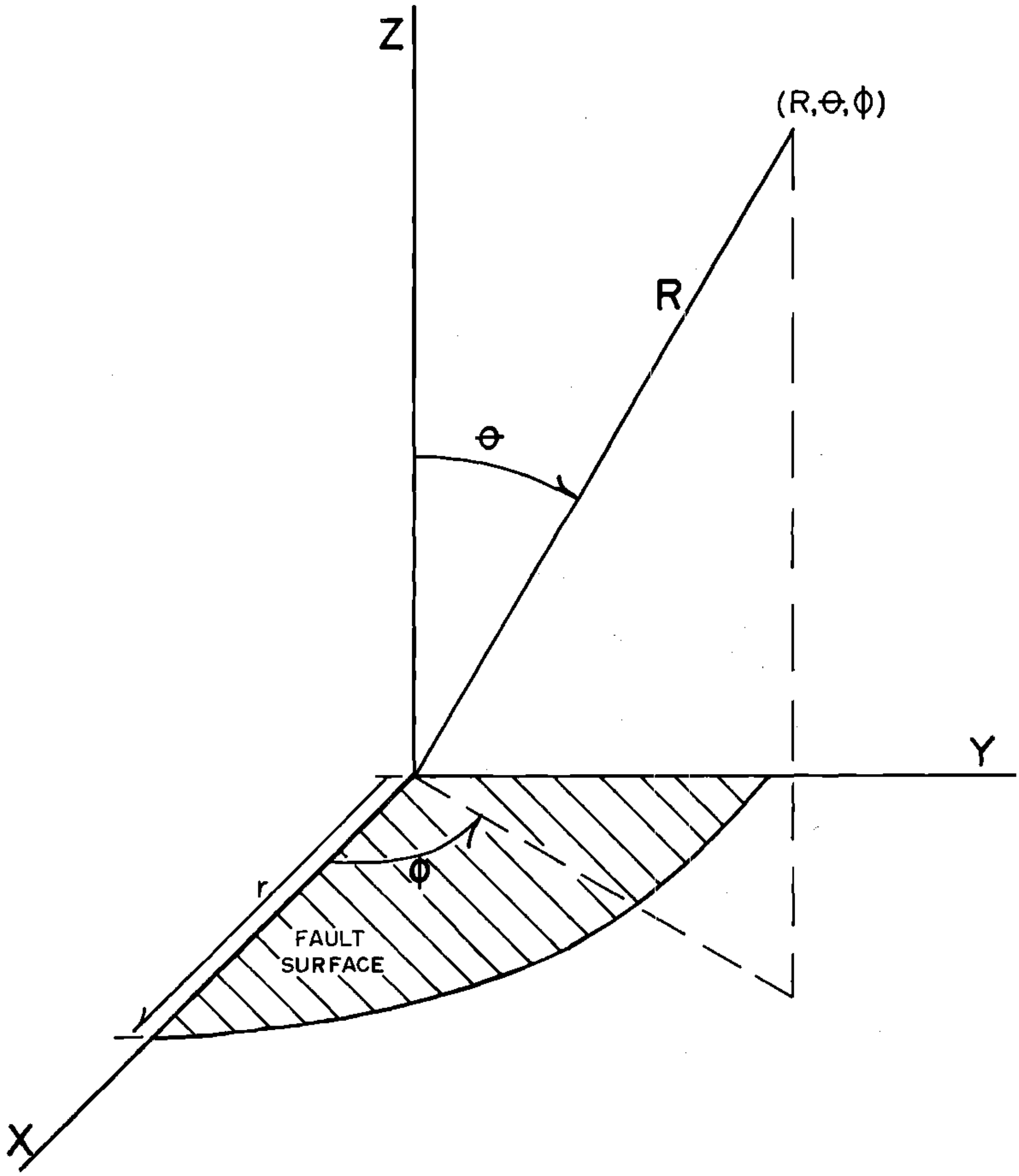

Figure 22. The Coordinate System. (The origin is located at the first point of rupture.)

between the arrival of the stopping phase from the nearest edge and the arrival of the stopping phase from the most distant edge gives the frequency at which this spectral corner will occur. The f_1 corner frequency can be used to determine the effective fault radius. For microearthquakes the effective fault radius is assumed to be equal to the actual rupture zone radius. Thus, the two dominant spectral corners are related to the rise time function (f_2) and to the fault dimensions (f_1). The f_1 corner frequency is also a function of the azimuth and rupture velocity. Azimuth, θ, is defined as being measured from the normal to the fault plane using polar coordinates (R, θ, ϕ) with the origin centered at the point of initial rupture (Figure 22). (The angle of wave incidence at the recording site is sometimes referred to as azimuth; but not in this paper.) Azimuth is used strictly to refer to the orientation of the fault plane in three dimensional space. The far-field effects are independent of the angle ϕ and depend only upon the angle θ (Savage, 1966A; Burridge, 1975). The time interval between recorded stopping phases is a function of the wave propagation velocity and the apparent distance between radiation points (Figure 21). If the observer is located at $\theta = 0$ degrees, the stopping phases from opposite edges will travel equal distances giving a recorded duration of zero time which suggests an infinite frequency for f_1 (i.e. fault radius equals zero). If the observer is located at $\theta = 90$ degrees, the distances that the two stopping phases travel differ by an amount equal to the fault length. At intermediate azimuths, intermediate apparent fault lengths are measured. This suggests that as azimuth decreases, corner frequencies move toward larger values. If both P- and

S-waves are radiated by the same fault dimensions, then the difference in distances travelled by each will be equal, but because the P-wave propagates faster than the S-wave, the time interval between arrivals of P-wave stopping phases will be shorter than the interval between S-wave stopping phases. The measured P-wave seismic pulse will be narrower than the S-wave seismic pulse. Therefore, the P-wave corner frequency should be higher than the S-wave corner frequency.

The discussion thus far suggests that the ratio of the P-wave corner frequency to the S-wave corner frequency, f_p/f_s, is greater than or equal to unity for all azimuths and that the corner frequency increases without bound as azimuth approaches zero. Both of these ideas produce results that are only approximate. Rupture velocity and interference effects modify the results. Molnar, et al. (1973) present a similar model and find that there is an upper limit to the frequency at which the corners may occur, because, in reality, the source is not a point, and the waves are modified by interference. These properties combine to restrict the range over which the corner frequencies may vary. Even so, the general statement that corner frequencies increase with decreasing azimuth should remain valid. The value of the ratio of corner frequencies will also be affected by the azimuth. The phenomenon is partly attributable to radiation patterns. A seismic source focuses P- and S-wave energies in different directions with S-waves being focused towards small azimuths and P-wave energies being focused towards large azimuths (Figure 23). Focusing suggests that P-waves radiated at small azimuths are of lower frequencies than P-waves radiated at large azimuths and vice versa for S-waves. Therefore, the ratio f_p/f_s should be less than unity for small azimuths

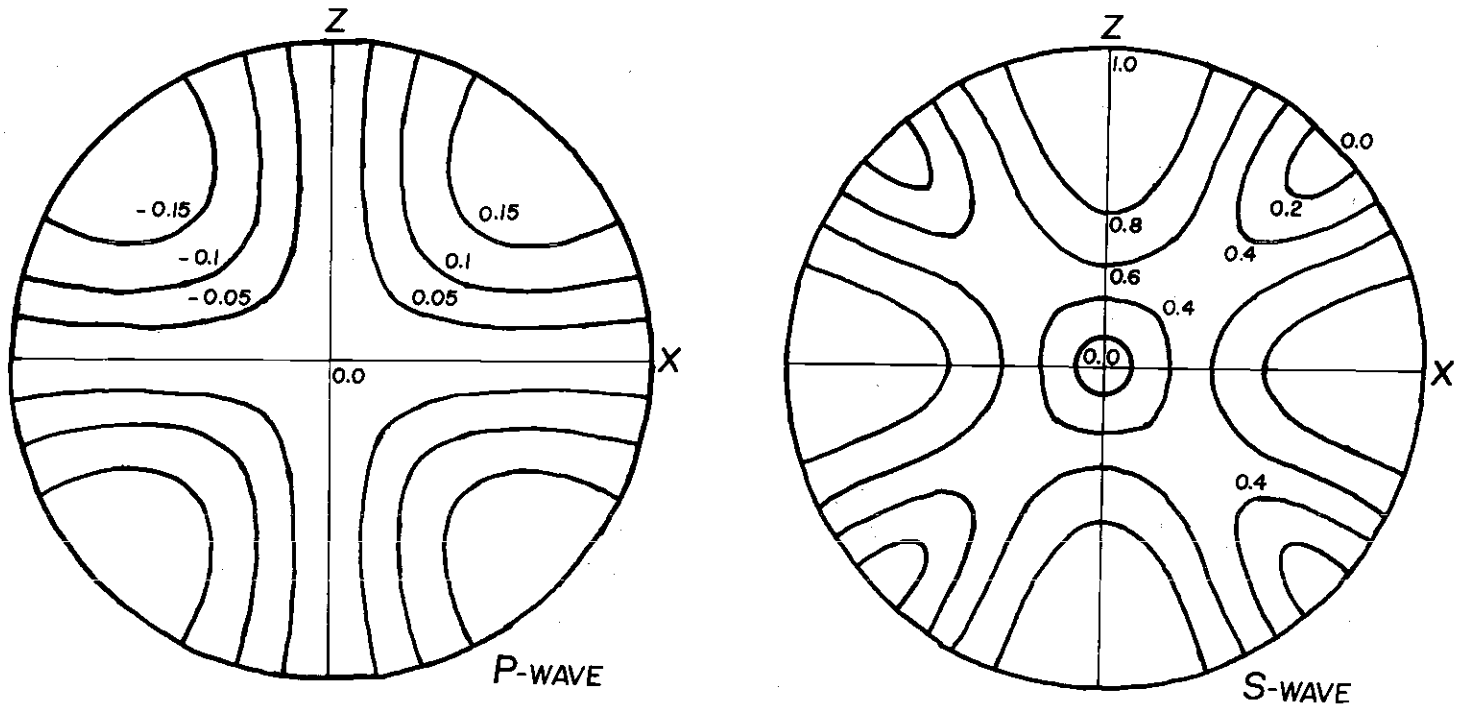

Figure 23. Radiation Patterns of a Double Couple (from Dahlen, 1974). (The fault plane is perpendicular to the page.)

and greater than unity for larger azimuths. A dynamic model presented by Madariaga (1976) shows f_p/f_s to be greater than unity for approximately 70% of the focal sphere in the transonic case (Figure 24). The model of Dahlen (1974) predicts ratios less than unity for all azimuths for subsonic rupture. However, Burridge (1975) shows that by extending the model of Dahlen (1974) to transonic rupture velocities one observes f_p/f_s to be greater than unity for 70% of the focal sphere. The Madariaga (1976) model finds f_p/f_s to be greater than unity even in the subsonic case and demonstrates that the actual value of the ratio will vary if subsonic rupture velocities are used. Therefore, the value of the ratio of corner frequencies appears to be a function of both azimuth and rupture velocity.

Certain properties must be present in a displacement spectrum if the seismic source results in the relaxation of stress (Randall, 1973A; Archambeau, 1968). The properties are that a spectrum must show a maximum amplitude at zero frequency and must decrease in amplitude with increasing frequency so as to conserve energy. A better intuitive feel for these properties can be attained by considering the sequence of processes that occur during an earthquake. This is done by reading a spectrum as a function of time rather than of frequency. A spectrum (e.g. Figure 13) can be read as chronological history of events by reading from right to left and noting that high frequency corresponds to small values of time and low frequency corresponds to large values of time. Rupture begins at time t = 0. Displacement increases with time. The more rapidly rupture occurs, the steeper the spectral slope will be, because the maximum displacement will be attained quicker. The spectral corner, f_c, corresponds

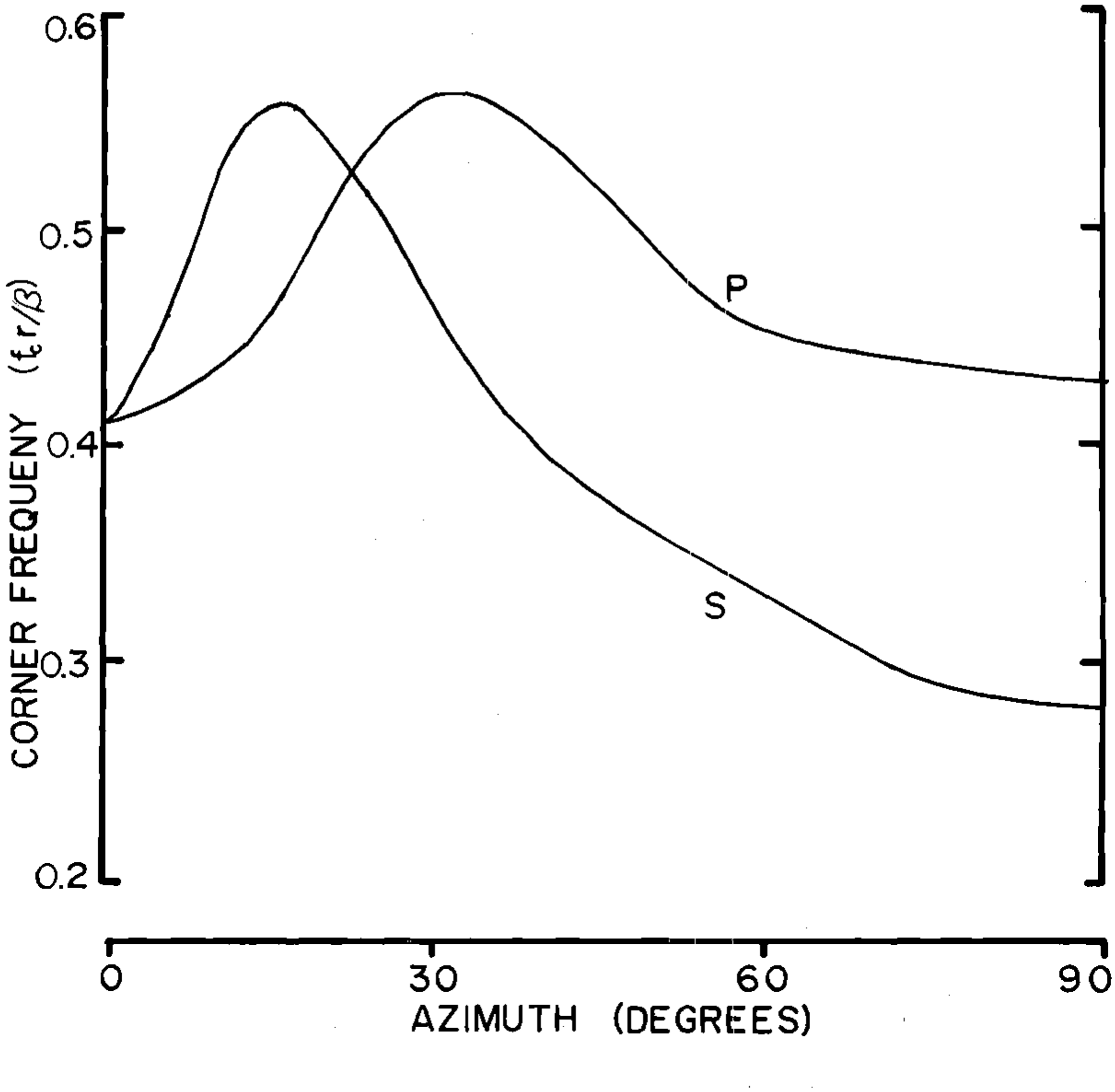

Figure 24. P-wave and S-wave Corner Frequencies as a Function of Azimuth for a Transonic Model (from Madariaga, 1976).

to the termination of displacement. Displacement is now constant for all time which shows as a line of slope zero in the spectrum. Having considered a spectrum as a chronological sequence of events, one can now return to the analysis according to frequency content.

The rate of amplitude decay at high frequencies is related to the highest order discontinuity in the time domain (White, 1965). The asymptotic behavior of the displacement spectrum is related to singularities in the time function of the form (from Lighthill, 1958)

$$U(t) \sim |t - t_o|^{\gamma-1} \tag{1}$$

which transforms into a term proportional to $\omega^{-\gamma}$, where ω is angular frequency. A condition that must be met is that the total energy must remain finite. This condition requires that γ must be greater than 1.5 (Hanks and Wyss, 1972). Therefore, the high frequency trend must decay faster than $\omega^{-1.5}$. The low frequency trend is considered to be proportional to $\gamma = 0$. The trend is ω^{o} because (i) rupture nucleates at a point and (ii) at distances and wavelengths large with respect to the fault dimensions, the fault will appear to be a point source. Point source radiation is described in terms of a Dirac delta function (White, 1965). A Dirac delta is a function composed equally of all frequencies; therefore, a spectrum of a Dirac delta is a line of constant amplitude (i.e. ω^{o}). The trend in spectral amplitude decay between the low and high frequency trends is the intermediate trend. The intermediate trend is bounded on the low frequency end by f_1 and by f_2 on the high frequency end. The intermediate trend, like the f_p/f_s ratio, has been the topic of considerable debate in the literature. An explanation by Aki (1967) suggests that the presence of the intermediate trend is evidence for a long narrow fault and the absence of the trend indicates an equidimensional fault. However, Madariaga (1976) finds this trend present even for a circular model. Brune (1970, 1971) relates this trend to partial stress drop. Madariaga (1976) relates this trend to the energy while Savage (1972, 1974) relates it to the slip function. The Savage kinematic models can be explained by the Brune or Madariaga models because they treat the dynamics that control the slip function. The Brune (1970, 1971) model describes the spectra as being a constant spectral amplitude determined by the stress, source dimensions, etc. multiplied by a spectral shape function (also see Randall, 1973B). The Brune (1970, 1971) shape function is assumed to be

$$G(\omega) = \omega_o^{-2} \left(1 - \frac{\omega^2}{\omega_o^2}\right)^{-1} \qquad (2)$$

such that the high frequency trend is proportional to an inverse square of angular frequency. The spectral amplitude is also multiplied by a term which has the effect of causing the spectral shape function to decay as ω^{-1} for a time before going into the high frequency trend if the fault has experienced premature termination of slip (i.e. partial effective stress drop). Effective stress drop refers to the stress available to produce slip and is not to be confused with the total stress in the rocks or even the total stress drop which includes energy released as frictional heat. This model requires that the f_1 corner be measured between the low- and high-frequency trends which locates f_1 approximately in the middle of the "intermediate" trend. An alternative explanation is presented by Madariaga (1976). Madariaga (1976) treats a subsonic dynamic model and finds three dominant slopes and assigns the following explanation:

1) Low frequency trend.

   This portion behaves as ω^{o} because the source appears to be a point source. This trend is controlled by the seismic moment.

2) Intermediate frequency trend.

   This trend involves a number of decay rates between $\omega^{-1.5}$ and $\omega^{-2.0}$ which vary with azimuth. This trend is related to the far-field seismic pulse and is controlled by the energy. The slope seems to be related to the order of discontinuity of the stopping phases.

3) High frequency trend.

   This trend is related to the highest order time discontinuity in the seismic pulse and is often obscured by radiation from irregularities in the fault. The slope is typically $\omega^{-2.5}$ to $\omega^{-3.0}$.

Earlier the statement was made that earthquakes can be modeled as either tangential shear dislocations or as a change within a volume. After making this statement the discussion very conveniently ignored volume models. The reason is that the spectral shapes are equivalent. Both a volume source model and a shear dislocation source model can explain the observed spectra. However, the discussion has been presented in terms of a tangential shear model because intuitively the shear model is a more realistic model for shallow focus microearthquakes.

Mathematical Formulation of a Model

Equations relating the source model to the displacement spectra are presented to help clarify the relation of model and source. The presentation is patterned after the work of Brune (1970, 1971) because it gives a mathematical-intuitive solution to a dynamic model applicable to a three dimensional analysis of spectral data. Recall that a completely analytic solution has not yet been presented, and a discussion of a numerical solution would not really help clarify relationships. The near-field is defined as being at distances small with respect to the fault dimensions and the far-field is defined as being at distances large with respect to the fault dimensions (Brune, 1970, from Keilis-Borok, 1960). The recorded data are recorded in the far-field while the seismic model gives information in the near-field. The problem then is to generalize the near-field to the far-field. The Brune (1970, 1971) model relates the stress acting upon the fault to properties of the rupture process by assuming a form of the initial time function for the near-field given by

$$\sigma(x,t) = \sigma H(t - x/V_r) \tag{3}$$

where

σ = effective stress

V_r = velocity of stress pulse propagation.

Brune (1970) uses $V_r = \beta$

$H(\tau)$ = Heaviside step function

$$= \begin{matrix} 0 & \tau < 0 \\ 1 & \tau > 0 \end{matrix} \qquad \text{where } \tau = t - x/V_r$$

The tangential displacement along the x-axis produced by the stress pulse is related to the force acting by

$$\sigma = \mu \frac{\partial U}{\partial x} \tag{4}$$

The assumption is made that the ruptured surface will not transmit elastic energy so that only one side of the fault need be investigated. Assuming a unit fault width, the mass accelerated in Figure 25 is given by

$$\text{Mass} = 1 \cdot V_r \Delta t \cdot c \Delta t \cdot \rho \tag{5}$$

where

c = seismic wave propagation velocity

$= \begin{matrix} \alpha \text{ if P-wave} \\ \beta \text{ if S-wave} \end{matrix}$

ρ = density

The shear stress is the force per unit area of the fault, given by

$$\sigma = \frac{1 \cdot V_r \Delta t \cdot c \Delta t \cdot \rho \cdot \ddot{U}}{1 \cdot V_r \Delta t} \tag{6}$$

Equation (6) gives the particle acceleration as

$$\ddot{U} = \frac{\sigma}{\rho c \Delta t} \tag{7}$$

Integrating gives the particle velocity and displacement

$$\dot{U} = \frac{\sigma}{\rho c} \tag{8}$$

$$U = \frac{\sigma}{\rho c}\, t \tag{9}$$

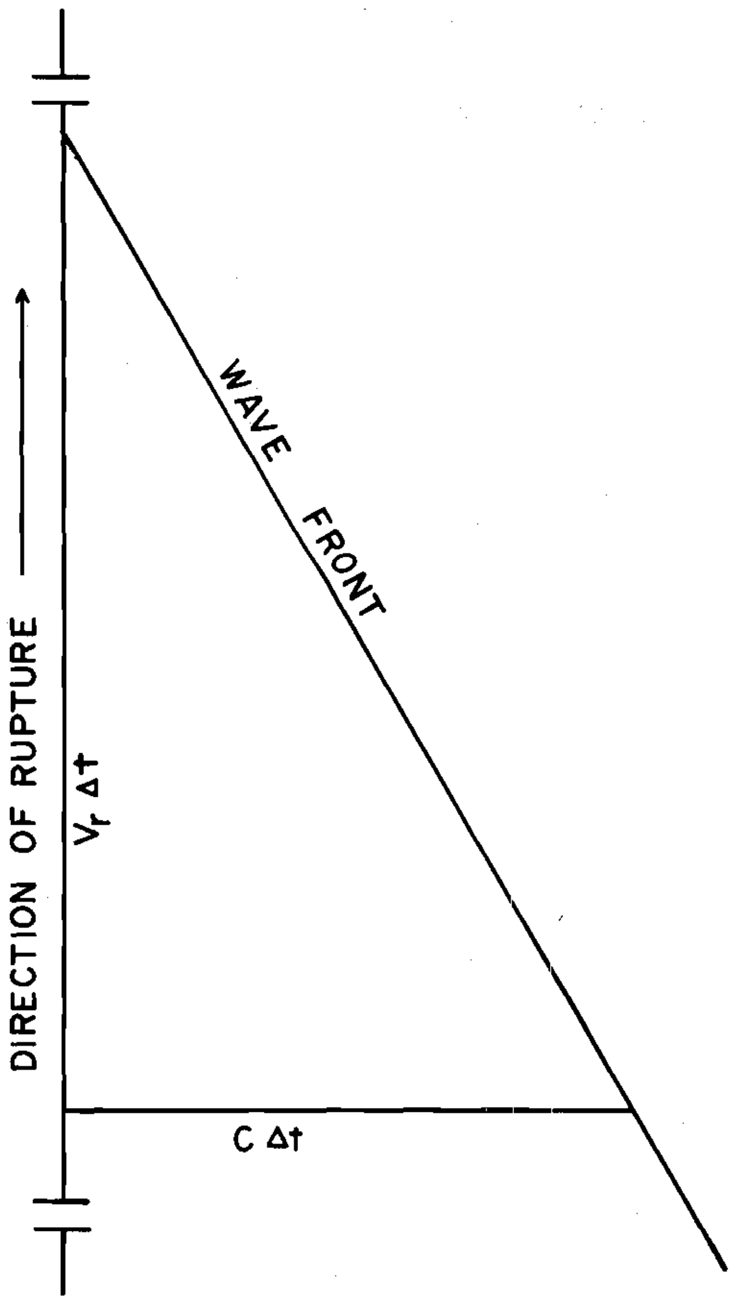

Figure 25. Stress Application Along a Fault Surface (from Brune, 1970).

Notice that the rupture velocity divided out of equation (6). In reality, the rupture velocity should still be present in equations (6 - 9) because the application of stress is a function of time related to the rupture velocity. This suggests that equation (3) is greatly over-simplified. Brune (1970) points out that equation (6) gives a S-wave particle velocity of approximately 100 cm/sec for a stress drop of 100 bars. The maximum shear wave particle velocity recorded as of 1970 is 76 cm/sec recorded during the Parkfield, California, earthquake by a strong-motion seismograph located nearly on the fault trace (Brune, 1970, from Housner and Trifunac, 1967). The value suggested is reasonable, allowing Brune (1970) to suggest that 100 bars is an upper limit for stress drop in most earthquakes.

Randall (1973B) states that the displacement spectrum is obtained by a Fourier transform of the particle displacement function

$$\Omega(\omega) = \int_{-\infty}^{\infty} U(t)\, e^{-i\omega t}\, dt \tag{10}$$

The near-field spectrum is given by equations (9) and (10) as

$$\Omega_{ps}(\omega) = \int_{0}^{\infty} \frac{\sigma}{\rho c}\, t\, e^{-i\omega t}\, dt \tag{11}$$

$$= -\frac{\sigma}{\rho c}\,\omega^{-2}$$

The far-field spectrum is obtained from the near-field spectrum by accounting for propagation effects. Spherical spreading of the wave front will cause amplitude to fall off as the inverse of the hypocentral distance. Therefore, the term r/R, where r is fault radius and R is hypocentral distance, must be included. Diffraction effects due to the fault edges will produce the same observable effect in the far-field as a double couple source (Brune, 1970, from Burridge and Knopoff, 1964). The constructive and destructive interference associated with diffraction are accounted for by including a phase term which decays exponentially as r/c (Brune, 1970, Molnar et al., 1973). The radiation pattern causes wave amplitudes to vary with azimuth, requiring a correction factor $R^{ps}_{\theta\phi}$ (Figure 23). Yet another possibility is that one type of wave energy may be converted into wave energy of another type (e.g. P-waves can be converted to S-waves upon reflection). Energy loss is corrected for by a term which varies from unity to zero such that

$$N = \begin{cases} 1 & \text{if no energy is lost} \\ 0 & \text{if all energy is lost} \end{cases} \tag{12}$$

Applying these propagation corrections to equation (9) gives the far-field particle displacement as

$$U(t) = R^{ps}_{\theta\phi} \cdot N \cdot r/R \cdot \sigma/\rho c \cdot \tau' e^{-\omega_o \tau'} \tag{13}$$

where

$\tau' = t - R/c$ such that τ' behaves in the far-field exactly as t behaves in the near-field.

Observed data would also include a correction for inelastic properties of the medium, $\exp(\frac{-\omega R}{2Qc})$, but the assumption of perfect elasticity precludes the use of this term in equation (13).

A Fourier transform of equation (13) gives the far-field spectrum (equation 15). However, the Fourier transformation must be performed by intuitive knowledge of the answer rather than by analytical methods to avoid the inclusion of complex terms into what must be interpreted as a real quantity. (Remember, the complete analytical dynamic solution has yet to be accomplished.) The success of this model is due to the fact that Brune (1970, 1971) was able to intuitively define a shape function which has the same general properties that the Fourier transformed term should have. This function is

$$G(\omega/\omega_o) = \frac{1}{\omega_o^2 + \omega^2}$$

$$= \omega_o^{-2}(1 + \omega^2/\omega_o^2)^{-1} \qquad (14)$$

The far-field spectrum is then

$$\Omega_{ps}(\omega) = R_{\theta\phi}^{ps} \cdot N \cdot r/R \cdot \sigma/\rho c \cdot \omega_o^{-2}\,(1 + \omega^2/\omega_o^2)^{-1} \qquad (15)$$

The short period limit of equation (15) is

$$\lim_{\frac{\omega}{\omega_o} \to \infty} \Omega_{ps}(\omega) = R_{\theta\phi}^{ps} \cdot N \cdot r/R \cdot \sigma/\rho c \cdot \omega_o^{-2}\,(\omega/\omega_o)^{-2} \qquad (16)$$

which states that the high frequency asymptote decays as the inverse square of the angular frequency. The long period limit of equation (15) is

$$\lim_{\frac{\omega}{\omega_o} \to 0} \Omega_{ps}(\omega) = R_{\theta\phi}^{ps} \cdot N \cdot r/R \cdot \sigma/\rho c \cdot \omega_o^{-2} \qquad (17)$$

which indicates that at low frequencies the amplitude of the spectrum is constant.

A constant, ε, is defined such that the spectrum is reduced to ε times the value for 100% effective stress drop. The case of fractional stress drop caused by premature stick is accounted for by Brune (1970) by multiplying the spectrum by

$$F(\varepsilon) = \{[2 - 2\varepsilon][1-\cos(0.85\,\frac{\varepsilon\omega}{\omega_o})] + \varepsilon^2\}^{1/2} . \qquad (18)$$

The function $F(\varepsilon)$ oscillates between ε and $2-\varepsilon$, with a mean value of

$$F(\varepsilon) = 1.6 - 0.6\varepsilon \qquad (19)$$

The spectrum now becomes

$$\Omega_{ps}(\omega) = R^{ps}_{\theta\phi} \cdot N \cdot r/R \cdot \sigma/\rho c \cdot F(\varepsilon) \cdot G(\omega/\omega_o) \qquad (20)$$

The effect of a fractional stress drop is to produce an intermediate trend (discussed in Brune, 1970, page 5006). The far-field spectrum of a double couple source for the static case is given by Hanks and Wyss, (1972) as

$$\Omega_{ps}(0) = R^{ps}_{\theta\phi} \cdot M_o \cdot (4\pi\,\rho\,R\,c^3)^{-1} \qquad (21)$$

where M_o is the seismic moment.

Recalling that the long period limit should agree with the static solution gives, using equations (21) and (20),

$$N = \frac{M_o \omega_o^2}{4\pi r \sigma c^2 F(\varepsilon)} \qquad (22)$$

For earthquakes which rupture the surface, the seismic moment is determined from field observations by measuring the fault length and the displacement and using (from Brune, 1970)

$$M_o = \mu A \, \overline{U}_d \tag{23}$$

where a Poisson solid is assumed

and

$$A = \text{area} \tag{24}$$
$$= \pi r^2$$

$$\overline{U}_d = \text{average fault displacement} \tag{25}$$
$$= 2/3 \; U_{d\ max}$$
$$= \sigma/\mu \cdot r \cdot 16/7\pi$$

Equation (23) when rewritten to include equations (24) and (25) becomes (Brune, 1970-71)

$$M_o = \frac{16}{7} \sigma r^3 \; . \tag{26}$$

Combining equations (22) and (26) gives

$$N = 1/F(\varepsilon)(4/7\pi)(r \; \omega_o/c)^2 \tag{27}$$

Because of the extremely short propagation distances of events used in this thesis, the conversion factor, N, can be set to unity. Assuming complete effective stress drop (i.e. $F(\varepsilon) = 1$), equation (27) becomes

$$\omega_o = (7\pi/4)^{1/2}(c/r) \tag{28}$$
$$= 2.34(c/r)$$

which happens to be the form used by Hanks and Wyss (1972).

A more general form is

$$f_c = \frac{k}{2\pi} \frac{c}{r} \tag{29}$$

This is the relation which allows the determination of the fault dimensions from the spectral corner frequency, f_c. Equation (29) is a good approximation and has been used extensively in the literature.

Recalling an earlier discussion of the Savage (1972) kinematic model, one finds that a convolution can be used to write equation (14) as

$$G(\omega/\omega_o) = \omega_o^{-3} (1 + \omega^3/\omega_o^3)^{-1} . \tag{30}$$

Equation (30) could be substituted for equation (14) and the analysis should explain an inverse cubic decay. Likewise, the relation (29) which suggests values of $f_p/f_s = 1.7$ for an average azimuth would be changed to $f_p/f_s = 1.4$ for an average azimuth, closer to the value found by Madariaga (1976) by numerical analysis. Equation (15) can be expressed in terms of the seismic moment by using equation (26) as (see Randall, 1973B)

$$\Omega_{ps}(\omega) = \frac{R^{ps}_{\theta\phi} M_o}{4\pi R \rho c^3} \cdot G(\omega/\omega_o) \tag{31}$$

or

$$M_o = \frac{\Omega_{ps}(\omega)}{R^{ps}_{\theta\phi} G(\omega/\omega_o)} \cdot 4\pi R \rho c^3 \tag{32}$$

Magnitude

Magnitude is a number assigned to an earthquake to facilitate statistical analysis of earthquakes. Magnitude estimation is at best only approximate because an earthquake involves a number of variables (seismic energy, fault dimensions, etc.). Seismic moment appears to be an excellent candidate for use in a magnitude relation because it is a function of fault displacement, seismic energy, and the fault dimensions. A relation is developed by McGarr (1976) to relate local magnitude, M_L, to the seismic moment for microearthquakes, $-0.4 \leq M_L \leq 2.9$, recorded near Denver, Colorado. The relation is

$$\log_{10} M_o = 1.7\, M_L + 15.1 \tag{33}$$

Equations of the same form as equation (33) but with different constants are used by Thatcher and Hanks (1972) and Wyss and Brune (1968) to describe larger earthquakes in other regions. The seismic moment is calculated directly from a spectrum by using equation (32). Therefore, equation (33) can be used to calculate an approximate value of local magnitude directly from the spectra presented in this thesis. The value will be only approximate because M_L applies strictly to southern California where it was developed and because the data set presently available for the data regions studied is insufficient to allow an adjustment of the constants of proportionality.

Seismic Energy

The potential energy which is stored in rocks in the form of strain is converted during the rupture process into energy in the form of friction and elastic waves. The energy used in overcoming friction cannot be determined from the seismic trace; however, elastic wave energy can be determined from the seismic trace because the ground motion at the seismic station is similar to a harmonic oscillator. The energy of a harmonic oscillator is given by Marion (1970) as

$$E_R = 1/2\ m\omega^2\ h^2 \tag{34}$$

where m = mass accelerated

ω = angular frequency

h = amplitude

Similarly, the seismic wave energy is calculated by applying Parsaval's theorem which is given by Kanasewich (1975) as

$$E = \frac{1}{2\pi} \int_{-\infty}^{\infty} |y_o(\omega)|^2\ d\omega \tag{35}$$

where E = energy density

$y_o(\omega)$ = a convolution such that $y_o(\omega) = \Omega_{ps}(\omega)\cdot\omega$

Equations (31) and (35) suggest

$$E_R = (\rho c R^2)\ \frac{M_o^2\ {R_{\theta\phi}^{ps}}^2\ \omega_c^{\,3}}{2(2\pi)^3 R^2 \rho^2 c^6} \int_0^{\infty} |G(\frac{\omega}{\omega_o})\cdot\omega|^2\ d\omega \tag{36}$$

where $\rho c R^2$ is the mass term needed to convert energy density into total energy, and $\omega_c^{\,3}$ arises from integration of the long period limit.

Equation (36) may be rewritten as

$$E_R = \frac{{R_{\theta\phi}^{ps}}^2}{2} \cdot \frac{M_o^{\,2}}{\rho c^5} \cdot f_c^{\,3} \cdot I \tag{37}$$

where Randall (1973B) describes I as

$$I = \int_0^{\infty} |G(\omega/\omega_o)\ \cdot\ \omega|^2\ d\omega \tag{38}$$

and Hanks and Wyss (1972) evaluate as

$$I = \left(\frac{1}{3} + \frac{1}{2\gamma - 3}\right) \tag{39}$$

where γ = order of high frequency decay trend.

Both definitions of I are equivalent. Equation (37) expresses the total energy radiated in the form of either P-waves or S-waves. For the case of an inverse cubic decay one finds I = 0.67 which suggests that energy is given as

$$E_R = \frac{1}{2} \mathcal{R}^{ps^2}_{\theta\phi} \cdot \frac{M_o^2}{\rho c^5} \cdot f_c^3 \, 0.67 \tag{40}$$

The ratio of the average P-wave energy to the average S-wave energy is

$$\frac{E_R^p}{E_R^s} = \frac{\langle \mathcal{R}^p_{\theta\phi} \rangle^2}{\langle \mathcal{R}^s_{\theta\phi} \rangle^2} \left(\frac{M_o^p}{M_o^s}\right)^2 \left(\frac{\beta}{\alpha}\right)^5 \left(\frac{f_p}{f_s}\right)^3 \tag{41}$$

Assuming a Poisson solid, the proper scaling between $\mathcal{R}^p_{\theta\phi}$ and $\mathcal{R}^s_{\theta\phi}$ should be $\mathcal{R}^s_{\theta\phi} = \left(\frac{\alpha}{\beta}\right)^3 \mathcal{R}^p_{\theta\phi}$ which suggests that equation (31) shows

$$\frac{M_o^p}{M_o^s} \sim \frac{\Omega_p(0)}{\Omega_s(0)} \tag{42}$$

Assuming that $M_o^p = M_o^s$, then equations (29) and (41) give

$$\frac{E_R^p}{E_R^s} = \frac{\langle \mathcal{R}^p_{\theta\phi} \rangle^2}{\langle \mathcal{R}^s_{\theta\phi} \rangle^2} \left(\frac{\beta}{\alpha}\right)^2 \tag{43}$$

The average values of the azimuthal patterns for an energy distribution are given by Wu (1966) as

$$\langle R^{P}_{\theta\phi}\rangle^{2} = \frac{4\pi}{15} \tag{44}$$

$$\langle R^{S}_{\theta\phi}\rangle^{2} = \frac{24\pi}{15}$$

Then

$$\frac{E^{P}_{R}}{E^{S}_{R}} = 0.06 \tag{45}$$

If a cubic relation is used, equation (45) becomes

$$\frac{E^{P}_{R}}{E^{S}_{R}} = 0.03 \tag{46}$$

In either case, the P-wave energy is almost unimportant with respect to the S-wave energy. Combining equations (40), (44), and (46) gives

$$E_{R} = 1.8\,\frac{M_{o}^{2}\,f_{s}^{3}}{\rho\,\beta^{5}} \tag{47}$$

Equation (47) is effectively the total body wave energy (i.e. P-wave plus S-wave). The constant of proportionality is adjusted for use of the vertical component.

As a point of interest, note that Brune (1970-71) finds that the S-wave body waves carry approximately 44% of the total seismic energy of an earthquake. In light of the energy ratios, one sees that somewhat less than 50% of the total seismic energy is radiated as body waves.

CHAPTER VII

CALCULATIONS

Having presented the observed spectra and equations for use in interpretation, the next obvious step is to apply the equations to the spectra to calculate values for use in interpretation. The seismic moment is calculated from equation (32) by recalling that at zero frequency $G(\omega/\omega_o)$ equals unity. Equation (32) then becomes

$$M_o = \frac{\Omega_{ps}(0)}{R^{ps}_{\theta\phi}} \cdot (4\pi R\rho c^3) \qquad (48)$$

(Refer to Figure 20 for instructions on measuring $\Omega_{ps}(0)$.)
The effective stress drop is calculated from equation (26) by writing it in the form

$$\sigma = \frac{7}{16}\frac{M_o}{r^3} \qquad (49)$$

where σ is used rather than $\Delta\sigma$ because a complete effective stress drop is assumed. The maximum relative fault particle displacement is calculated from the stress drop by using equation (25) in the form

$$U_{d_{max}} = \frac{\sigma r}{\rho\beta^2} \cdot \frac{16}{7\pi} \cdot \frac{3}{2} \qquad (50)$$

The magnitude is calculated from equation (33) and the energy is calculated from equation (47). The source dimensions are determined for an average value of azimuth from the plots presented in Figure 24. The relations for the transonic model are

$$r_p = 1.6/f_p \tag{51}$$

and

$$r_s = 1.2/f_s \tag{52}$$

The relations for the subsonic model are

$$r_p = 1.2/f_p \tag{53}$$

and

$$r_s = 0.8/f_s \tag{54}$$

Table 1. Values Calculated from the Observed Spectra

ID#	Event		Phase	$-\gamma$	R E-5 cm	$\Omega(0)$ cm-sec	f_c	f_p/f_s	r E-5 cm	M_o dyne-cm	$\Delta\sigma$ bars	M_L	$U_{d\,max}$ cm	E_R Joules
1	LBT 03/04/76		P	3.0	4.68	6.0E-10	87	1.3	0.018	1.1E16	0.83	0.6	4.9E-3	9.6E2
2	LBT 03/04/76		S	3.0	4.68	2.0E-9	62		0.019	1.6E15	0.20	0.1	1.1E-3	7.3E0
3	DFE 01/15/76		P	2.5	3.41	7.0E-10	86	2.0	0.019	9.1E15	1.1	0.5	7.0E-3	6.3E2
4	DFE 01/15/76		S	2.5	3.41	4.0E-9	43		0.028	2.3E15	0.03	0.2	2.7E-4	5.0E0
5	ESD 01/15/76		P	3.0	2.36	6.5E-10	100		0.016	5.8E15	0.50	0.4	2.6E-3	4.0E2
6	ESD 01/15/76		S	3.0	2.36	1.2E-9	88		0.013	4.8E14	0.10	-0.2	2.1E-4	1.9E0
7	SGC 01/15/76		P	3.0	1.72	5.0E-10	90	2.1	0.018	3.3E15	0.20	0.2	1.2E-3	9.5E1
8	SGC 01/15/76		S	2.5	1.72	1.4E-9	42		0.029	4.1E14	0.10	-0.3	9.6E-5	1.5E-1
9	PLS 11/09/75	08:26:08	P	3.0	1.74	3.6E-9	71	1.3	0.022	2.4E16	1.01	0.8	7.2E-3	2.5E3
10	PLS 11/09/75	08:26:08	S	2.0	1.74	1.0E-8	55		0.022	3.0E15	0.20	0.2	1.2E-3	1.8E1
11	PLS 11/08/75	21:18:48	P	3.0	2.44	7.2E-10	70	1.0	0.023	6.7E15	0.21	0.4	1.4E-3	1.9E2
12	PLS 11/08/75	21:18:48	S	3.0	2.44	4.0E-9	67		0.018	4.1E14	0.04	-0.3	2.4E-4	6.1E-1
13	PLS 11/08/75	02:30	P	3.0	2.37	2.8E-10	60	1.0	0.027	2.5E15	0.05	0.2	4.9E-4	1.6E1
14	PLS 11/08/75	02:30	S	3.0	2.37	7.0E-10	60		0.02	2.8E14	0.02	-0.4	1.3E-4	2.0E-1
15	GNC 06/08/76	1st triple	P	3.0	1.42	4.0E-10	78	1.1	0.020	2.2E15	0.08	0.1	5.3E-4	2.7E1
16	GNC 06/08/76	1st triple	S	3.0	1.42	9.0E-10	75		0.016	2.2E14	0.01	-0.4	6.6E-5	2.4E-1
17	GNC 06/08/76	2nd triple	P	3.0	1.42	2.2E-10	78	1.0	0.020	1.2E15	0.05	-0.0	3.3E-4	8.2E0
18	GNC 06/08/76	2nd triple	S	3.0	1.42	4.5E-10	79		0.015	1.1E14	0.01	-0.6	6.6E-5	7.2E-2
19	GNC 06/08/76	3rd triple	P	3.0	1.42	4.0E-10	65	0.9	0.025	2.2E15	0.05	0.1	4.9E-4	1.6E1
20	GNC 06/08/76	3rd triple	S	3.0	1.42	8.0E-10	78		0.016	2.0E14	0.01	-0.5	6.6E-5	2.3E-1
21	DKF 06/08/76	01:33:58	P	3.0	1.34	1.0E-9	70		0.023	5.1E15	0.20	0.4	1.4E-3	1.1E2
22	CH5 06/07/76		1st	3.0	1.50?	4.3E-7	24	1.2						
23	CH5 06/07/76		2nd	3.0	1.50?	1.6E-6	20							
24	CH5 06/03/76		1st	?	1.00?	?								
25	CH5 06/03/76		2nd	3.0	1.00?	2.0E-6	20		0.066					

Table 1. (Continued)

ID#	Event	Phase	$-\gamma$	R E-5 cm	$\Omega(0)$ cm-sec	f_c	f_p/f_s	r E-5 cm	M_o dyne-cm	$\Delta\sigma$ bars	M_L	$U_{d\,max}$ cm	E_R Joules
26	STA 1 (EOC) 04/02/76	all	3.0	2.34	2.0E-9	60		0.028	1.8E16	0.40	0.7	3.6E-3	8.4E2
27	CH5 02/05/76	1st	2.5	1.80	6.0E-9	41	1.0	0.039	1.8E15	0.01	0.1	1.4E-4	2.7E0
28	CH5 02/05/76	2nd	3.0	1.80	8.0E-9	40		0.030	2.6E15	0.02	0.2	2.4E-4	5.2E0
29	GNC 02/05/76 02:04:+	P	3.0	0.40	2.0E-10	108	2.7	0.015	3.0E14	0.03	-0.4	2.0E-4	1.4E0
30	GNC 02/05/76 02:04:+	S	3.0	0.40	8.0E-10	40		0.030	5.4E13	0.04	-0.8	1.0E-4	2.0E-3
31	GNC 02/05/76 01:27:42	P	2.5	0.40	1.6E-10	120	4.0	0.013	2.4E14	0.01	-0.4	2.1E-4	1.2E0
32	GNC 02/05/76 01:27:42	S	2.5	0.40	2.0E-9	30		0.040	1.4E14	0.05	-0.6	1.3E-4	1.0E-2
33	GNC 02/04/76 03:58:15	P	3.0	0.60									
34	GNC 02/04/76 03:58:15	S	?	0.60									
35	HUM 12/19/75 20:10:58	P	3.0	1.34	1.0E-10	110	1.0	0.015	5.1E14	0.07	-0.2	3.5E-4	4.1E0
36	HUM 12/19/75 20:10:58	S	3.0	1.34	7.3E-10	105		0.012	1.5E14	0.02	-0.5	1.3E-4	3.1E-1
37	HUM 12/19/75 19:55:44	P	3.0	1.29	1.0E-9	120	3.0	0.013	4.9E15	1.00	0.3	3.3E-3	5.0E2
37A	REFLECTION		3.0		1.0E-10	120							
38	HUM 12/19/75 19:55:44	S	2.5	1.29	1.0E-9	40		0.030	2.2E14	0.01	-0.4	1.3E-4	4.0E-2
39	HUM 12/19/75 19:53:02	P	3.0	1.27	8.0E-10	120	2.4	0.013	3.9E15	0.80	0.3	5.1E-3	3.2E2
40	HUM 12/19/75 19:53:02	S	2.0	1.27	1.1E-9	50		0.021	2.4E14	0.01	-0.4	5.6E-5	9.0E-2
41	GNC 02/05/76 00:18:23	all	2.0	0.74	4.4E-10	40		0.040	1.2E15	0.01	-0.0	4.0E-4	1.1E0
42	HUM 12/19/75 19:52:55	P	3.0	1.23	4.7E-10	110	2.2	0.015	2.2E15	0.31	0.1	1.5E-3	7.7E1
43	HUM 12/19/75 19:52:55	S	2.5	1.23	3.0E-10	50		0.024	6.3E13	0.01	-0.8	1.0E-4	6.0E-3
44	HUM 12/18/75 20:16:05	P	2.5	1.27	6.1E-10	118	1.1	0.014	2.9E15	0.50	0.2	3.0E-3	1.7E2
45	HUM 12/18/75 20:16:05	S	3.0	1.27	4.1E-10	110		0.011	8.8E13	0.02	-0.7	6.6E-5	1.2E-1
46	GNC 12/12/75 22:38:15	P	2.0	1.34	8.0E-11	62	0.9	0.016	4.1E14	0.03	-0.3	2.0E-4	4.8E-1
47	GNC 12/12/75 22:38:15	S	2.5	1.34	3.7E-10	66		0.016	8.9E13	0.01	-0.7	6.6E-5	2.7E-2
48	GNC 12/12/75 22:37:57	all	3.0	0.80	1.0E-9	70		0.024	3.0E16	1.00	0.8	8.1E-3	3.7E3
49	HUM 12/12/75 04:03:59	P	3.0	0.84	6.1E-11	90	1.0	0.016	1.9E14	0.01	-0.5	6.6E-5	3.2E-1
50	HUM 12/12/75 04:03:59	S	2.5	0.84	3.0E-10	86		0.014	4.3E13	0.01	-0.9	6.6E-5	1.4E-2

Table 1. (Continued)

ID#	Event	Phase	-γ	R E-5 cm	Ω(0) cm-sec	f_c	f_p/f_s	r E-5 cm	M_o dyne/cm	Δσ bars	M_L	$U_{d\,max}$ cm	E_R Joules
51	GNC 12/12/75 20:55:04	P	2.0	0.85	3.0E-10	51		0.024	9.7E14	0.01	-0.1	2.4E-4	1.5E0
52	GNC 12/12/75 20:55:00	all	2.0	1.27	1.8E-10	60		0.027	8.7E14	0.04	-0.1	6.2E-4	2.0E0
53	GNC 12/12/75 20:53:03	all	2.0	1.27	2.1E-10	50		0.032	1.0E15	0.04	-0.1	4.2E-4	1.5E0
54	HUM 12/12/75 03:12:53	P	2.5	1.38	2.0E-10	90		0.018	1.0E15	0.03	-0.1	4.7E-4	7.4E0
55	HUM 12/12/75 03:12:53	S	3.0	1.38	5.0E-10	105	0.9						
56	HUM 12/12/75 02:13:28	P	3.0	1.84	1.5E-10	92	0.9	0.017	1.0E15	0.03	-0.1	5.0E-4	9.3E0
57	HUM 12/12/75 02:13:28	S	3.0	1.84	5.0E-10	105		0.011	1.2E14	0.01	-0.6	1.1E-4	2.0E-1
58	HUM 12/13/75 02:19:16	P	3.0	1.40	6.0E-11	98	1.1	0.016	3.2E14	0.03	-0.3	1.6E-4	1.2E0
59	HUM 12/13/75 02:19:16	S	3.0	1.40	2.1E-10	90		0.013	5.0E13	0.10	-0.8	4.3E-5	2.0E-2
60	2-2-248-250	P	2.0	1.07	7.0E-10	87	0.8	0.014	2.8E15	0.44	0.2	2.0E-3	6.2E1
61	2-2-248-250	S	2.0	1.07	5.0E-10	103		0.007	9.1E13	0.10	-0.7	2.3E-4	1.0E-1
62	2-2-332-250	P	3.0	1.32	1.3E-9	120	1.6	0.013	6.5E15	1.20	0.4	5.2E-3	8.8E2
63	2-2-332-250	S	1.5	1.32	8.0E-9	73		0.011	1.8E15	0.70	0.1	2.4E-3	1.5E1
64	2-2-348-250	P	2.5	0.94	9.0E-10	120	1.3	0.013	3.2E15	0.60	0.2	2.6E-3	1.0E-1
65	2-2-348-250	S	2.0	0.94	1.8E-9	90		0.009	2.9E14	0.20	-0.4	5.9E-4	7.0E-1
66	2-2-655-250	P	3.0	0.94	1.0E-9	170	1.1	0.009	3.6E15	1.90	0.3	5.6E-3	7.6E-2
67	2-2-655-250	S	3.0	0.94	7.0E-10	160		0.008	1.1E14	0.22	-0.6	3.2E-4	6.0E-1
68	2-2-850-250	P	2.5		1.7E-10	127	1.2	0.013					
69	2-2-850-250	S	2.5		3.2E-10	105		0.012					
70	2-2-920	P	?	2.61	1.0E-10	?	?	?	?	?	?	?	?
71	2-2-920-250	S	2.5	2.61	1.6E-9	82		0.015	7.1E14	0.07	-0.1	3.5E-4	3.3E0
72	2-2-924-250	P	3.0	2.67	5.0E-9	157	1.8	0.008	2.4E15	0.20	0.2	4.8E-4	2.7E2
73	2-2-924-250	S	2.0	2.67	1.1E-9	86		0.009	5.0E14	0.31	-0.2	9.2E-4	1.9E0
74	2-2-1000-250	S	2.5	2.64	2.1E-9	83		0.014	1.0E15	0.09	-0.1	4.2E-4	6.9E0
75	2-2-1233-250	P	2.5	2.51	5.2E-10	110	1.3	0.015	5.0E15	0.71	0.4	3.5E-3	4.0E2
76	2-2-1233-250	S	2.5	2.51	2.4E-9	88		0.014	1.1E15	0.30	-0.1	1.2E-3	9.0E0

Table 1. (Continued)

ID#	Event	Phase	-γ	R E-5 cm	Ω(0) cm-sec	f_c	f_p/f_s	r E-5 cm	M_o dyne/cm	Δσ bars	M_L	$U_{d\,max}$ cm	E_R Joules
77	2-2-1298-250	P	2.0	2.67	3.2E-10	115	1.3	0.010	3.2E15	1.30	0.2	4.2E-3	1.9E2
78	2-2-1298-250	S	1.5	2.67	1.5E-9	87		0.009	6.8E14	0.43	-0.2	1.3E-3	3.7E0
79	2-2-1319-250	P	2.5	1.46	4.0E-9	90		0.018	2.2E16	1.74	0.7	1.0E-2	4.2E3
80	2-2-1371-250	P		2.51	1.0E-10	?							
81	2-2-1371-250	S		2.51	2.0E-10	80		0.015	8.5E13	0.01	-0.7	5.0E-5	4.0E-2
82	2-2-1382-250	P		0.97	2.0E-10	?							
83	2-2-1382-250	S	2.0	0.97	6.0E-10	81		0.010	1.0E14	0.06	-0.6	2.0E-4	6.0E-2
84	2-2-1425-250	P		2.72	1.0E-10	100		0.016	1.0E15	0.05	-0.1	5.8E-4	1.2E1
85	2-2-1425-250	S	2.0	2.72	1.5E-9	80		0.010	6.9E14	1.32	-0.2	1.1E-3	2.9E0
86	2-2-1435-250	P	2.0	1.27	6.0E-10	90	0.9	0.014	2.9E15	0.54	0.2	2.3E-3	7.3E1
87	2-2-1435-250	S	1.5	1.27	4.0E-10	105		0.007	8.6E13	0.13	-0.7	2.3E-4	1.0E-1
88	2-2-1475-250	P	1.5	1.77	5.2E-10	108	1.0	0.011	3.5E15	1.11	0.3	4.1E-3	1.9E2
89	2-2-1475-250	S	1.5	1.77	9.0E-10	105		0.007	2.7E14	0.31	-0.4	6.9E-4	1.0E0
90	2-2-1495-250	P	1.5	1.30	4.0E-10	105	1.2	0.011	1.8E15	0.51	0.1	2.0E-3	4.5E1
91	2-2-1495-250	S	3.0	1.30	2.0E-9	85		0.014	3.8E14	0.05	-0.3	6.0E-4	1.1E0
92	2-2-1558-250	P	3.0	0.97	4.0E-10	90	0.9	0.018	1.5E15	0.11	0.0	6.5E-4	2.0E1
93	2-2-1558-250	S	3.0	0.97	2.6E-9	105		0.015	4.3E14	0.13	-0.3	5.0E-3	2.4E0
94	2-2-1698-250	P	3.0	1.47	1.0E-9	108	1.3	0.015	5.6E15	0.80	0.4	3.8E-3	4.7E2
95	2-2-1698-250	S	3.0	1.47	3.6E-9	85		0.014	9.0E14	0.14	-0.1	6.5E-4	6.0E0
96	2-2-1748-250	P	3.0		1.3E-9	93	1.1	0.017					
97	2-2-1748-250	S	2.0		1.8E-9	88		0.010					
98	2-2-1780-250	P	2.5	1.64	2.0E-9	100	0.9	0.016	1.2E16	1.34	0.6	7.1E-3	1.7E3
99	2-2-1780-250	S	2.5	1.64	4.0E-9	110		0.011	1.1E15	0.40	-0.1	1.5E-3	1.9E1
100	2-2-1817-250	P	2.5	1.62	1.0E-10	100	1.3	0.016	6.2E14	0.11	-0.2	3.7E-4	4.6E0
101	2-2-1817-250	S	1.5	1.62	2.0E-10	80		0.010	5.5E13	0.08	-0.8	1.0E-4	2.0E-2
102	2-2-1860-250	P		3.01	4.0E-9								
103	2-2-1965-250	P	3.0	2.87	7.0E-10	120		0.013	7.6E15	1.42	0.5	6.1E-3	1.2E3

Table 1. (Continued)

ID#	Event	Phase	$-\gamma$	R E-5 cm	$\Omega(0)$ cm-sec	f_c	f_p/f_s	r E-5 cm	M_o dyne/cm	$\Delta\sigma$ bars	M_L	$U_{d\,max}$ cm	E_R Joules
104	2-2-1988-250	P		2.34	2.0E-10								
105	2-2-1988-250	S	2.0	2.34	3.0E-9	120		0.006	1.2E15	2.0	0.0	4.0E-3	3.0E1
106	2-2-2554-250	P	2.5	2.67	2.0E-10	110	1.0	0.015	2.0E15	0.30	0.1	1.4E-3	6.4E1
107	2-2-2554-250	S	2.5	2.67	4.0E-9	105		0.011	1.8E15	0.29	0.1	1.4E-3	1.1E2
108	2-2-2772-250	P	2.0	1.00	1.1E-9	99	1.0	0.010	2.3E15	1.03	0.1	3.3E-3	6.2E1
109	2-2-2772-250	S	2.0	1.00	2.6E-9	97		0.006	2.2E14	0.51	-0.5	1.5E-3	5.3E-1
110	2-2-2785-250	P	3.0	2.44	2.4E-9	105	0.9	0.015	1.1E16	1.43	0.6	1.1E-2	1.7E3
111	2-2-2785-250	S	3.0	2.44	3.0E-9	115		0.011	6.2E14	0.30	-0.2	1.0E-3	7.0E0
112	FRT Small CH1	P		3.74									
113	FRT9-792-CH1	P	3.0	4.20	1.1E-7	11.5	0.4	0.139	1.8E18	0.31	1.9	1.1E-2	5.9E4
114	FRT9-792-CH1	S	3.0	4.20	1.1E-7	30.0		0.040	7.9E16	0.50	1.1	8.8E-3	2.0E3
115	FRT9-806-CH1	P	1.5	5.30	3.0E-7	16.0		0.075	6.0E18	6.32	2.2	1.7E-1	1.8E6
116	FRT9-1207-CH1	P	2.0	3.74	3.0E-7	10.0	1.1	0.120	4.3E18	1.11	2.1	4.3E-2	2.2E5
117	FRT9-1207-CH1	S	2.0	3.74	5.0E-7	8.8		0.088	3.2E17	0.21	1.4	6.1E-3	8.4E2
118	FRT9-1238	P	3.0	4.04	1.4E-7	11.4	1.0	0.105	2.1E18	1.51	1.9	3.8E-2	7.8E4
119	FRT9-1238	S	1.5	4.04	5.4E-7	11.0		0.109	3.7E17	0.17	1.5	3.0E-3	2.2E3
120	FRT9-2354-CH1	P	1.5	3.88	1.0E-7	10.0		0.120	1.5E18	0.42	1.8	1.5E-2	2.7E4
121	FRT10-575-CH1	P	1.5	4.07	5.0E-7	17.0	1.5	0.071	7.5E17	0.93	1.6	2.2E-2	2.3E4
122	FRT10-575-CH1	S	3.0	4.07	4.0E-7	11.0		0.110	2.8E17	0.11	1.4	3.3E-3	1.3E3
123	FRT10-763-CH1	P	1.5	4.15	2.0E-7								
124	FRT10-765-CH1	P	3.0	4.15	4.0E-8	12.0		0.133	6.3E17	0.11	1.6	5.3E-3	8.3E3
125	FRT10-765-CH1	S	?	4.15	2.0E-8	?							
126	FRT10-1734-CH1	P	2.5	6.14	4.0E-7	11.0		0.145	9.3E18	1.32	2.3	8.8E-2	1.4E6
127	FRT10-1734-CH1	S	2.0	6.14	1.0E-6	?							
128	FRT11-855-CH1	P	3.0	2.61	4.6E-8	11	0.8	0.145	4.6E17	0.11	1.5	2.6E-3	3.4E3
129	FRT11-855-CH1	S	3.0	2.61	1.3E-7	13		0.092	5.8E16	0.04	1.0	7.3E-4	8.9E1

Table 1. (Continued)

ID#	Event	Phase	$-\gamma$	R E-5 cm	$\Omega(0)$ cm-sec	f_c	f_p/f_s	r E-5 cm	M_o dyne/cm	$\Delta\sigma$ bars	M_L	$U_{d\,max}$ cm	E_R Joules
130	FRT11-908	S	1.5	3.54	?	?							
131	FRT11-916-CH1	P	1.5	3.88	3.5E-8	8		0.150	5.2E17	0.08	1.5	3.5E-3	1.7E3
132	FRT11-916-CH4	P	?	3.88	1.0E-8								
133	FRT11-916-CH4	S	?	3.88	4.0E-8								
134	FRT11-961-CH4	P	1.5	3.80	2.0E-8								
135	FRT11-961-CH4	S	?	3.80	5.0E-8	80							
136	FRT11-961-CH1	P	1.5	3.80	5.0E-8	5.5		0.218	7.2E17	0.04	1.6	2.2E-3	1.0E3
137	FRT11-961-CH1	S	1.5	3.80	1.0E-7								
138	FRT11-1693-CH1	P	1.5	4.55	4.0E-7	5.4	1.1	0.220	6.9E18	0.30	2.2	2.0E-2	9.0E-4
139	FRT11-1693-CH1	S	3.0	4.55	3.0E-6	5.0		0.200	3.9E18	0.14	2.1	8.0E-3	2.3E4
140	FRT11-1837-CH1	P	?	4.08	?	?							
141	FRT11-1837-CH1	S	?	4.08	?	?							
142	FRT11-1838.5-CH1	P	2.5	4.41	1.0E-7	12.9	0.6	0.123	1.7E18	0.42	1.8	1.7E-2	7.4E4
143	FRT11-1838.5-CH1	S	1.5	4.41	1.6E-7	20		0.039	1.2E17	0.93	1.2	1.0E-2	1.4E3
144	FRT13-968-CH1	P	1.5	3.88	5.0E-8	12		0.100	7.4E17	0.30	1.6	1.0E-2	1.1E4
145	FRT13-968-CH4	P	?	3.88	3.0E-8	?							
146	FRT13-968-CH4	S	2.0	3.88	3.2E-7	10.3		0.070	2.1E17	0.20	1.3	5.1E-3	5.8E2
147	FRT13-1326-CH1	P	2.5	4.48	1.4E-7	14	1.4	0.114	2.4E18	0.73	1.9	2.8E-2	1.9E5
148	FRT13-1326-CH1	S	2.0	4.48	2.1E-6	10		0.120	1.6E18	0.41	1.8	2.0E-2	3.1E4
149	FRT13-1500=CH1	S	3.0	4.00	3.5E-7	43		0.028	2.4E17	4.81	1.3	4.4E-2	5.5E4
150	FRT16-1485-CH1	P	2.5	5.01	1.3E-7	21	0.4	0.076	2.5E18	2.00	1.9	5.0E-2	6.9E5
151	FRT16-1485-CH1	S	2.0	5.01	8.0E-7	16							
152	01/04/74-CH1	S	2.5	1.74	5.0E-7	55		0.022	1.5E17	5.83	1.2	4.2E-2	4.5E4
153	FRT-924	S	2.0		1.0E-9	80							
154	HHH 2 246	P	?	2.67	3.0E-10	?							
155	HHH 4 321	P	?	2.47	2.0E-10	?							
156	HHH 4 322	P	?	2.61	3.0E-10	?							

Table 1. (Continued)

ID#	Event	Phase	$-\gamma$	R E-5 cm	$\Omega(0)$ cm-sec	f_c	f_p/f_s	r E-5 cm	M_o dyne/cm	$\Delta\sigma$ bars	M_L	$U_{d_{max}}$ cm	E_R Joules
157	JAM 1 433	S	2.5	0.80	2.3E-8	21		0.057	3.1E15	0.04	0.2	1.9E-4	1.1E0
158	JAM 1 1203	S	3.0	1.27	8.0E-9	31		0.039	1.8E15	0.04	0.1	1.3E-4	1.2E0
159	Maryville 623	P	2.0	19.4	2.0E-6	3.5	0.5	0.343	1.5E20	1.60	2.9	1.8E-1	1.1E7
160	Maryville 623	S	2.0	19.4	6.0E-6	6.4		0.120	2.0E19	5.10	2.5	2.0E-1	1.2E6
161	Maryville 1295	P	2.0	21.0	1.5E-6	3.4	0.6	0.353	1.2E20	1.20	2.9	1.4E-1	5.7E6
162	Maryville 1295	S	2.0	21.0	1.1E-6	6.0		0.128	3.9E18	0.82	2.1	3.5E-2	3.9E4
163	Maryville 1450	P	2.0	12.0	5.0E-7	5.2	0.9	0.231	2.3E19	0.82	2.5	6.2E-2	8.9E+5
164	Maryville 1450	S	2.0	12.0	1.5E-6	5.5		0.140	3.1E18	0.51	2.0	2.2E-2	1.9E4
165	Maryville 985	P	2.0	20.0	6.0E-7	17.0		0.071	4.6E19	57.04	2.7	1.3E-0	1.2E8
166	Jocassee DFE 01/15/76	Surface											
167	Jocassee SGC 01/15/76	Surface											
168	PLS 11/08/75 21:18:48	Surface											
169	HUM 12/18/75 20:16:05	Surface											
170	GNC 12/12/75 20:55:04	Surface											
171	FRT 11 1896.5 CH1	Surface											
172	FRT13 1326 CH1	Surface											
173	FRT13 1326 CH4	Surface											
174	FRT13 1500 CH1	Surface											

CHAPTER VIII

DISCUSSION

Briefly summarizing, the general background of the study has been discussed, observed displacement spectra have been calculated and presented, recent displacement spectral theories have been reviewed, and values calculated by applying the theoretical equations to the observed displacement spectra. The final step is to use the information presented to form an interpretation of the microearthquake data. The preceding chapters have been fairly general in their descriptions. Interpretation involves examining some very specific cases; however, the interpretation will be discussed in general terms whenever reasonable. The discussion can be generalized somewhat by noting that the CHRA and the JRA spectra are similar enough that they can be grouped together. The MTA data differ from the data from the other data regions and will be discussed separately. Data from the CHRA and the JRA (Table 1) typically show sharp, well-defined spectral corners, ratios of f_p/f_s that are greater than unity, high frequency trends that decay in amplitude as ω^{-3}, and an absence of observed "intermediate" trends. Approximately 80% of the spectra from these two areas show high frequency decays proportional to either $\omega^{-2.5}$ or $\omega^{-3.0}$, with $\omega^{-3.0}$ being twice as common as $\omega^{-2.5}$. For a given event, both P- and S-wave spectra typically show the same order of decay. A few of the spectra suggest decay trends proportional to ω^{-4}, but these have been grouped with the ω^{-3} because of a lack of high frequency information in these particular spectra. The remaining 20% show ω^{-2} decay at high frequencies.

The absence of the "intermediate" trend is explainable in terms of four possibilities: (i) The rise time duration and the seismic far-field pulse duration are equal. (ii) The rise time interval is so short that the f_2 corner (Figure 20) is off the high frequency end of the instrument response (Savage, 1974). (iii) The "intermediate" trend and the "high" frequency trend have the same slope. (iv) The Brune (1970) definition is used to suggest a total stress drop. The first case seems to be a freak situation. If the second case is true and the third case is false, then the slopes should have been less than the ω^{-3} that was observed (Figure 20). Molnar <u>et al</u>. (1973) explain spectral corners in terms of destructive interference which requires that a hole (i.e., a very small portion of the spectrum where the amplitude temporarily drops to zero, which shows as an inverted spike in the spectrum) be present in the spectrum at each spectral corner (Madariaga, 1976). However, an observed spectrum is so full of holes from irregularities in the fault surface and inhomogeneities in the propagation path that positive identification of the f_2 corner frequency hole is not easily accomplished. Thus, if the slope of the intermediate and high frequency trends are equal, the f_2 spectral corner is not observable and neither is the "intermediate" trend.

A high frequency trend of ω^{-3} implies a quadratic singularity in the time function associated with either the initial rupture (Dahlen, 1974) or with the termination of rupture (e.g. Savage, 1974). A quadratic rise-time was discussed in Chapter VI in terms of a convolution. Similarly, Savage (1974) explains the high frequency singularity as being a convolution of the final slip function with the stopping phases. The subsonic model presented by Madariaga (1976) relates the slope of the "intermediate" trend to the order of the discontinuity of the stopping phase such that the slope is proportional to ω^{-2} for values of θ between 30 degrees and 45 degrees. However, the slope undergoes a transition to $\omega^{-1.5}$ for θ greater than 45 degrees. I interpret the Madariaga (1976) subsonic model to mean that the order of the stopping phase varies with azimuth from $t^{0.5}$ to t^{1}. If this is true, then a convolution with the final slip function as suggested by Savage (1974) gives a trend which varies from $\omega^{-2.5}$ to ω^{-3} as azimuth decreases. This is one possible explanation of the presence of both slopes in the data set (Table 1). This premise can be checked by noting that the Madariaga (1976) transonic model requires that the f_p/f_s ratio decrease with decreasing azimuth (Figure 24). For azimuths less than approximately 30 degrees, the ratio should be less than unity. This implies that if the above interpretation is reasonable, then microearthquakes showing high frequency trends of ω^{-3} should be associated with ratios of f_p/f_s closer to unity than those showing trends of $\omega^{-2.5}$. The observed data presented in Table 1 support this premise.

An alternative explanation is possible in terms of the Brune "intermediate" trend. If the Brune (1970-71) model is adjusted to an inverse cubic decay as suggested by equation (31), then the "intermediate" trend resulting from a fractional stress drop matches the slope of the Madariaga "intermediate" trend. Madariaga (1976) apparently uses a complete effective stress drop which suggests that his "intermediate" trend is truly different. A comparison of the definitions of the corner frequency characteristic of the fault dimensions offered by each study suggests that the "intermediate" trend of Madariaga (1976) corresponds to the "high frequency" trend of the Brune (1970) model. A partial effective stress drop should manifest itself as a rounding off of the f_1 spectral corner (Figure 20). This explanation allows the previous explanation to still be used to explain the presence of ω^{-3} and $\omega^{-2.5}$ trends. Even if the model of Brune (1970) is used independent of the earlier explanation, the interpretation of the spectra as being related to a transonic equidimensional model will not be changed.

Approximately 20% of the CHRA spectra show high frequency trends of ω^{-2}. Molnar et al. (1973) find that at certain values of the azimuth, constructive interference will result in the high frequency trend being an inverse square frequency function instead of the expected inverse cube frequency function. However, for transonic rupture velocities, the P- and S-waves will not experience constructive interference at the same azimuth. The observed results support this premise by showing that 72% of the micro-earthquakes in question produce an inverse square decay for only one phase (usually the S-wave).

Do the microearthquakes at the CHRA occur along a single plane, or are a number of planes (not necessarily parallel) required to explain the spectra? This question is answered by considering the effect of azimuth on the f_p/f_s ratio. First, one can determine that azimuth does indeed play an important role by observing the spectra of the 01/15/76 microearthquake which was recorded on three stations (DFE, SGC, and ESD) at the JRA (Figure 3). Stations DFE and SGC show $f_p/f_s = 2.0$ while station ESD shows $f_p/f_s = 1.0$. All three stations were very close to the hypocenter and were located on the same geologic unit; thus, the variation must be a reault of azimuth. At station HUM in the CHRA, the value of the f_p/f_s ratio varies by a factor of three for microearthquakes recorded at the same hypocentral distance (see Table 1, Nos. 41 and 45). This requires that azimuth vary by at least 25 degrees (see Burridge, 1975). If only a single plane exists, then the hypocentral distance must change to allow a variation in azimuth at a single station. Note that the hypocentral distance did not change for these events which implies that they occurred along two different planes not parallel to each other assuming both occurred in the same immediate epicenter. Are only two planes important or are there others? If microearthquakes are occurring along numerous surfaces, not all of which are parallel, then one could expect to record events at a variety of fault orientations (i.e. different azimuths). A similar effect can be obtained theoretically by fixing a single plane within a focal sphere and sampling the azimuthal effects at different points along the surface of the sphere. Studies by Madariaga (1976) and Burridge (1975) predict that one should observe f_p/f_s to be greater than unity for approximately 70% of the surface of the focal sphere. Table 1 indicates that approximately 70% of the CHRA microearthquakes produce values of f_p/f_s that are greater than or equal to unity. This is good evidence that the CHRA microearthquakes are presently occurring along multiple planes.

This premise is supported by two additional considerations. Scheffler (1976) explains a majority of the aftershocks of the August 2, 1974, earthquake in terms of a single plane which if extended intersects the surface along a feature that appears to be an ancient shear zone based upon surface geology. Microearthquakes recorded recently (September,

1976) on the Georgia Tech telemetry system indicate an active area on the Georgia side of the Savannah River near Fishing Creek, approximately ten kilometers from the previous epicenter. This new epicenter is not on a direct extension of the shear zone, indicating that more than one plane of faulting exists in the CHRA. Also, Bridges (1975) concludes on the basis of hypocentral plots that aftershock activity probably occurred along two or more fault planes. Thus, considering these two points and especially the spectral results of this thesis, I conclude that microearthquakes are occurring in the CHRA along multiple planes, not all of which are parallel.

The spectra for the CHRA and the JRA are best explained in terms of a model which (i) nucleates rupture at a point, (ii) results in moderately high to very high frequency content, (iii) ruptures transonically, and (iv) is not confined to a single orientation. On the basis of these conditions, one can propose a possible model of faulting. Bridges (1975) notes that stress amplification at corners may be able to explain the fracture of brittle rocks in the area. This process is investigated in terms of regional tectonics by Long and Hsiao (1976) and Hsiao (1977). This certainly explains the high frequency content, but not the transonic rupture which requires a well-lubricated dislocation surface. Field observations of the rocks exposed along the lake front reveal that the region is highly jointed in multiple orientations. Denman (1974) states that four sets of joints are common (NE, NW, ENE, NNE). The NE and NW sets seem to be predominant. The joint surfaces must certainly be well lubricated because of the presence of a naturally high water table. These surfaces certainly meet the requirement for a transonic slip which occurs if the static friction is less than the total stress acting (i.e. $5.357T_o$). They also allow microearthquakes to occur in multiple orientations. A combination of these concepts can explain both the high frequency content and the transonic rupture of an average spectrum. If the dislocation surface is locked by a rough surface, incomplete jointing, or one of the many dikes or veins, then sufficient stress must accumulate to fracture these brittle structures (stress amplification). Once the locking structure has been sheared, the remaining stress produces rupture at transonic velocities along the well lubricated joint surface. Thus, one observes a high frequency transonic earthquake.

This general model can be taken to two extremes. One extreme is the case of slip along a smooth surface that is not locked by a brittle material. The spectrum should show the ω^{-3} trend characteristic of a transonic rupture, a relatively low corner frequency, and a low stress drop (e.g. number 26 of Table 1). The other extreme case is that of brittle fracture only. This case should produce a spectrum showing a high stress drop, a high corner frequency, and the ω^{-2} to $\omega^{-2.5}$ slope characteristic of a subsonic rupture. Some of the spectra presented appear to have corner frequencies higher than the instrumentation is capable of recording. Spectra numbers 77 and 80 are very similar except that insufficient high frequency information was recorded in number 77 to show the high frequency trend. Number 77 does show a rounding off and a spectral hole, both of which are characteristic of a spectral corner, at approximately 200 Hertz. A number of spectra are similar to number 77, suggesting that brittle fracture may be an important source mechanism.

Although the data included in this thesis from the JRA are insufficient to perform a detailed analysis, one can guess that the slip process must be at least similar to the CHRA events because the spectra from the JRA are very similar to the CHRA spectra. The JRA microearthquakes are in part triggered by reservoir impounding (Fogle et al., 1976).

The MTA spectra are decidedly different from the CHRA and JRA spectra. The MTA spectra show an amplitude decay which is proportional to $\omega^{-2.0}$ or $\omega^{-2.5}$. The spectra also show a relatively smooth transition at the spectral corners, and values of the ratio f_p/f_s less than unity. The inverse square trend can be explained in terms of subsonic models presented by Savage (1974) and Madariaga (1976) or in terms of the transonic Brune (1970) model. The justification given for the ω^{-2} decay in the CHRA-JRA data discussion is not acceptable here because both P-waves and S-waves decay at the same rate. The most realistic model is the Madariaga (1976) model (Figure 20). If compared to this model, the MTA spectra show the low and intermediate portions but only a small portion of the high frequency trend. Using the earlier interpretation of the relation of the Brune and Madariaga models, the rounded spectral corners are characteristic of a partial stress drop. Thus, the MTA spectra may be modeled as a nearly equidimensional rupture zone rupturing subsonically and experiencing a premature arrest of slip. These spectra can also be explained as long narrow faults by following the Savege (1972) and the Aki (1967) kinematic models, but the circular Madariaga (1976) dynamic model may be more realistic.

Does the fact that the MTA microearthquakes were recorded during an immediate aftershock sequence explain why they differ from the CHRA-JRA microearthquakes? The spectra for the CHRA station FRT are calculated from records of microearthquakes recorded by S. R. Bridges during the immediate aftershock of the August 2, 1974, earthquake in the CHRA reported in Bridges (1975). These FRT station data compare favorably with other CHRA microearthquake spectra that were not immediate aftershocks. Thus, simply being aftershocks will not explain why the MTA and CHRA-JRA spectra differ.

The spectra for the MTA show a spectral shape characteristic of a subsonic rupture. This can be explained by requiring that the aftershocks either occurred on surfaces with cohesion greater than 5.357 T_o or that they had to form their own rupture surface. This explanation is supported indirectly by a study (Bollinger _et al_., 1976) of the MTA earthquake of November 30, 1973, which concludes that the focal mechanism of the main shock and the focal mechanisms of the aftershocks do not match. Two orientations of faulting can be defined. One orientation is N-S and the other trend is E-W. Apparently the aftershocks did not occur along the predefined rupture zone of the main shock, but rather had to form their own surfaces.

Table 2 presents spectral estimates of stress drop for microearthquakes from other studies. The typical stress drop of the CHRA microearthquakes is slightly greater than the typical value of four studies and less than those of two studies. Although this seems to indicate that the CHRA values are slightly high, they certainly are not extreme, being about an order of magnitude larger than the smallest reported value and about an order of magnitude smaller than the largest. However, the CHRA spectra do suggest a complete stress drop and the maximum value obtained (6.3 bars) agrees well with the value for the main shock of August 2, 1974 (Bridges, 1975). Also, recall that a number of CHRA spectra suggested very high stress drop, but high frequency resolution was insufficient to form a definite conclusion. The JRA stress drops tend to be slightly lower than the CHRA values. The MTA data produced less consistent values, making comparison more difficult.

Table 2. Comparison of Data to Published Observational Results

Area or Paper	~ M_L	Phase	$\Delta\sigma$ (bars)
CHRA	-0.5 to 2.3	PZ	0.1 to 6.3
CHRA	-0.8 to 2.1	SV	0.1 to 5.8
JRA	0.2 to 0.8	PZ	0.1 to 1.1
JRA	-0.4 to 0.2	SV	0.1 to 0.2
MTA	2.0 to 2.9	PZ	0.8 to 57.0
MTA	2.0 to 2.5	SV	0.5 to 5.1
Bakum *et al.* (1976)	0.9 to 2.4	PZ	0.1 to 245.3
Bakum *et al.* (1976)	0.9 to 2.4	SH	0.1 to 5.9
Brune and Allen (1967)	3.6	Love	1.1
Douglas and Ryall (1972)	1.0 to 2.0	S	0.04 to 0.6
Johnson and McEvilly (1974)	2.4 to 2.6	Whole Record	0.5 to 1.0
Thatcher and Hanks (1973)	2.0 to 3.0	SH	0.5 to 0.9
Tucker and Brune (1973)	1.4 to 3.0	SH	1.0 to 100.0
Wyss and Brune (1968)	3.1 to 3.4	Love	0.2 to 0.7

CHAPTER IX

CONCLUSIONS

The conclusions presented in this chapter are divided into two sections. The first section consists of conclusions not dependent upon personal interpretation. This section is effectively a summary of the displacement spectral properties observed. The second section consists of conclusions drawn from interpretation of the displacement spectra.

I) Conclusions based solely upon observed spectral properties include:

(1) The Clark Hill Reservoir area (CHRA) and the Jocassee Reservoir area (JRA) spectra are very similar while the Maryville, Tennessee, (MTA) spectra differ.

(2) Spectra from the CHRA and the JRA typically show high frequency trends proportional to $\omega^{-2.5}$ and ω^{-3} with the ω^{-3} trend being twice as common as the $\omega^{-2.5}$ trend.

(3) Spectra from the MTA typically show ω^{-2} trends with $\omega^{-2.5}$ trends sometimes being present for short high frequency segments.

(4) The CHRA and JRA spectra show sharper transitions at spectral corners than do the MTA spectra.

(5) For all data regions, a given microearthquake generally produces the same high frequency amplitude decay trend for both P- and S-waves.

(6) The CHRA spectra result in values of the f_p/f_s ratio both greater than unity and less than unity. The JRA spectra show only values greater than unity and the MTA spectra produce only values less than unity.

II) Conclusions derived from interpretation include:

(7) The CHRA and the JRA spectra are best modeled by an equidimensional (circular) fault which nucleates rupture at a point and ruptures transonically.

(8) High frequency content and stress drop of the CHRA microearthquakes are explainable in terms of brittle fracture while the transonic slip is explained in terms of well-lubricated pre-existing surfaces, both of which appear to exist in the geology of the CHRA and may combine to produce the high-frequency transonic earthquakes.

(9) Variations from $\omega^{-2.5}$ to ω^{-3} in the high frequency trends of both the CHRA and the JRA spectra are explained in terms of variations in azimuth, where azimuth refers to the orientation of the fault plane in three-dimensional space.

(10) The infrequent ω^{-2} high frequency trend in the CHRA and the JRA spectra is the result of constructive interference at certain azimuths.

(11) The value of the ratio of corner frequencies, f_p/f_s, does vary with azimuth such that values of the ratio greater than and less than unity are justifiable.

(12) The value of the ratio of corner frequencies is not a function of magnitude over the range studied.

(13) The microearthquakes at the CHRA occur on numerous planes not all of which are parallel.

(14) Peaks at the spectral corner in the CHRA and the JRA spectra are related to the small fault dimensions and to resonance.

(15) For the CHRA epicenter, $Q_p = 500$ and $Q_s = 250$ (see Appendix D).

(16) The MTA spectra are best modeled by a subsonic rupture occurring on either circular or elongated (probably circular) faults which may show premature stick.

CHAPTER X

RECOMMENDATIONS

(1) Focal mechanisms for a number of CHRA earthquakes should be calculated to help decide the question of the number of planes and orientations present.

(2) Spectra should continue to be calculated and catalogued to acquire a better statistical sample.

(3) The magnitude relation needs to be adjusted for use in the Southeast.

(4) The effects of stress amplification should be investigated more thoroughly to determine their significance.

(5) The tape units need a clock-oscillator to supplement the WWV radio time during periods of poor reception. A light could also be installed to improve the ease and efficiency of night operations.

(6) The digitizing technique used for this report, although accurate, is ridiculously slow. The A/D converter should be perfected so that this method will not have to be used again.

(7) Hope for earthquakes (both in old and new epicenters).

APPENDIX A

CALIBRATION OF THE TOTAL SYSTEM

The Geophone-Amplifier Subsystem

Calibration of the geophone-amplifier subsystem (Figure 26) is accomplished by comparing the output voltage of a 15 Hertz exploration geophone, which has been modified by the installation of a X1000-gain amplifier inside the geophone case (hereinafter referred to simply as the exploration geophone) to the output voltage of a 1-Hertz Mark Products, Inc. model L-4C geophone, which has been independently calibrated. The problem is two-fold: i) to isolate the geophones from background noises and ii) to drive the geophones at a known frequency such that both geophones respond to the same motion.

The problem of isolating the system was solved by constructing a suspension platform which has an effective natural frequency of less than one Hertz. The major source of background noise was a building vibration. To determine a reference level, the exploration geophone was placed directly on the floor, which showed a very consistent value of 3.8 volts peak to peak at 14.8 Hertz. Placing the exploration geophone on 18 inches of foam rubber effected a reduction of 38:1, which was not accepted. A shake table (suspension platform) was constructed by suspending a rigid platform from a rigid structure by means of elastic bands. This system effected a noise reduction of 190:1, which means a voltage level 0.25% of the saturation level of the geophone or 0.5% of the

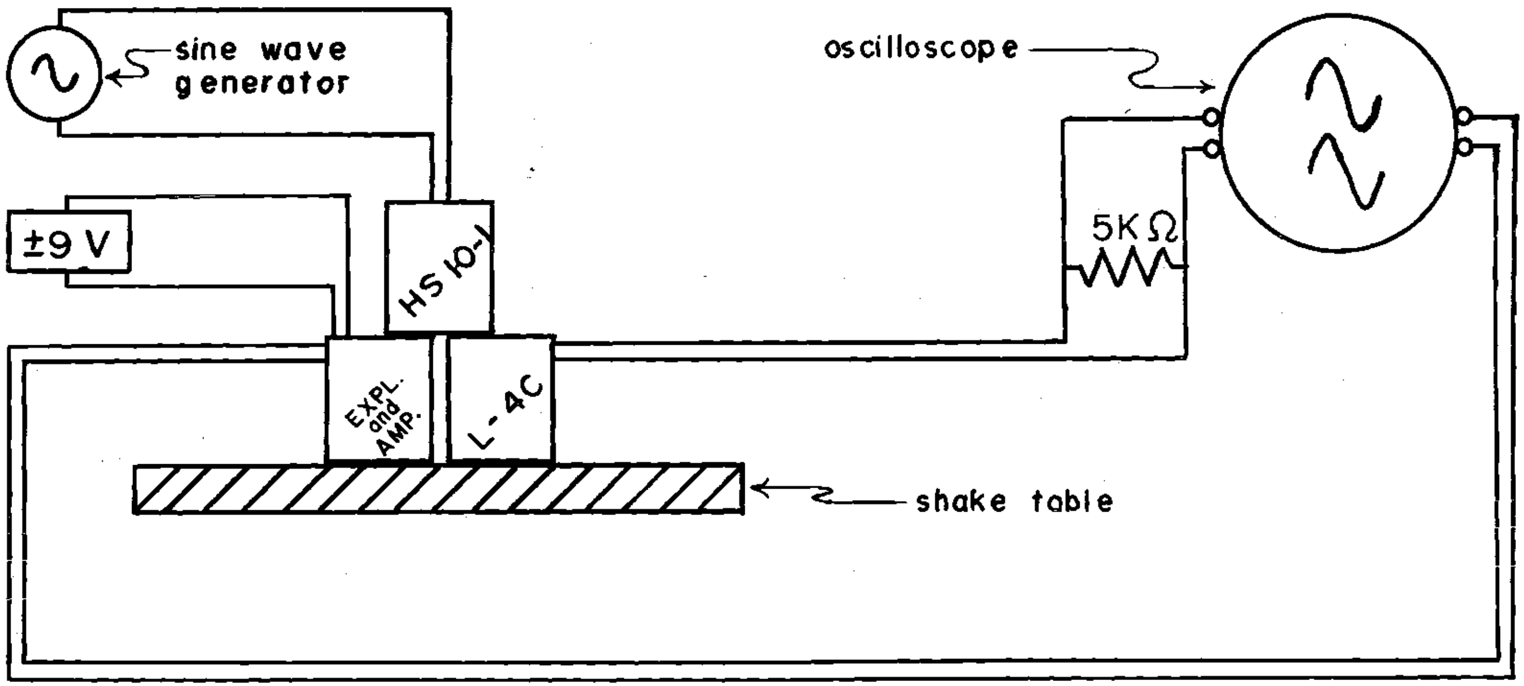

Figure 26. The Exploration Geophone - Amplifier Subsystem Setup.

saturation level of the tape recorder. In the calibration, the driving force is provided by a sine wave generator driving a Hall-Sears model HS10-1 vertical geophone which has a natural period of one second. The components of the system are coupled such that both test geophones respond to the same motion. The shake table must be kept level to avoid error due to tilt of the geophones.

The damping of the L-4C is determined by (Mark Products, Inc., 1975)

$$b_c = \frac{1.1\ R_c}{R_c + R_s} \tag{55}$$

where R_s = resistance of the shunt

R_c = resistance of the L-4C coil

The L-4C used in this test has a coil resistance of 5500 ohms. Therefore

$$b_c = 0.58 \tag{56}$$

The total damping is given by (Mark Products, Inc., 1975)

$$b_t = b_o + b_c \tag{57}$$

where b_o = damping of the L-4C without a shunt

$= 0.86$

Response curves supplied by Mark Products, Inc. for this L-4C geophone show that for a total damping of 0.86 the transduction at 40 Hertz is 3.58 volt in^{-1} sec. The ratio of the output voltage of the exploration geophone to the output voltage of the L-4C geophone is used to determine the transduction of the exploration geophone. At 40 Hertz the relative amplitude was measured as

$$\frac{\text{exploration}}{\text{L-4C}} = \frac{4.0\ \text{volts}}{2.0\ \text{mv}} = 2000{:}1 \qquad (58)$$

$$\begin{aligned}\text{Exploration Geophone Transduction} &= (2000)(3.58\ \text{volt in}^{-1}\ \text{sec}) \\ &= 7{,}160\ \text{volt in}^{-1}\ \text{sec} \\ &= 282\ \text{volt mm}^{-1}\ \text{sec} \qquad (59)\end{aligned}$$

The plot of the relative amplitudes is scaled such that the transduction of the exploration geophone at 40 Hz is 282 volt mm^{-1} sec (Figure 7). Note that the exploration geophone is slightly underdamped and shows a slight resonance at 20 Hz. This is useful because the underdamping helps compensate for the low frequency roll-off of the tape recorder subsystem (Figure 8).

The Tape Recorder Subsystem

The tape recorder subsystem is composed of the signal mixer circuit and the tape deck. Unit volume is arbitrarily chosen to occur at 100 Hz because this frequency is well within the reliable response range of the instrument and because microearthquakes with corner frequencies on the order of 100 Hz were anticipated. A controlled signal of a constant amplitude is put into the system such that the signal passes through the signal mixer circuit and is recorded (Figure 24). The recording volume adjustment of the deck is calibrated such that the voltage recorded equals the voltage put in. To determine the response of recording, a record is made as the input signal is varied from 1 Hz to 3500 Hz. The tape recorded during this last step is now played and the output of the tape is monitored (Figure 25) after adjusting the playback volume to give unit amplitude at 100 Hz. The above procedure is repeated for each of the three tape units. Tapes from each unit are played on the other units to document any possible errors produced by interchanging tapes (Figure 26). Because the tape units are similar, an average of the response curves is used as the instrument response. Figure 8 shows the maximum possible error in recording and playback. The maximum deviation results because the tape unit that has the strongest recording response also has the strongest playback response, and similarly for the weakest response. By interchanging tapes, one can keep the response much closer to the average value as shown in Figure 26.

The Stripchart Signal-Separator Subsystem

The response of the stripchart signal-separator subsystem (Figure 27) is determined by putting a constant amplitude signal into the signal-separator from a sine wave generator while varying the frequency from 1 Hertz to 300 Hertz. The response of the stripchart is affected by the amplitude and by the center position of the pen. Amplitudes begin to lose linearity if the displacement is greater than ±12.5 mm for the 20 mv/mm setting or ±5 for the 50 mv/mm setting. These errors are most significant above 100 Hertz.

The velocity response of the total system is determined by combining the response curves of the subsystems (Figure 10). The displacement response for the total system is determined by multiplying each value of the transduction by the corresponding value of the angular frequency (Figure 11).

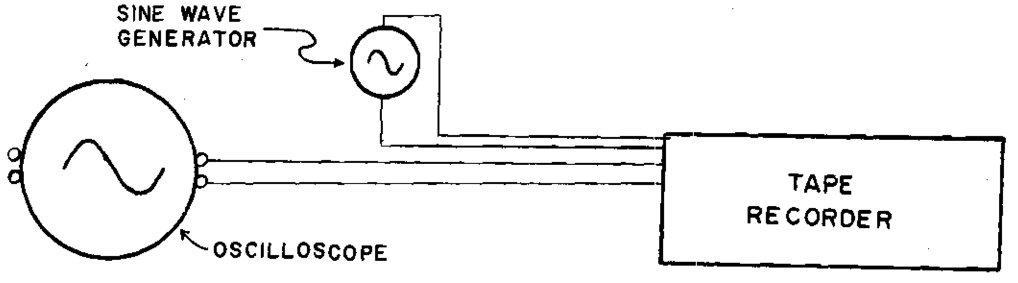

Figure 27. The Tape Recorder Subsystem Recording
Calibration Setup.

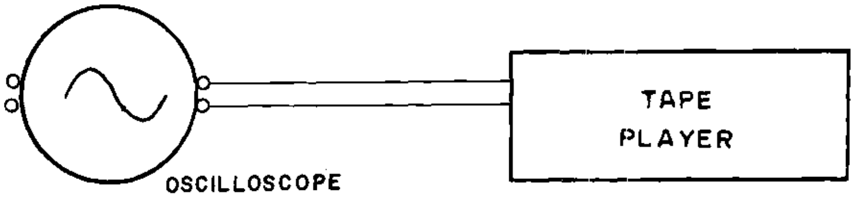

Figure 28. The Tape Player Subsystem Playback
Calibration Setup.

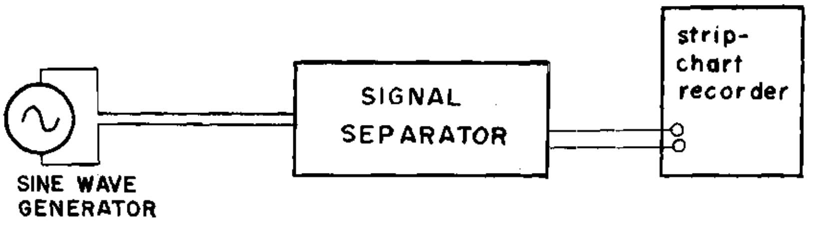

Figure 29. The Signal Separator - Stripchart Recorder
Subsystem Calibration Setup.

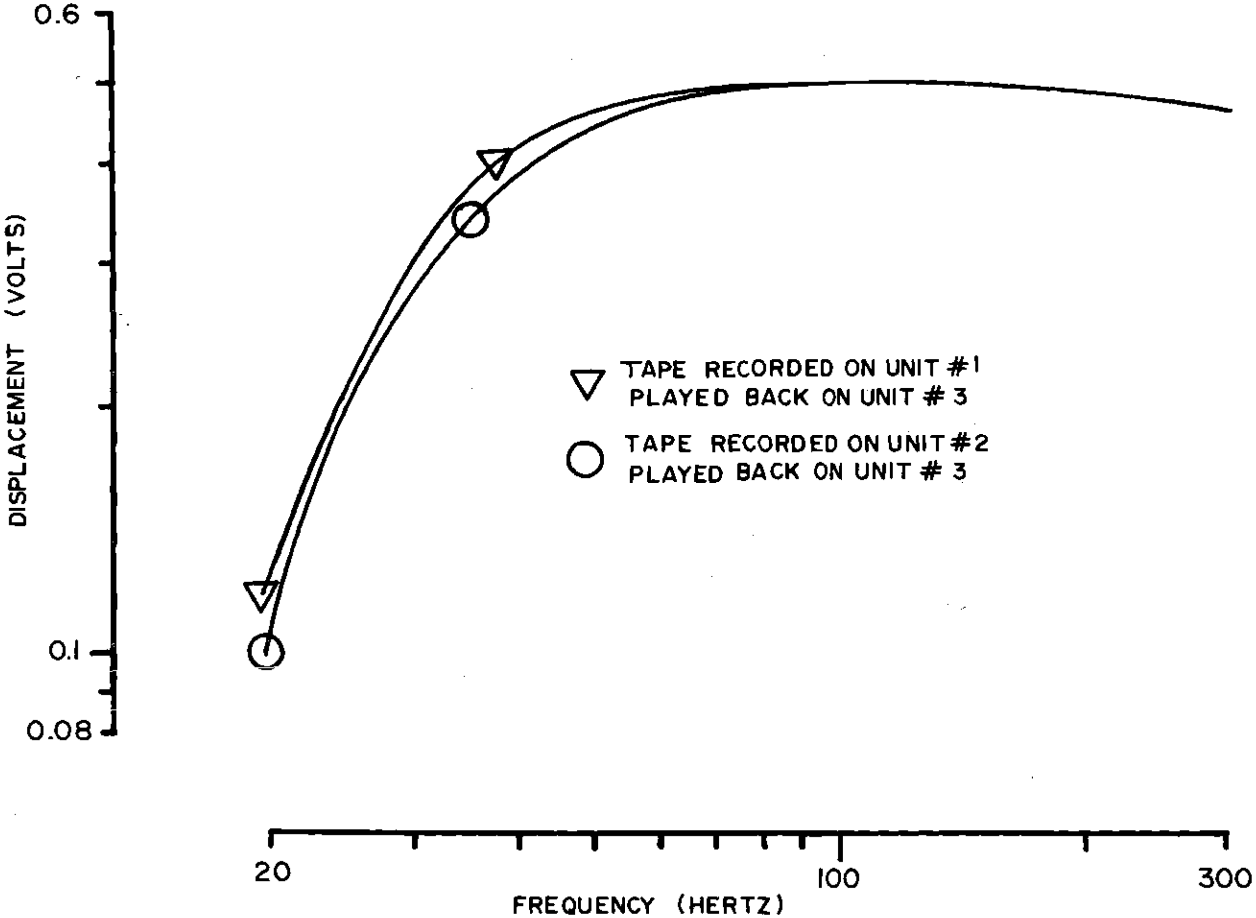

Figure 30. The Combined Recording and Playback Response with Tapes Interchanged. (Note that curves stay near the average value of Figure 8.)

Table 3. Percent of Amplitude Input that is Preserved

Frequency	% of Signal Amplitude Input to Tape Recorder That is Recovered	% of Signal Amplitude Input to the Stripchart-Signal Separator that is Recovered	% of Signal Amplitude That is Preserved on the Strip Chart Record	Frequency
10 Hz	6%	99.9%	6%	10 Hz
15	17	99.9	17	15
19				19
20		99.0	30	20
20.5				20.5
21	32			21
23.5			39	23.5
24	40	97		24
27	49			27
30	56	96	54	30
34	66			34
40	77	94	73	40
44	82			44
50	88	91	80	50
60	92	88	81	60
70		84	79	70
80		80	77	80
90	99.5	78	77	90
100	100	76	76	100
125		62	62	125
150	99.5	44	44	150
200	98	26	26	200
250	96	14	13	250
300	92	8	7	300

APPENDIX B

DYNAMIC RANGE

The Sony model TC-800B tape deck saturates at ±4.0 volts, while the geophone-amplifier system saturates at ±8.0 volts. For a background level of one millivolt, ±4.0 volts gives a dynamic range of 4000:1. The minimum background level discernible on the strip chart recorder without the aid of magnification is five millivolts which suggest a maximum practical dynamic range of 800:1. A typical value of the background seismic level experienced during actual field monitoring is ±12.7 millivolts which gives a typical dynamic range of 315:1 for the events in this report. A ground motion of 3.3×10^{-8} cm at 150 Hz will produce an output voltage of 0.5 volts for the X10 gain setting. The 20 mv/mm setting of the stripchart recorder will write the trace of a 0.5 volt signal as 2.5 cm. This gives a maximum magnification for the total system of 7.6×10^{7}:1, or 79 db (db is given by Marion (1970) as 10 log (relative amplitude)). The same ground displacement would show a 69db magnification for the X1 gain step. The maximum particle velocity that the system will record is 0.068 cm/sec at 60 Hz. For the X1 gain step the maximum is 0.009 cm/sec. The maximum particle displacement recordable is 1.1×10^{-5} cm at 150 Hz. For the X1 gain step the maximum is 2.7×10^{-6} cm at 150 Hz. Although the system is set for unit calibration, one may wish to play small events at full volume. If the event is recorded at unity and played at full volume, the resulting trace can be corrected to unity by the constant 0.7925. Also, a number of events were recorded prior to the calibrating of the system. These are corrected to unit volume by the arbitrary constant 0.5.

APPENDIX C

ERROR ANALYSIS

The quality of the displacement spectra are limited only by the corrections applied to the original data. Unfortunately, an exact recording of a physical process cannot be made; therefore, one must consider the precision and accuracy of the technique as a means of determining the limits of the observed results and as a means of suggesting improvements. The term "error" refers to estimated uncertainties in the analysis and is expressed in terms of a standard deviation. "Precision" is a measure of the random errors, and "accuracy" is a measure of the systematic errors (Beers, 1958). Random errors (e.g. reading error, background noises, etc.) are small because they tend to average to zero. However, there are a number of systematic errors mainly related to the averaging of curves. The error in the geophone-amplifier subsystem curve appears to be ±1.6% while the error in all of the other individual curves appears to be ±1.4%. If each tape recorder and each setting of the stripchart recorder had been used independently, a total of at least eighteen total response curves would have been needed to cover the combinations of tape recorders and stripchart settings. Each total displacement response curve would have had an error of approximately ±2.1% in frequency and amplitude. Instead, curves were averaged to form a single total displacement response curve.

The standard deviation is

$$s = \left(\frac{\sum_{n=1}^{k} (\delta\ x_n)^2}{K-1} \right)^{1/2} \tag{60}$$

The fractional standard deviation is

$$S = \frac{s}{\overline{x}} \tag{61}$$

where $\overline{x}$ is the average value.

The fractional standard deviation of a single product combines as

$$S_V = (S_x^{\ 2} + S_y^{\ 2})^{1/2} \tag{62}$$

where $V = xy$ or $V = x/y$.

When the three curves in Figure 8 or the two curves in Figure 9 are combined, the equation

$$s_{\overline{x}} = [\frac{1}{K^2} (s_{x_1}^2 + s_{x_2}^2 + \ldots s_{x_k}^2)]^{1/2} \tag{63}$$

is used to find the standard deviation of the resulting average curve. The resulting errors are a function of frequency and are presented as fractional standard deviations in Table 4. Equation (63) is used to combine the average curves for each subsystem into a single total response curve with the errors being presented in Table 4. Multiple test suggests that the digitization process is no worse than ±5%. Thus, the spectra presented in this report have an error in amplitude varying with frequency from ±5.4% to ±31% while the frequency is a consistent ±5.4%. The value of ±31% is the maximum error, and is rarely encountered (refer to Appendix A). The interpretation of the spectra should be weighted in favor of frequencies between 30 Hz and 120 Hz. Additional error is induced by fitting asymptotic lines to the spectra. Therefore, the values of spectral amplitude and corner frequency are correct to within an error of ±10%.

Table 4. Error of the Calibrating Process

Hz	Stripchart Signal Separator	Tape Recorder Subsystem	Total System	Total System Plus Digitization
15	± 1 %	± 28 %	± 28 %	± 29 %
20	1	26	26	27
25	1	15	15	16
30	1	9.5	10	11
35	1	7	7	9
40	1	4	4	6.4
45	1	3	3.5	6.1
50	1	2.2	2.8	5.7
60	1	2.1	2.7	5.7
70	1	2.0	2.6	5.6
80	1	1.0	2.1	5.4
90	1.7	0.8	2.4	5.5
100	2.5	0.8	3.0	5.8
120	6	0.8	6.2	8.0
150	18	0.8	18.0	19.0
200	27	0.8	27	27
250	31	0.8	31	31
300	± 18 %	± 0.8 %	18 %	19 %

APPENDIX D

ATTENUATION

The displacement spectra have been calculated as if no amplitude were lost during propagation due to inelastic properties. However, attenuation must be accounted for before performing interpretation. The proper quality factor (Q-value) is chosen and attenuation is applied to the theoretical curves before fitting them to the observed spectra. However, an arbitrary Q-value cannot be used because a variety of different curves can be made to fit a given spectrum by simply varying the Q-value. A Q-value is established for the epicentral area of the CHRA by applying the method of spectral ratios of local quarry explosions (Figure 31). Explosions are used because a given frequency will experience the same attenuation independent of the source. Explosions allow one to set up refraction lines, thereby eliminating azimuthal effects. If attenuation were negligible, then the seismic wave would not lose any amplitude causing the spectrum calculated at each station to show exactly the same spectral slope. Thus, by comparing spectral slopes for a given explosion (Figure 32), one can determine the Q-value. Attenuation is assumed to obey (from Douglas and Ryall, 1972)

$$\text{Attenuation} = \exp\left(\frac{-\omega R}{2Qc}\right) \tag{64}$$

such that Q is the only unknown.

Two explosions of equivalent force detonated within a very restricted area were used. The blast of 06/17/76 was recorded at stations CH6, CH5, MPB and LCC while the record at SBS is of the 04/29/76 blast. Three pairs are formed: MPB-LCC, LCC-SBS, and CH6-CH5. A value of $Q_p \doteq 500$ is obtained for each pair. Studies by Savage (1966B) and Walsh (1966) suggest that Q_s should be half the value of Q_p; thus, $Q_s \doteq 250$. This happens to be the same two values used by Molnar, et al. (1973) for the February 9, 1971, San Fernando earthquake sequence.

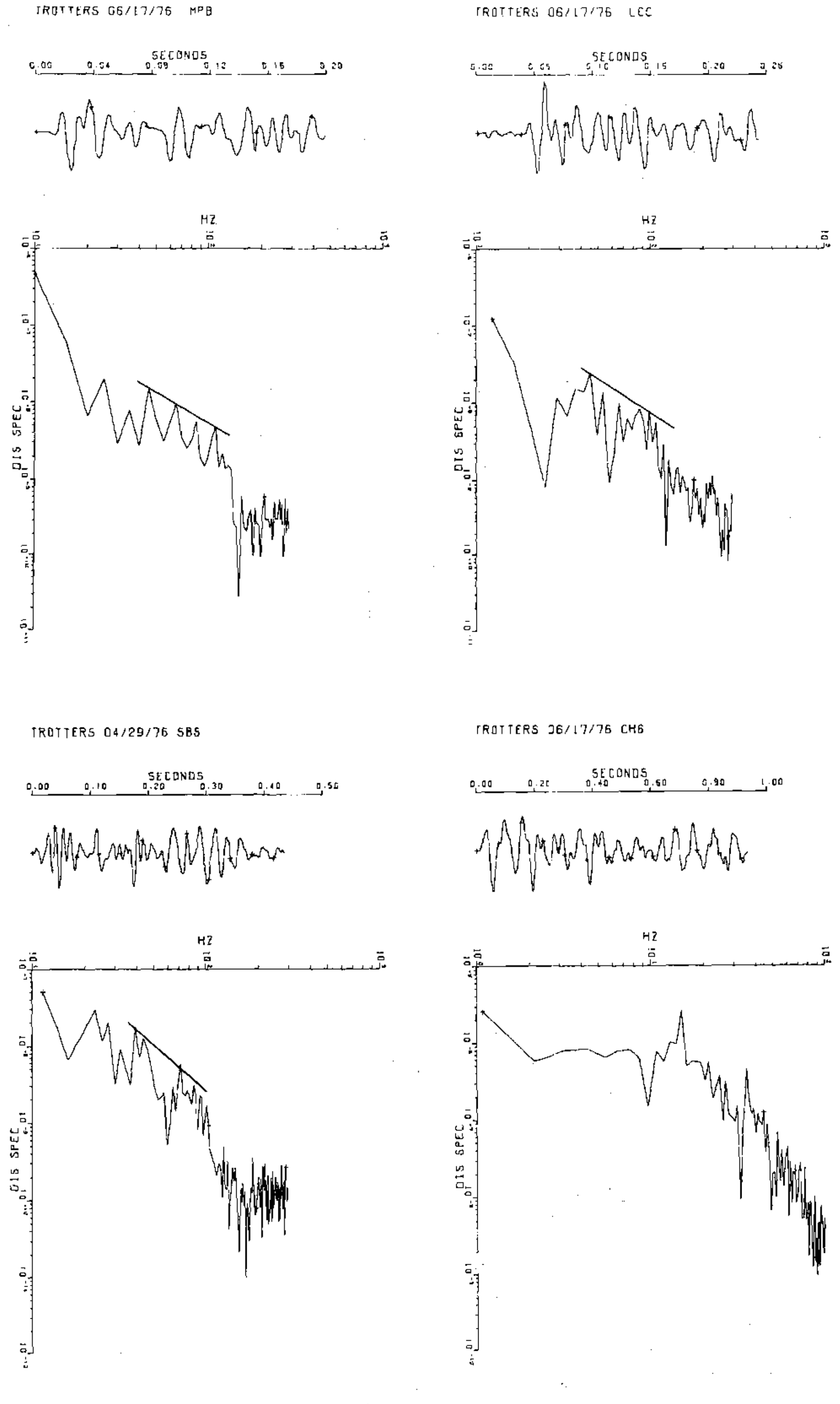

Figure 31. Spectra of Blasts (Q-value).

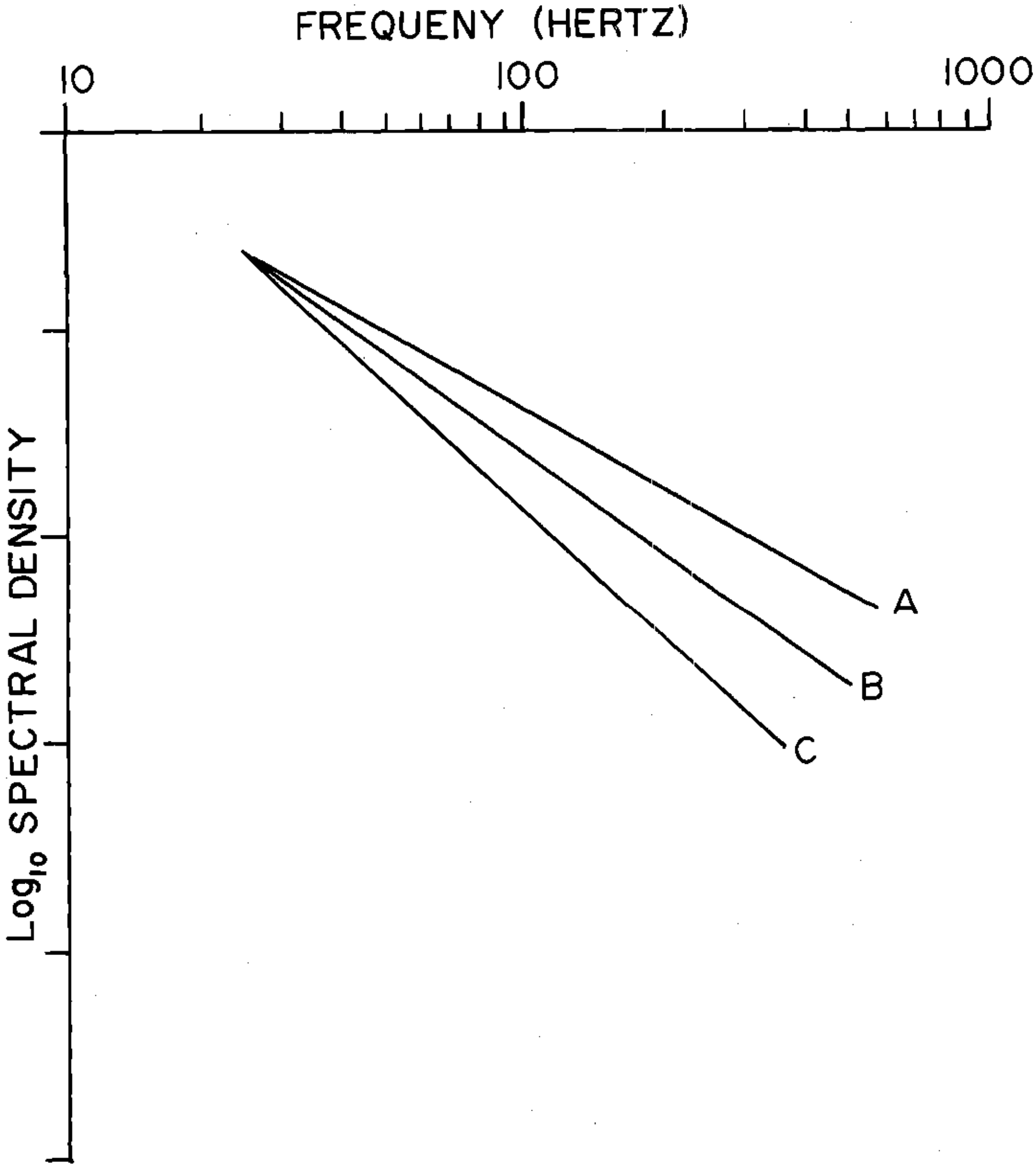

Figure 32. Comparison of Slopes for the Determination of Q-value. (Curve A is the slope of the spectrum for station MPB.) (Curve B is the slope of the spectrum for station LCC.) (Curve C is the slope of the spectrum for station SBS.)

APPENDIX E

SPECTRAL NOISE

This appendix is intended to aid in the interpretation of the spectra by pointing out possible errors. Figure 33 shows a perfectly incorrect spectrum. The trace is completely correct except for a single point that was programmed incorrectly by misplacing the decimal. The resulting dominant spike is effectively a Dirac delta function which is white noise to the spectrum. When the constant spectral amplitude of the delta function is fitted to the instrument response curve, the spectrum becomes the inverse of the response curve. Noise may also result at high frequencies if a two wide digitizing interval is used; or, at low frequencies, if these frequencies are absent from the digitized portion (Figure 34).

The curve fitted to the spectra (Figures 13-20 and Appendix G) are theoretical curves corrected for attenuation rather than best fit curves. These curves are used as a means of comparing theory to observation. The curves are fitted asymptotically because the theories are developed for an asymptotic fit and because a curve drawn through the spectra tends to obscure the data making a future re-analysis difficult. The spectral slopes and corner frequencies used for deducing properties of the earthquake are identical irregardless of whether an asymptotic fit or a best-fit through the spectra is used. The value of the seismic moment will vary; however, rarely by more than 10%. The seismic moment is used to derive only magnitude, so this variation has no effect upon this analysis. All theoretical curves are drawn assuming a complete effective stress drop.

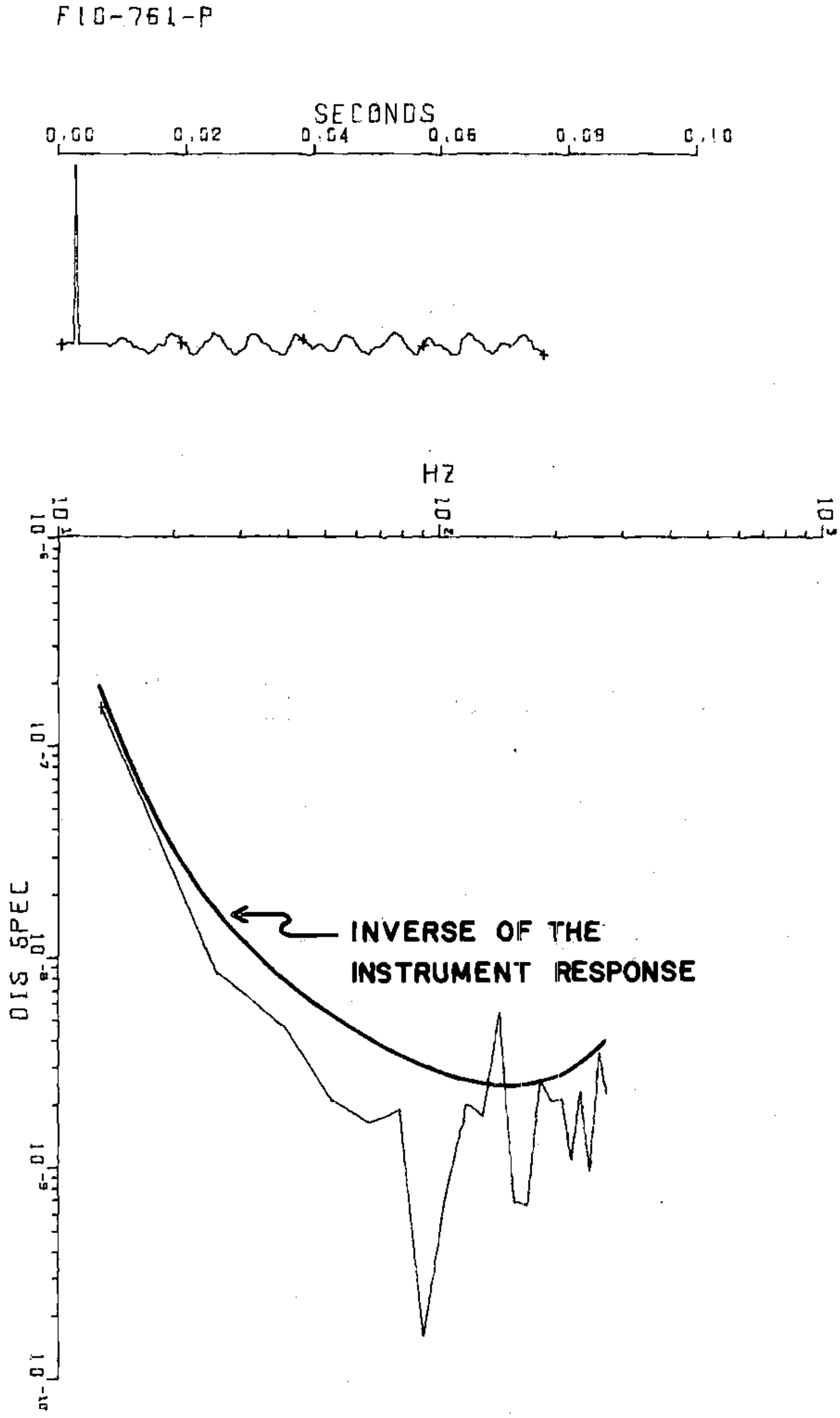

Figure 33. A Noise Spectrum.

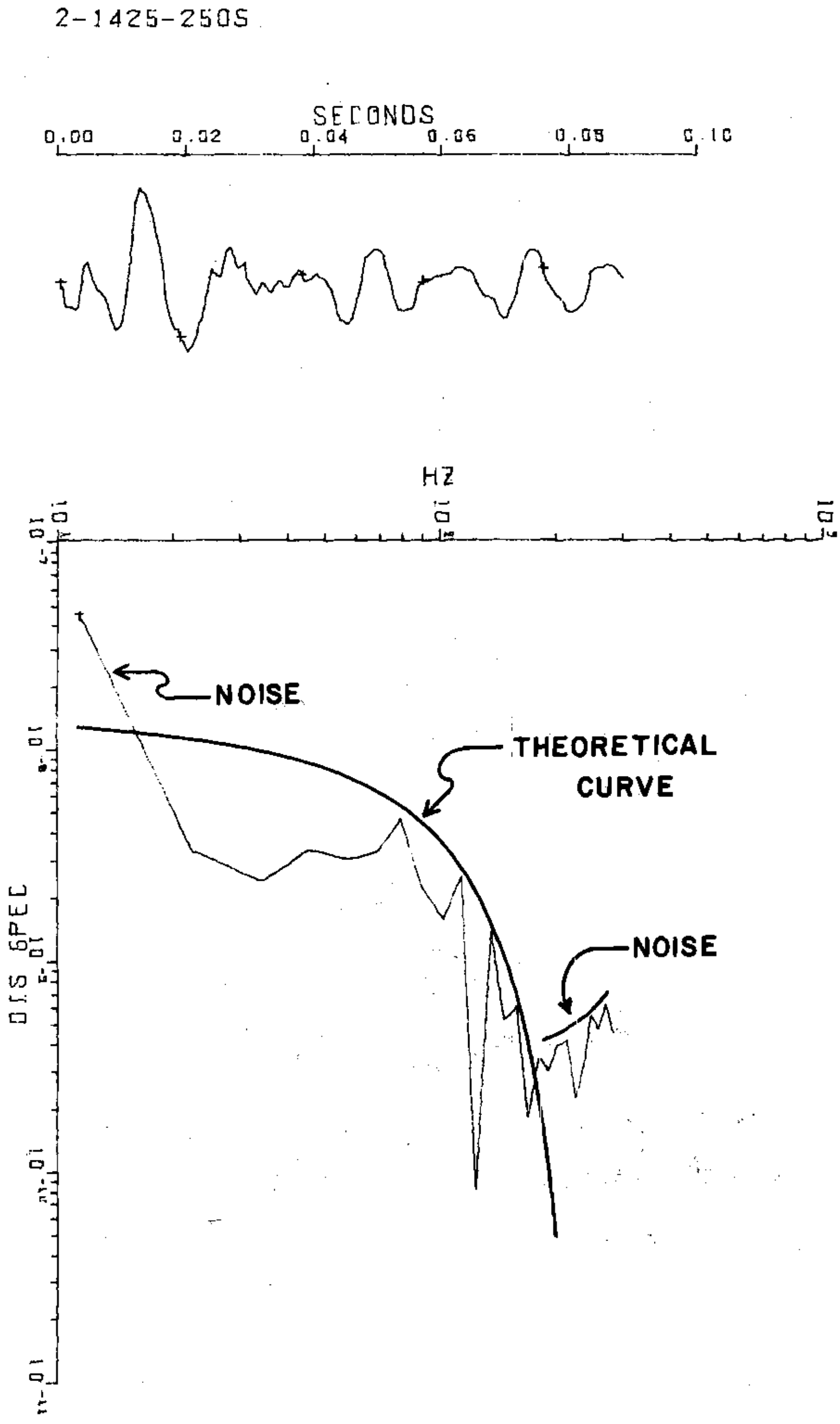

Figure 34. Noise In an Observed Spectrum.

APPENDIX F

FIELD EXPEDITIONS

This appendix is a listing of field expeditions between the dates of September 21, 1975 and September 18, 1976. Only those stations occupied by tape units are listed.

Data Region	Date	Time	Station	S-P (sec)
CHRA	09/21-22/75	No events	SUM	
JRA	11/08/75	21:18:48	PLS	0.29
		?	PLS	0.24
		02:30:+	PLS	0.28
		?	PLS	0.29
	11/09/75	08:26:08	PLS	0.20
CHRA	11/21-23/75	No events	DKF	
CHRA	12/11/75	02:13:28	HUM	0.18
	12/11/75	02:14:49	HUM	0.19
	12/11/75	03:14:05	HUM	0.19
	12/11/75	03:20:03	HUM	0.19
	12/11/75	04:13:40	HUM	0.19
	12/11/75	05:04:58	HUM	?
	12/11/75	05:12:53	HUM	0.18
	12/11/75	09:32:23	HUM	0.13
	12/11/75	11:46:44	HUM	0.19
	12/11/75	17:12:53	HUM	0.13

Data Region	Date	Time	Station	S-P (sec)
	12/11/75	25:14:21	HUM	0.13
	12/11/75	26:13:28	HUM	0.13
	12/11/75	26:19:16	HUM	0.13
	12/11/75	28:03:59	HUM	?
	12/12/75	03:12:53	HUM	0.17
CHRA	12/12/75	20:12:54	GNC	0.25
	12/12/75	20:54:53	GNC	0.07
	12/12/75	20:54:57	GNC	0.13
	12/12/75	20:55:04	GNC	0.13
	12/12/75	21:35:45	GNC	?
	12/12/75	21:37:41	GNC	0.19
	12/12/75	22:38:08	GNC	0.13
	12/12/75	22:38:08	GNC	0.16
CHRA	12/19/75	04:03:59	HUM	0.10
CHRA	12/18-20/75	19:50:27	HUM	?
	12/18-20/75	19:52:03	HUM	?
	12/18-20/75	19:52:55	HUM	0.13
	12/18-20/75	19:53:02	HUM	0.15
	12/18-20/75	19:54:57	HUM	?
	12/18-20/75	19:55:14	HUM	?
	12/18-20/75	19:55:44	HUM	0.13
	12/18-20/75	19:56:54	HUM	?
	12/18-20/75	19:57:18	HUM	?
	12/18-20/75	20:10:58	HUM	0.10
	12/18-20/75	20:16:05	HUM	0.15

Data Region	Data	Time	Station	S-P (sec)
	12/18-20/75	21:04:+	HUM	0.15
CHRA	01/09-10/76	No events		
JRA	01/15/76		DFE	0.41
	01/15/76	No events	ESD	0.29
	01/15/76	No events	SGC	0.21
CHRA	02/04/76	23:58:15	GNC	0.07
CHRA	02/05/76	00:18:23	GNC	0.08
	02/05/76	01:27:42	GNC	0.05
	02/05/76	02:04:+	GNC	0.07
	02/05/76	17:42:16	GNC	0.26
JRA	03/04/76		LBT	0.56
JRA	03/08-10/76	No events		
CHRA	03/24-25/76	No events		
CHRA	04/02/76		STA(EOC)	0.30
CHRA	04/07-09/76	Lots of extremely small events	SBS	
CHRA	06/08/76	01:33:58	DKF	0.17
		04:42:+	GNC	0.17
CHRA	09/18/76	No spectra calculated	GNC HUM DKF	

For information on the FRT events, refer to Bridges (1975).

APPENDIX G

SPECTRAL PLOTS

All of the displacement spectra calculated for this study are catalogued in this appendix. The spectra are arranged according to the ID# listed at the top of each spectrum. Spectra number one through number 14 are from the JRA, spectra number 15 through number 158 are from the CHRA, and the spectra numbers 159 through 165 are from the MTA. In addition to the P-wave and S-wave spectra, a number of surface wave spectra were calculated and are presented as numbers 166 through 174. Although surface waves are not used in this analysis, these spectra are catalogued in this appendix as a bonus prize. All spectra are calculated from the vertical component only. Theoretical curves are fitted according to the rules described in Appendix E. Each spectrum includes a reconstructed waveform of the digitized data used to calculate the spectrum. The spectra and the wave trace have been plotted using predefined axes lengths to ease the problem of fitting the diagrams neatly into a thesis. The result is that several different scales were required; thus, comparison of frequencies and slopes by eye-analysis may prove misleading. To help avoid this problem, the following symbols are used as visual aids:

0 = time t = 0 for digitizing purposes

Λ = 0.10 seconds

Δ = 100 Hertz

← = 10^{-9} mm-sec of spectral amplitude

•—< = 10^{-6} mm-sec of spectral amplitude

f_c = the corner frequency (the f_1 corner)

$\omega^{-\gamma}$ = the slope of the decay trend.

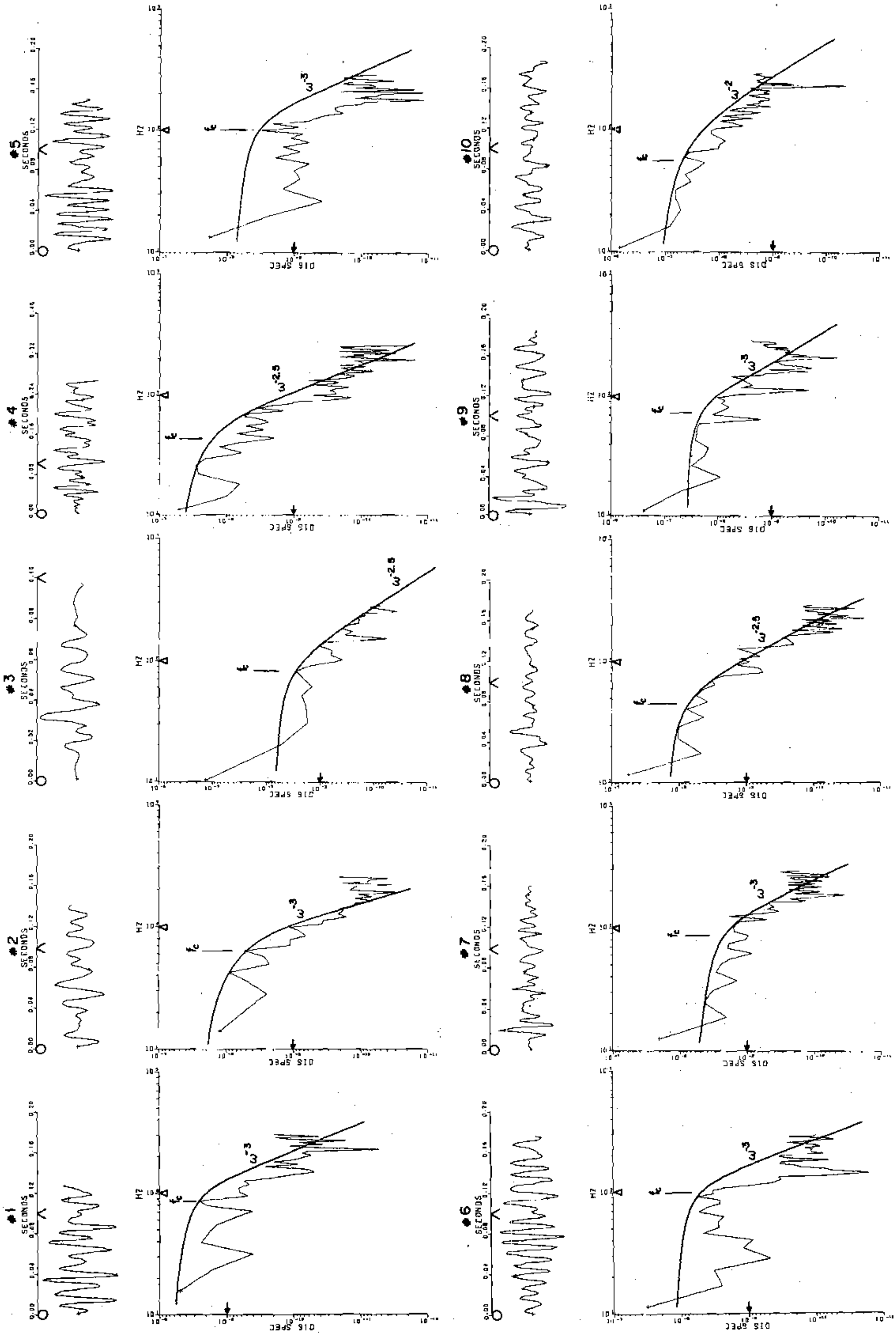

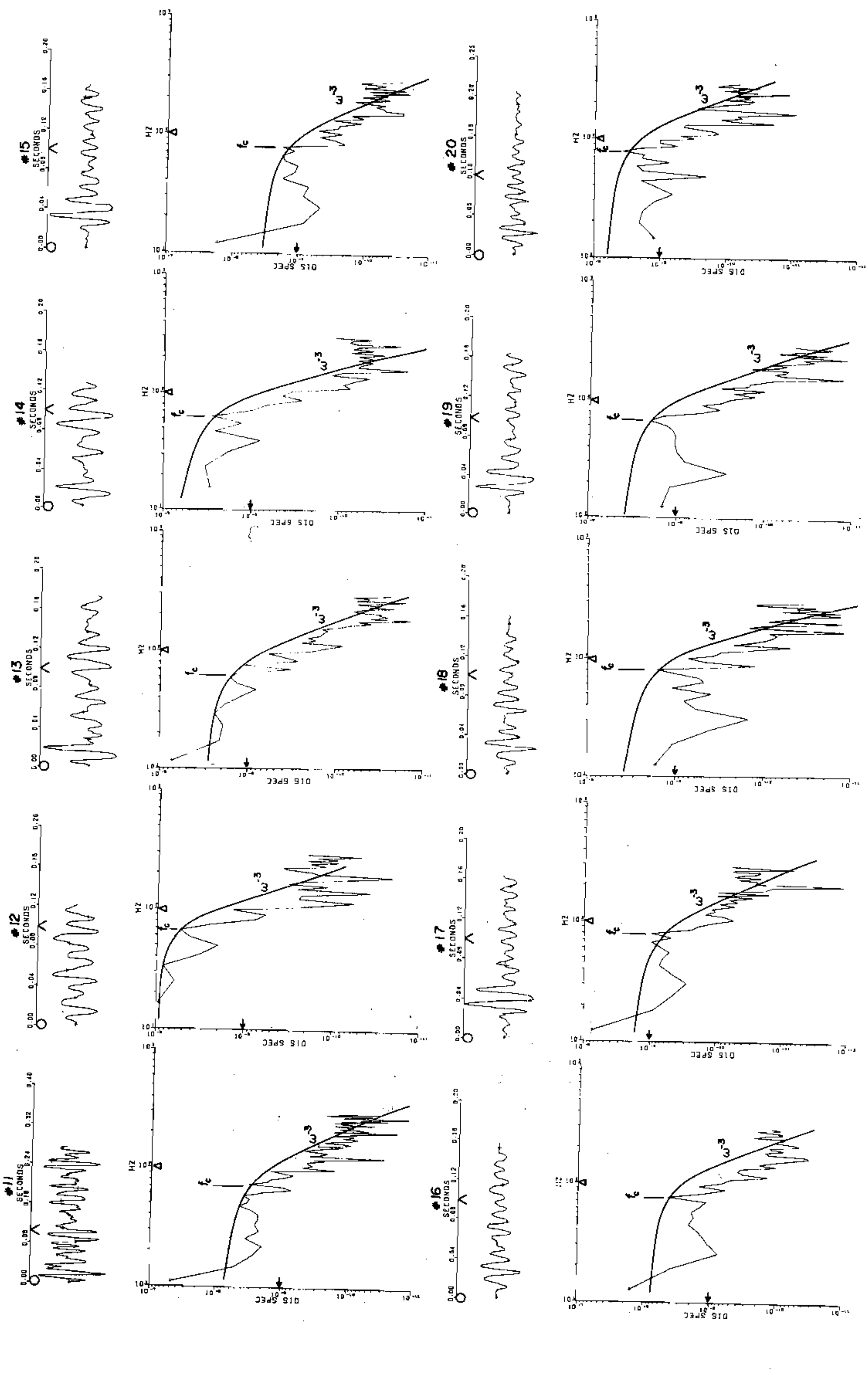
#11
#12
#13
#14
#15
#16
#17
#18
#19
#20
SECONDS
HZ
DIS SPEC
f_c
ω^{-3}

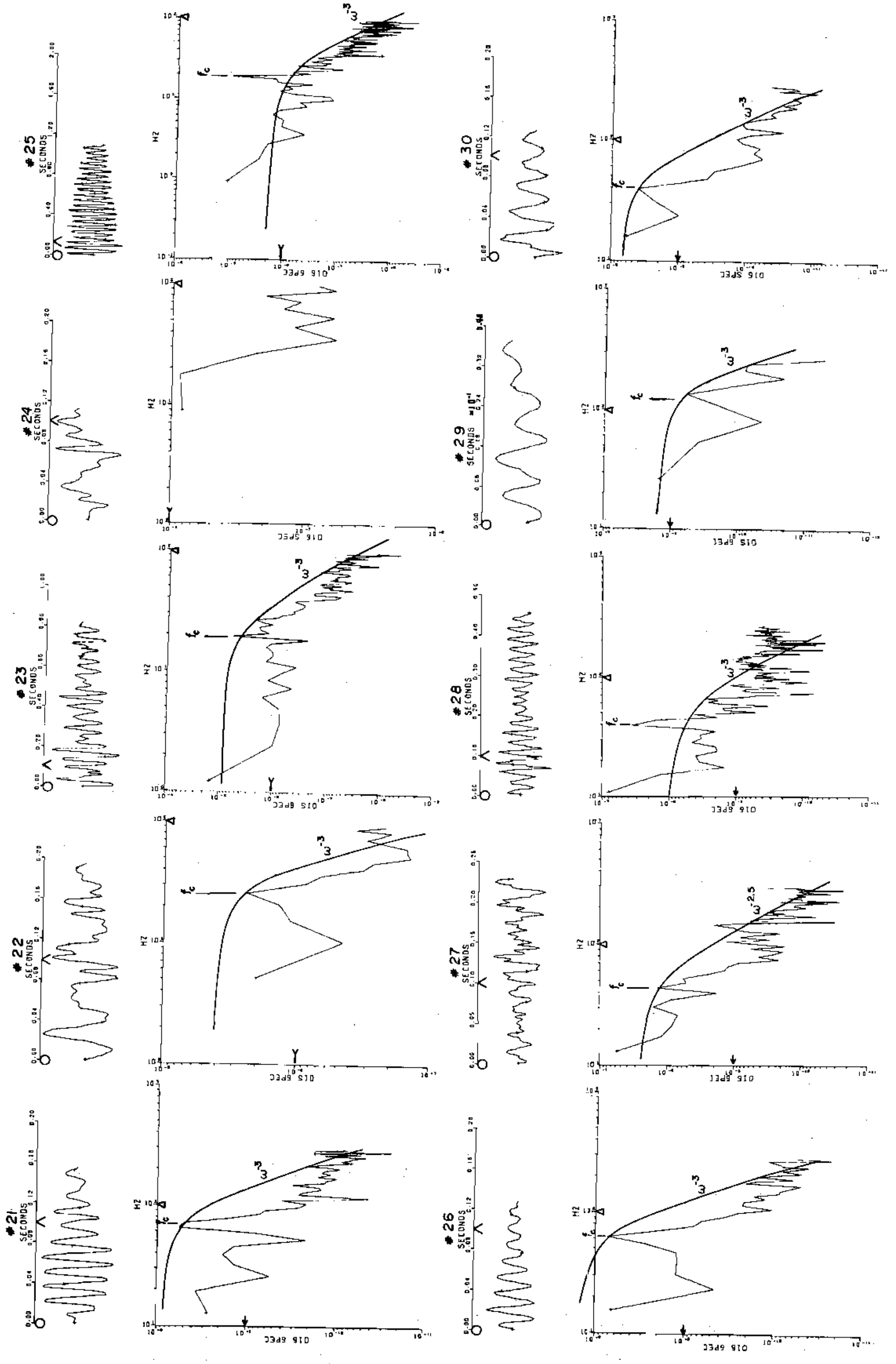

#21
#22
#23
#24
#25
#26
#27
#28
#29
#30
SECONDS
HZ
DIS SPEC
f_c
ω^-3
ω^-2.5

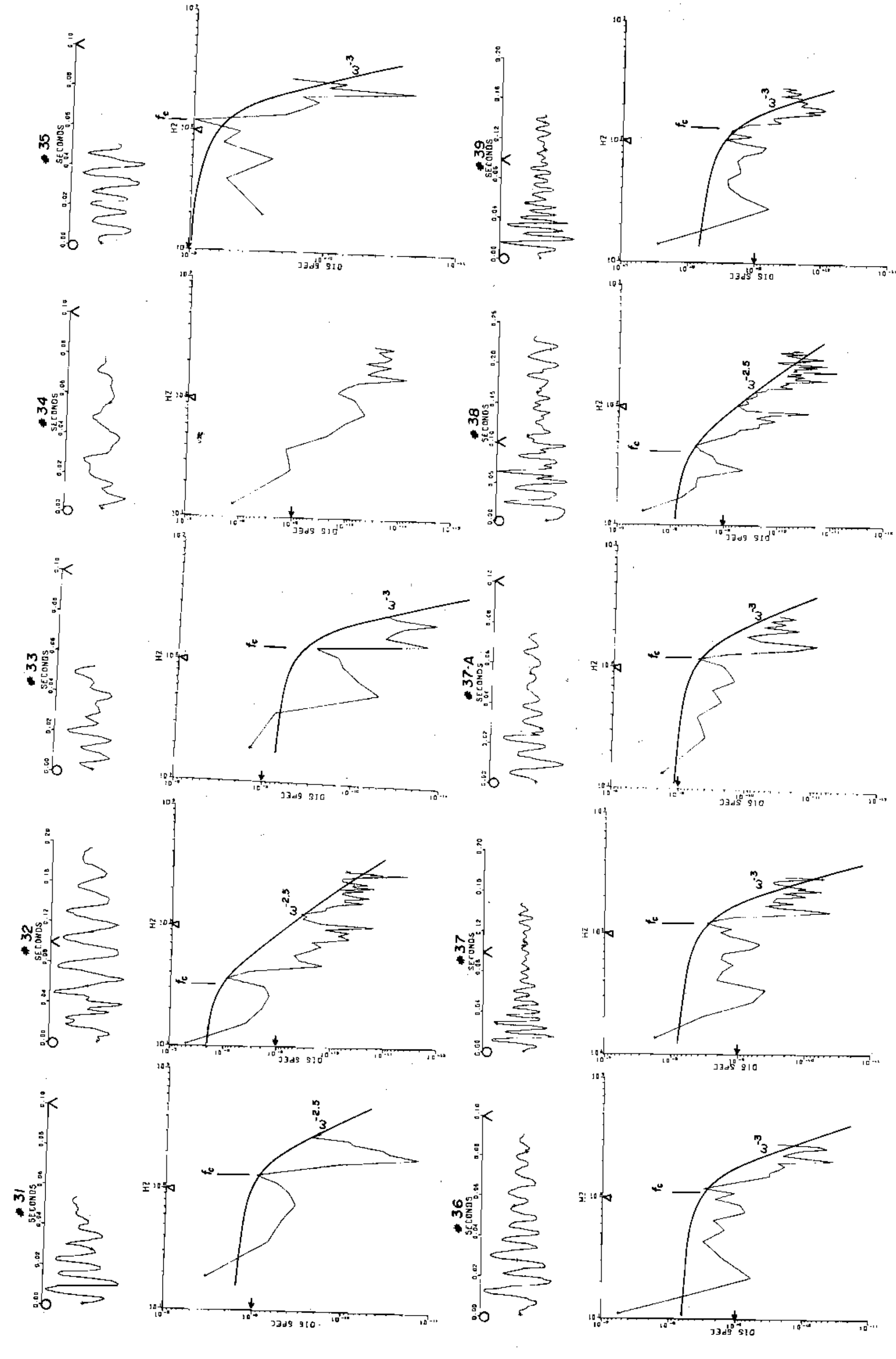
#31
#32
#33
#34
#35
#36
#37
#37-A
#38
#39
SECONDS
HZ
DIS SPEC
f_c
ω^{-3}
$\omega^{-2.5}$

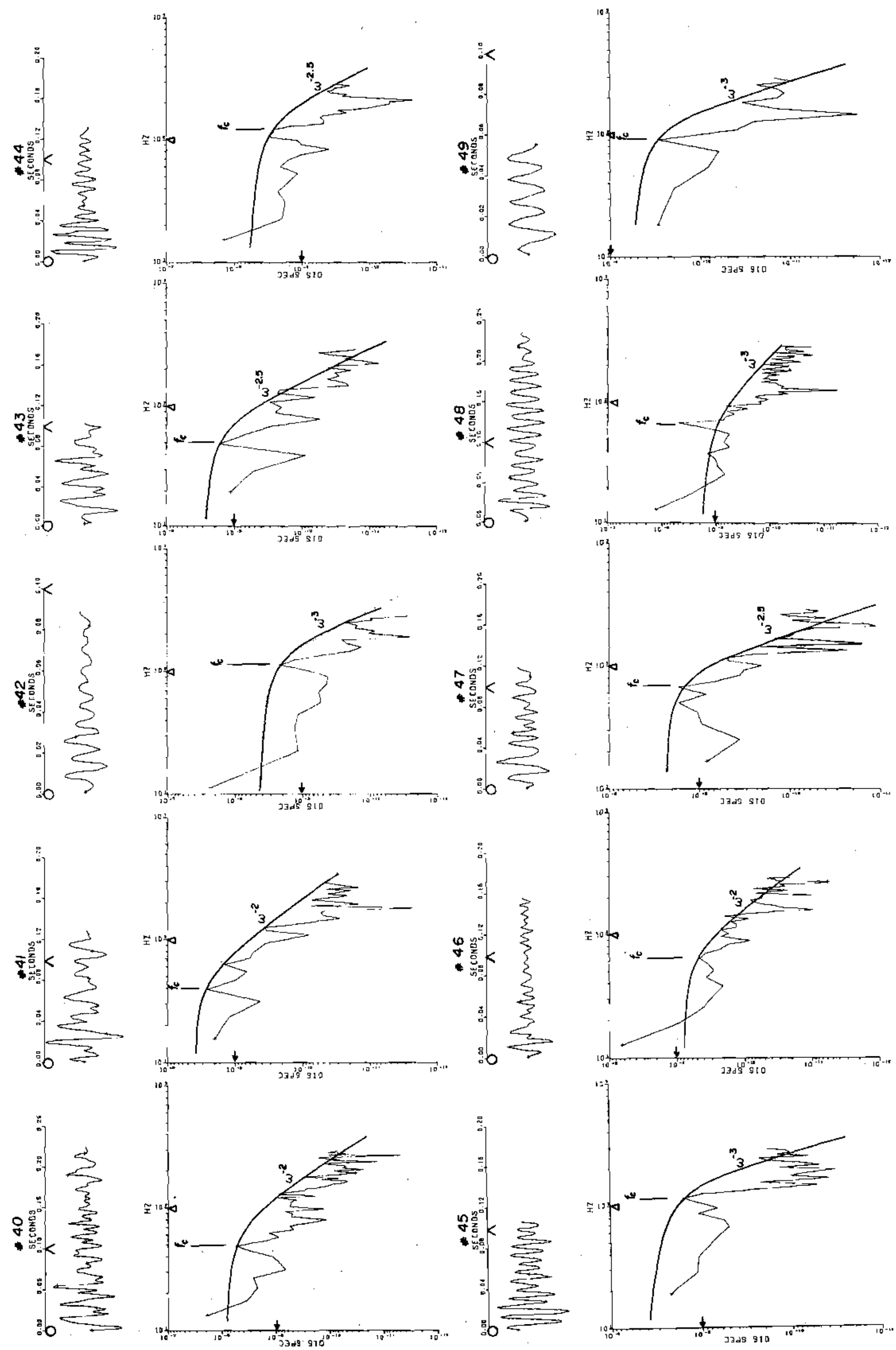

#40
#41
#42
#43
#44
#45
#46
#47
#48
#49
SECONDS
HZ
DIS SPEC
f_c
ω^{-2}
$\omega^{-2.5}$
ω^{-3}

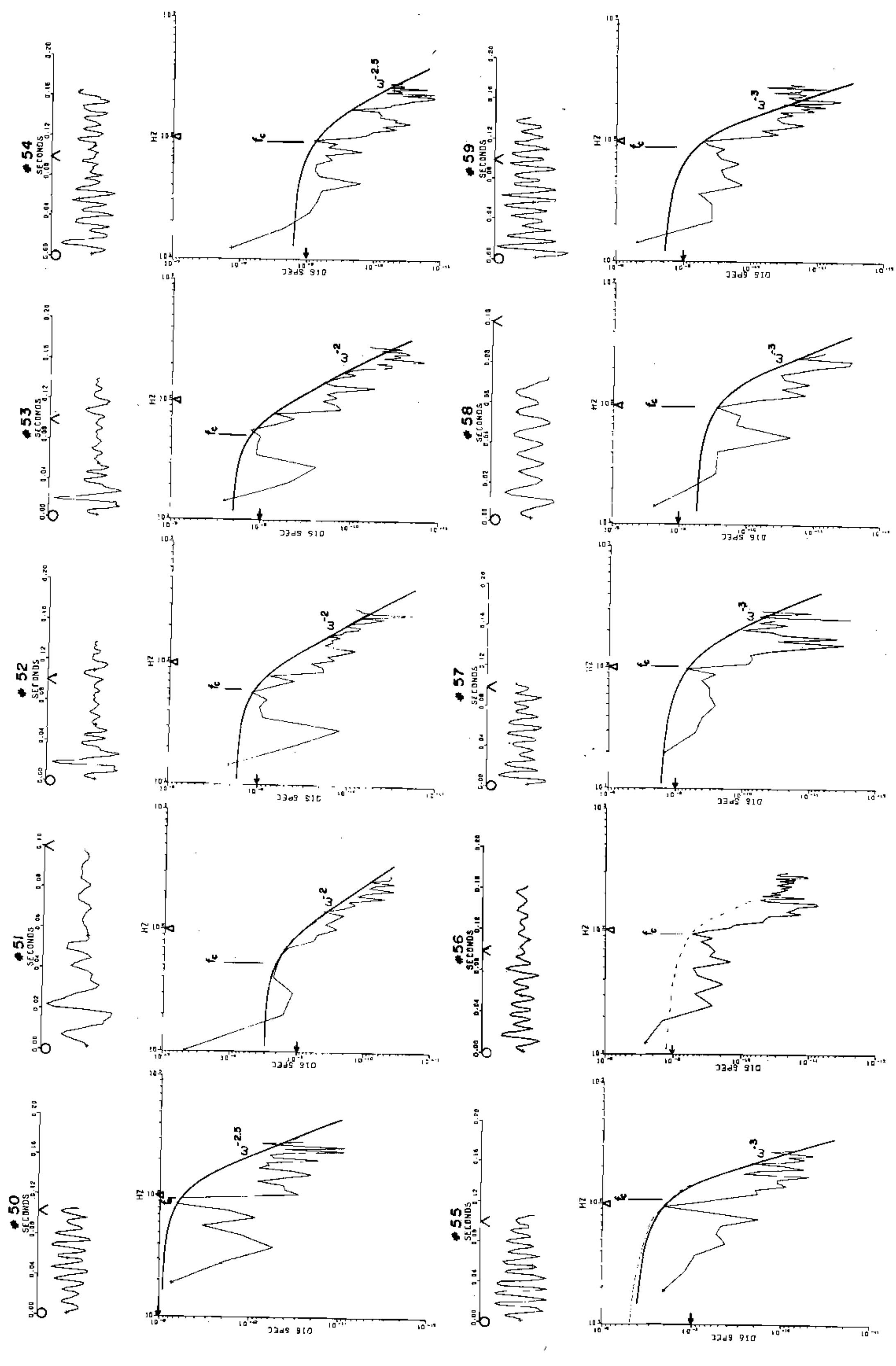
#50
#51
#52
#53
#54
#55
#56
#57
#58
#59
SECONDS
HZ
DIG SPEC
fc
ω-2.5
ω-2
ω-3

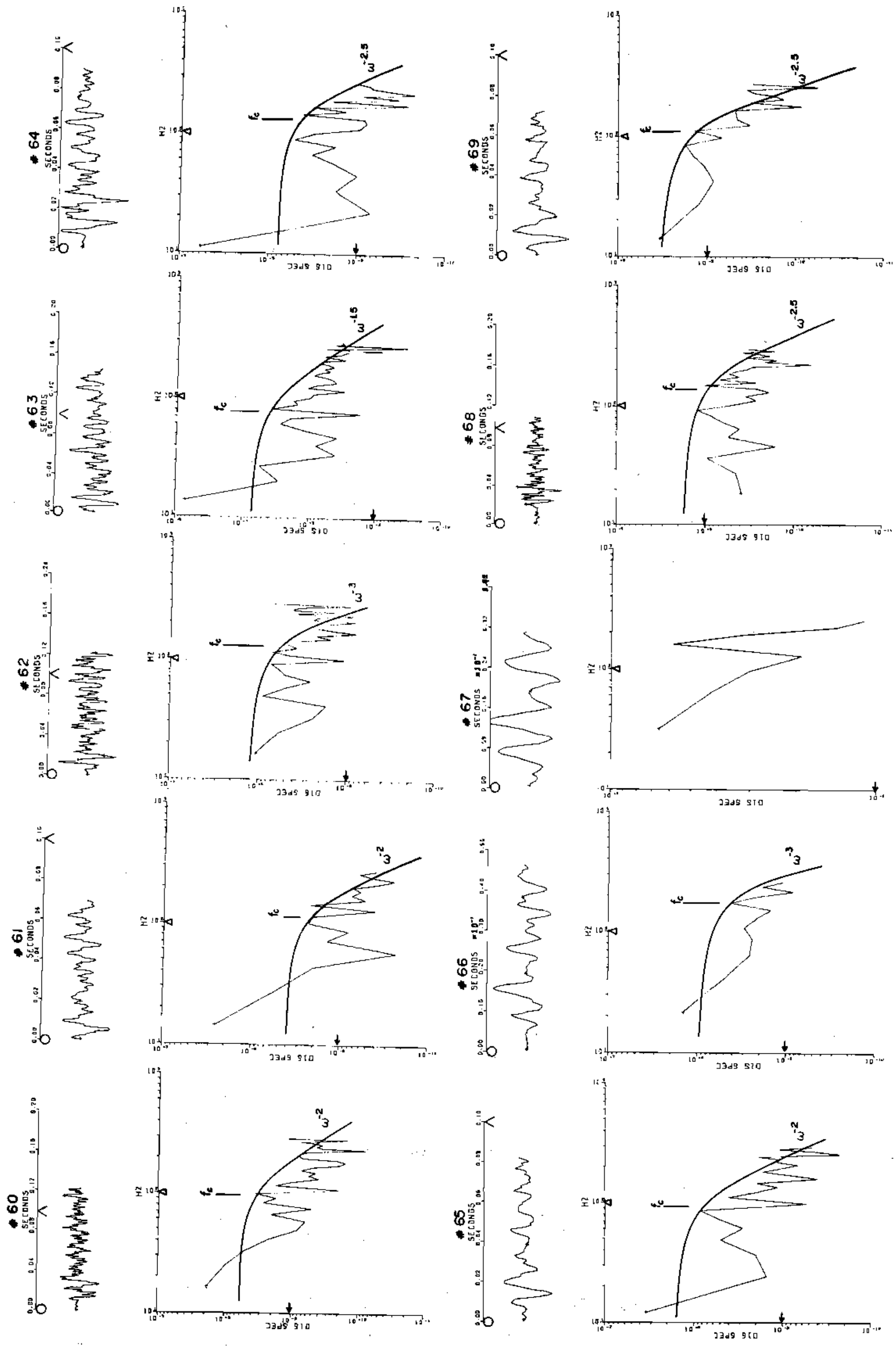

#60
#61
#62
#63
#64
#65
#66
#67
#68
#69
SECONDS
HZ
DIS SPEC

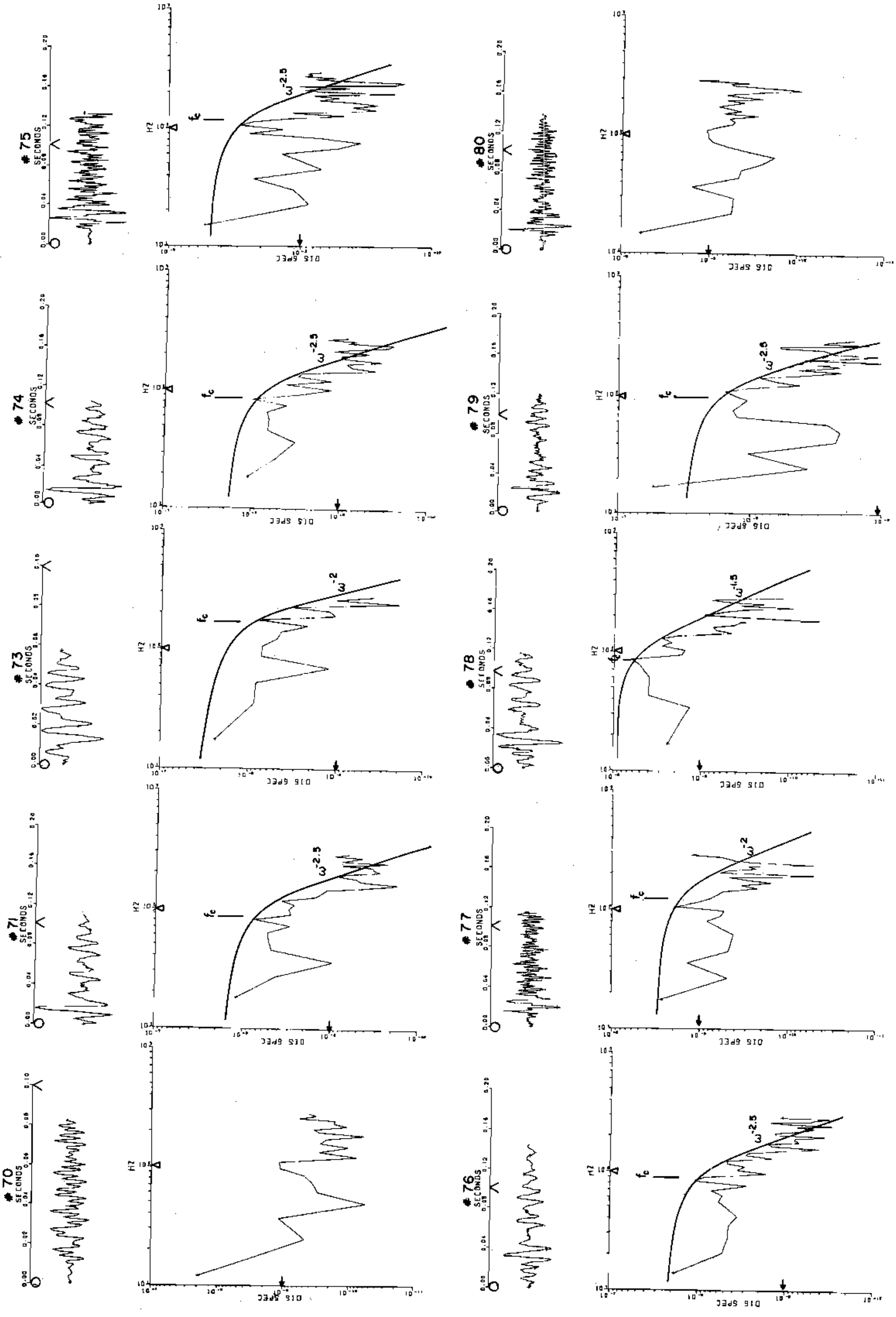
#70
#71
#73
#74
#75
#76
#77
#78
#79
#80
SECONDS
HZ
DIS SPEC
f_c
$\omega^{-2.5}$
ω^{-2}
$\omega^{-1.5}$

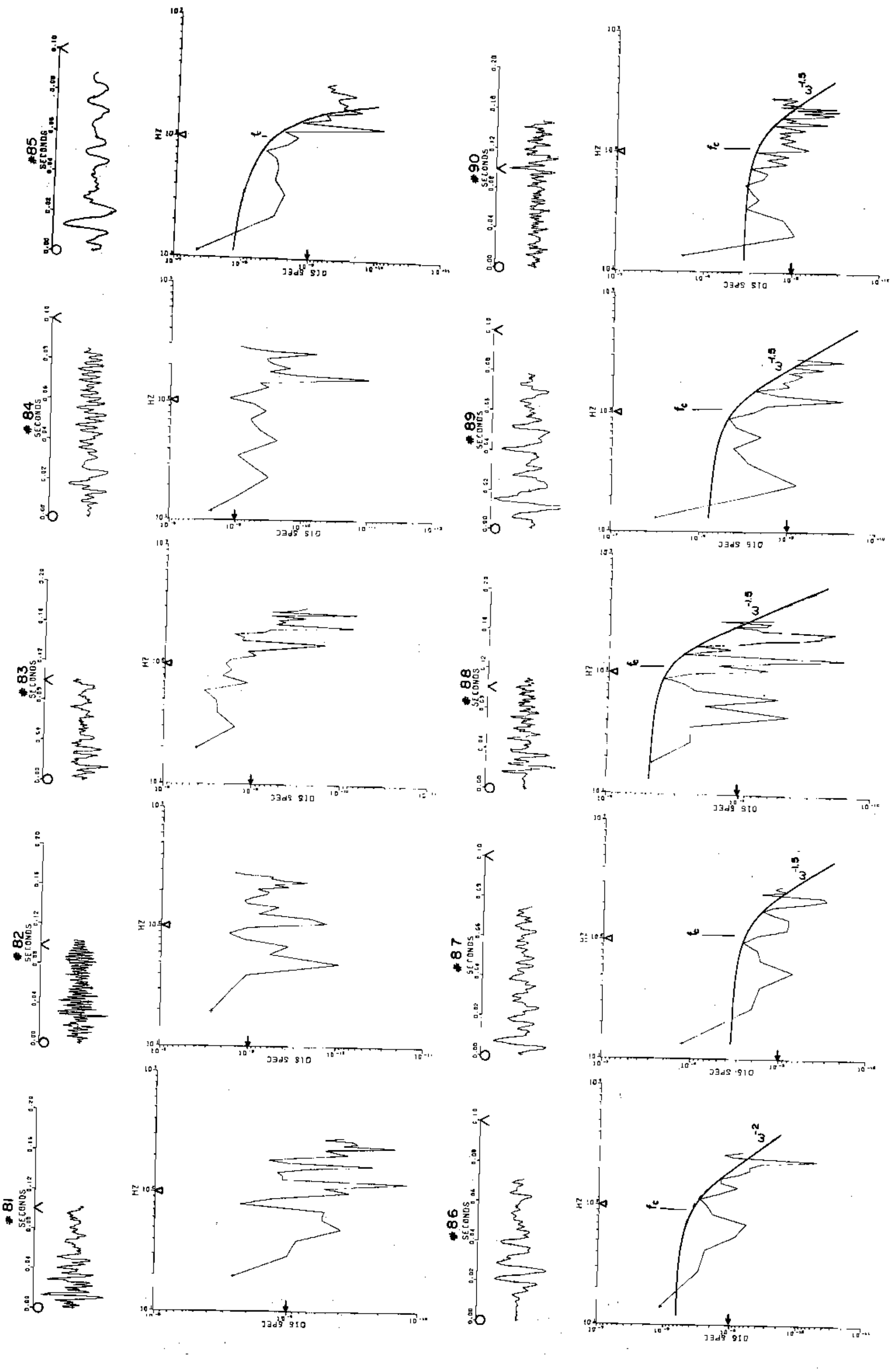
#81
#82
#83
#84
#85
#86
#87
#88
#89
#90
SECONDS
HZ
DIS SPEC

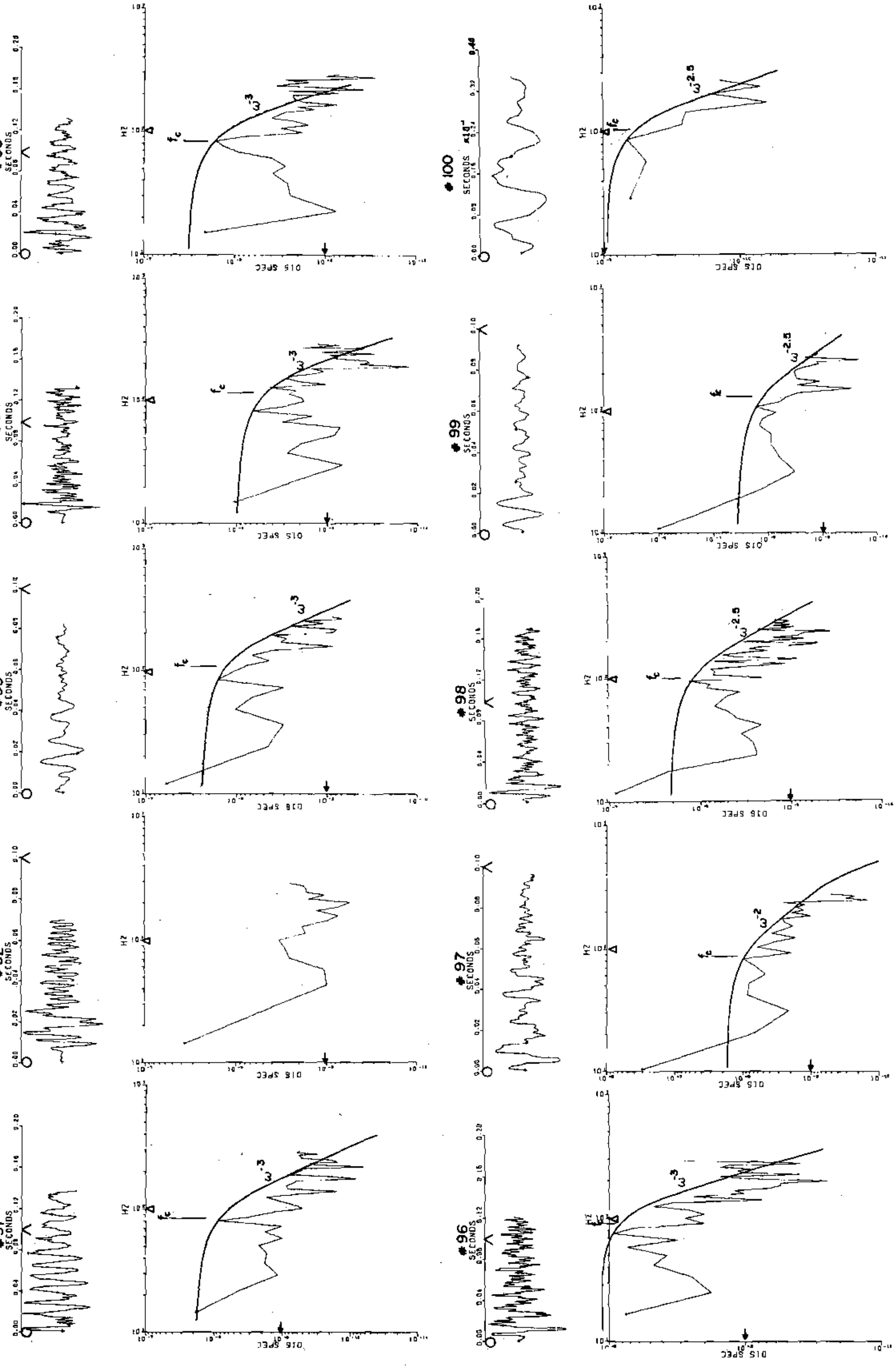
#91
#92
#93
#94
#95
#96
#97
#98
#99
#100
SECONDS
HZ
DIS SPEC

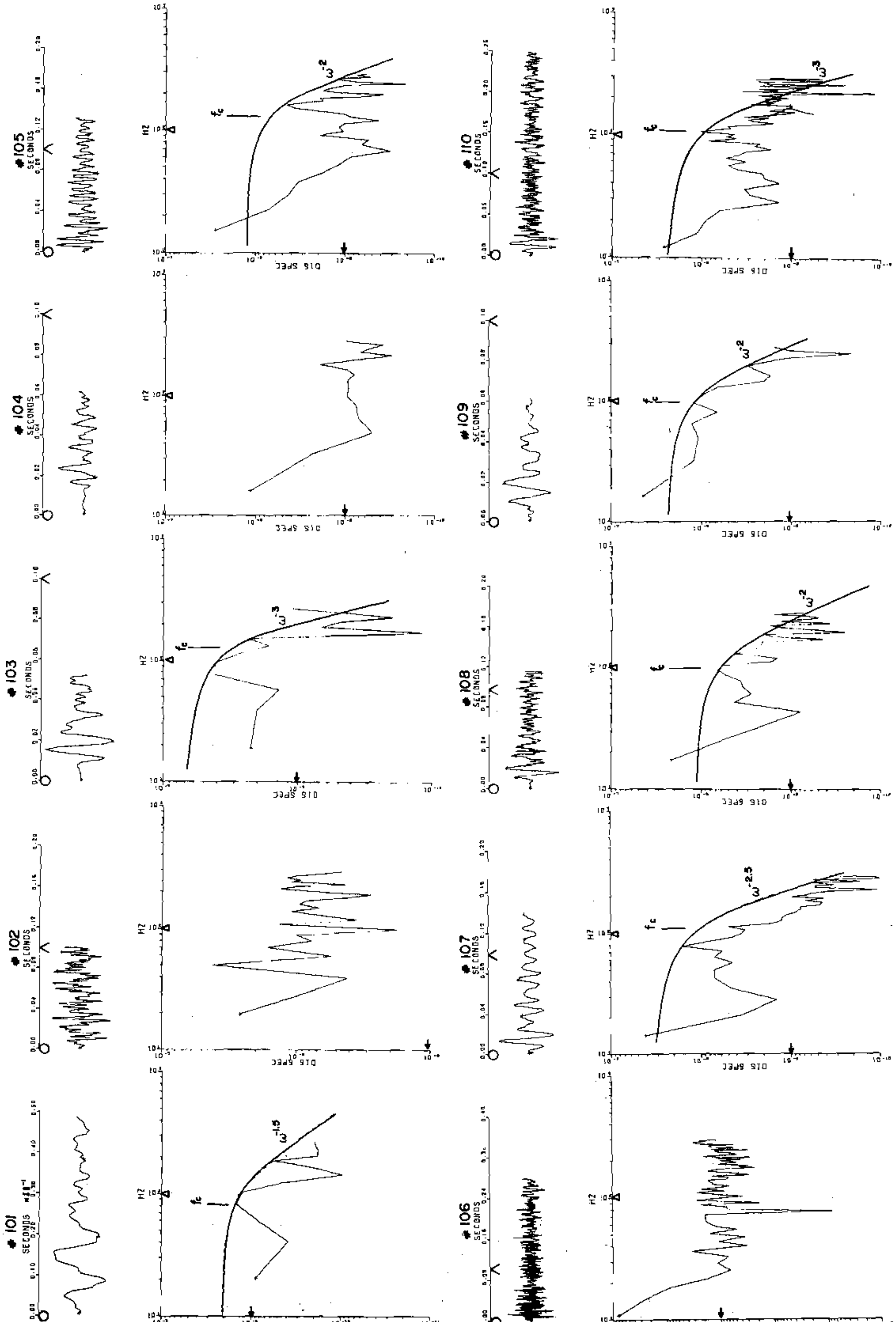

#101
SECONDS
#102
SECONDS
#103
SECONDS
#104
SECONDS
#105
SECONDS
#106
SECONDS
#107
SECONDS
#108
SECONDS
#109
SECONDS
#110
SECONDS
HZ
DIS SPEC
f_c
$\omega^{-1.5}$
ω^{-3}
ω^{-2}
$\omega^{-2.5}$

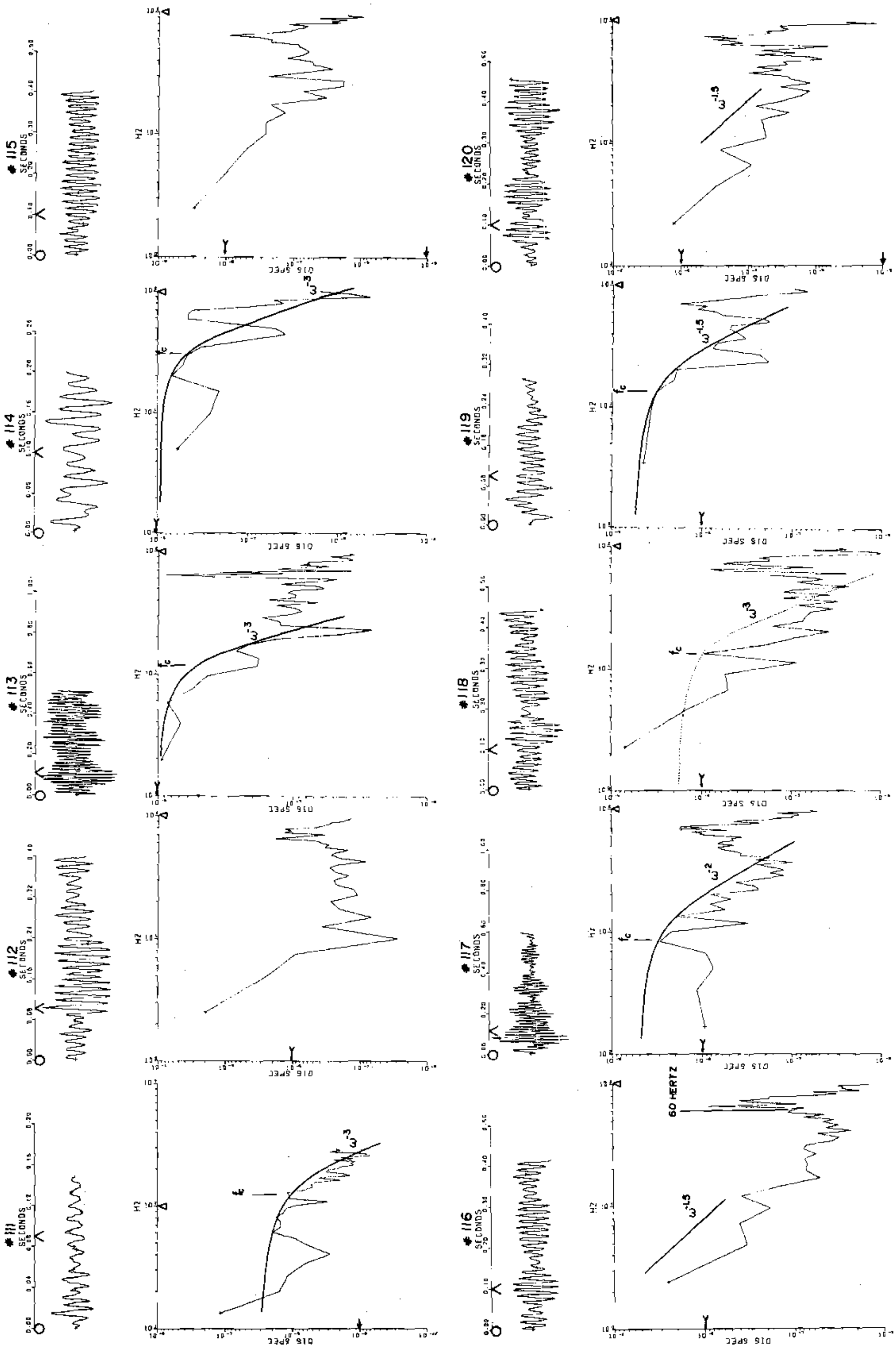

111
112
113
114
115
116
117
118
119
120
60 HERTZ

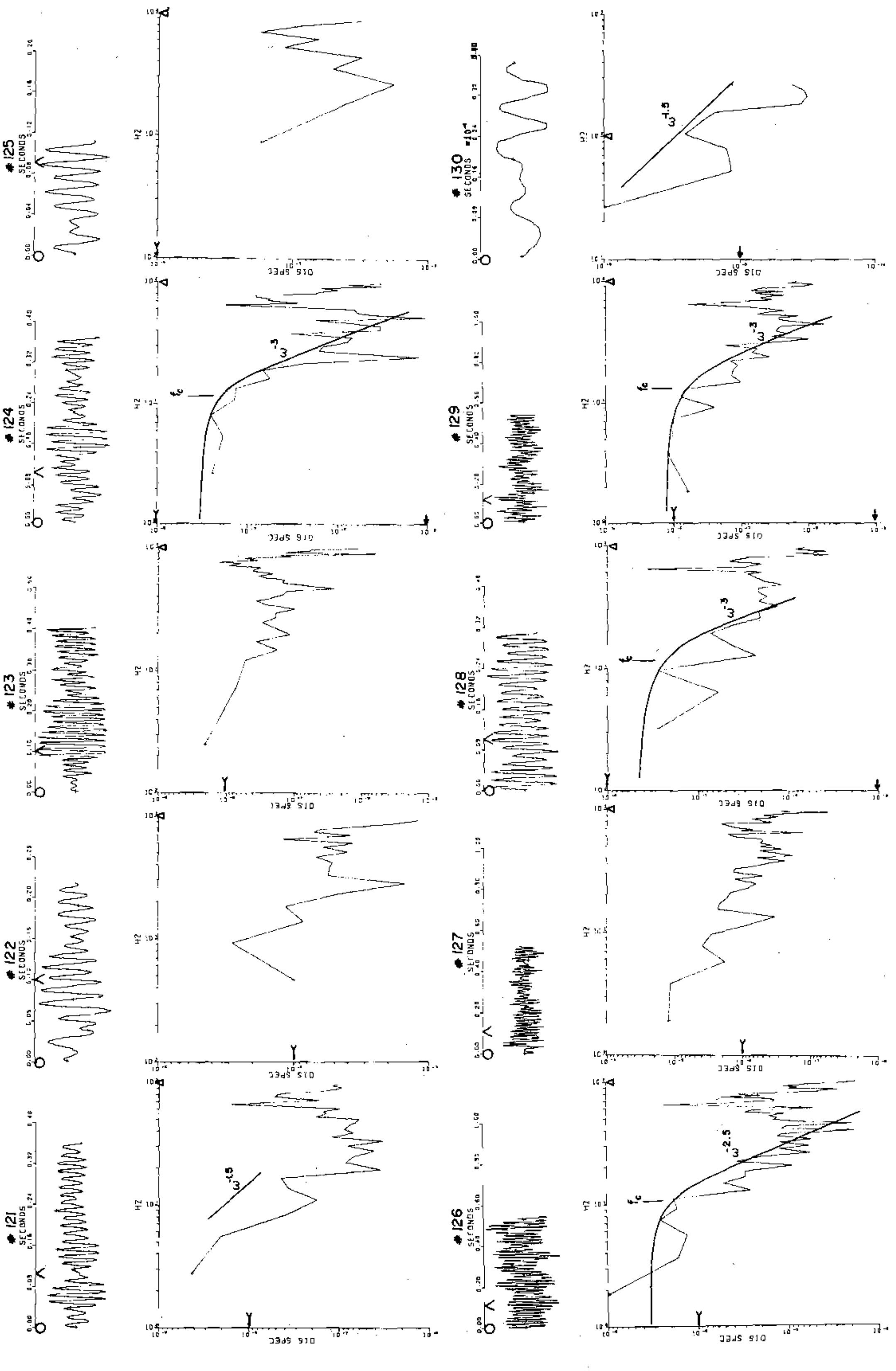

121
SECONDS
122
SECONDS
123
SECONDS
124
SECONDS
125
SECONDS
126
SECONDS
127
SECONDS
128
SECONDS
129
SECONDS
130
SECONDS
HZ
DIS SPEC
f_c
$\omega^{-1.5}$
ω^{-3}
$\omega^{-2.5}$

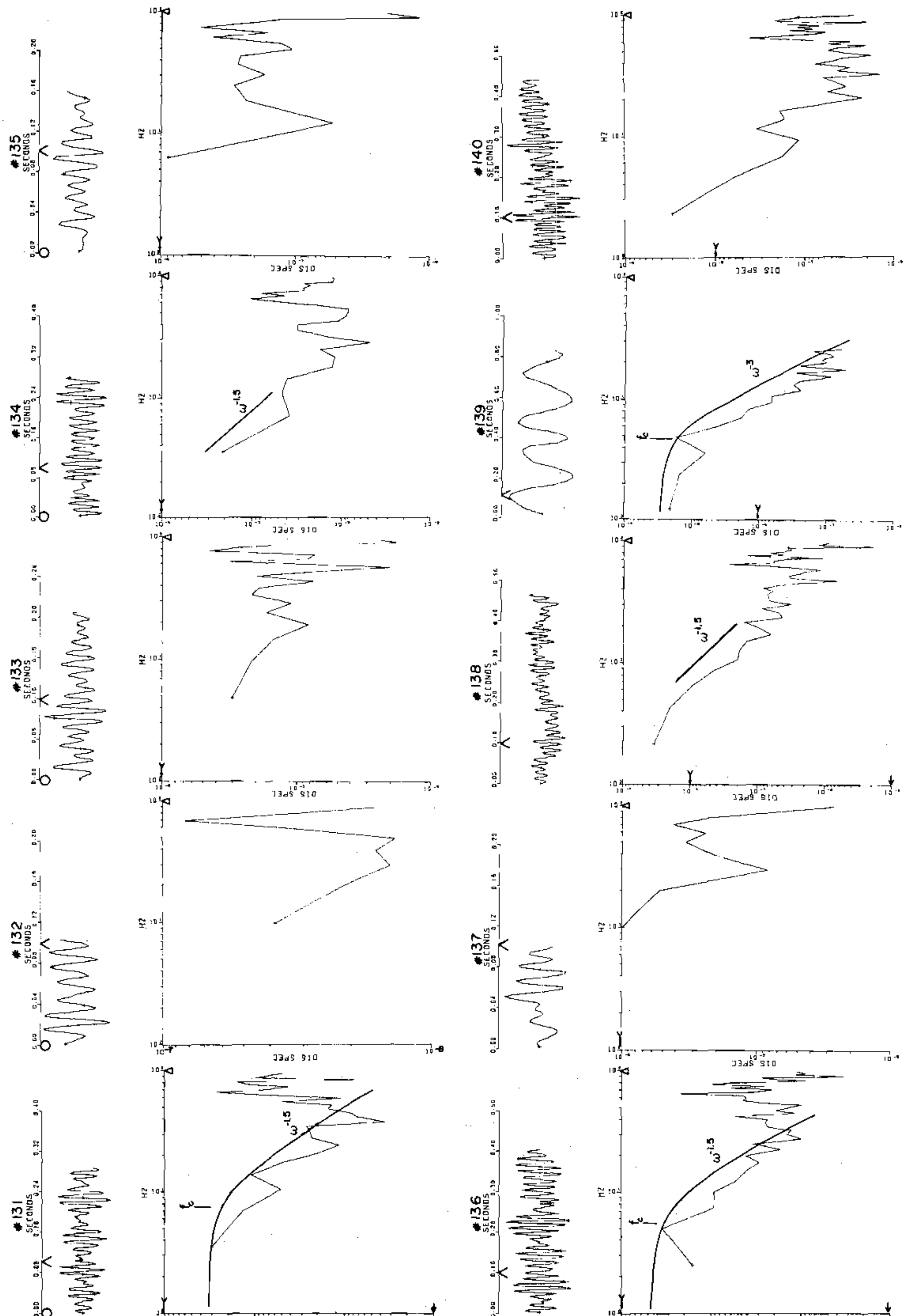
#131
SECONDS
#132
SECONDS
#133
SECONDS
#134
SECONDS
#135
SECONDS
#136
SECONDS
#137
SECONDS
#138
SECONDS
#139
SECONDS
#140
SECONDS
HZ
DIS SPEC
$\omega^{-1.5}$
f_c
$\omega^{-2.5}$
ω^{-3}

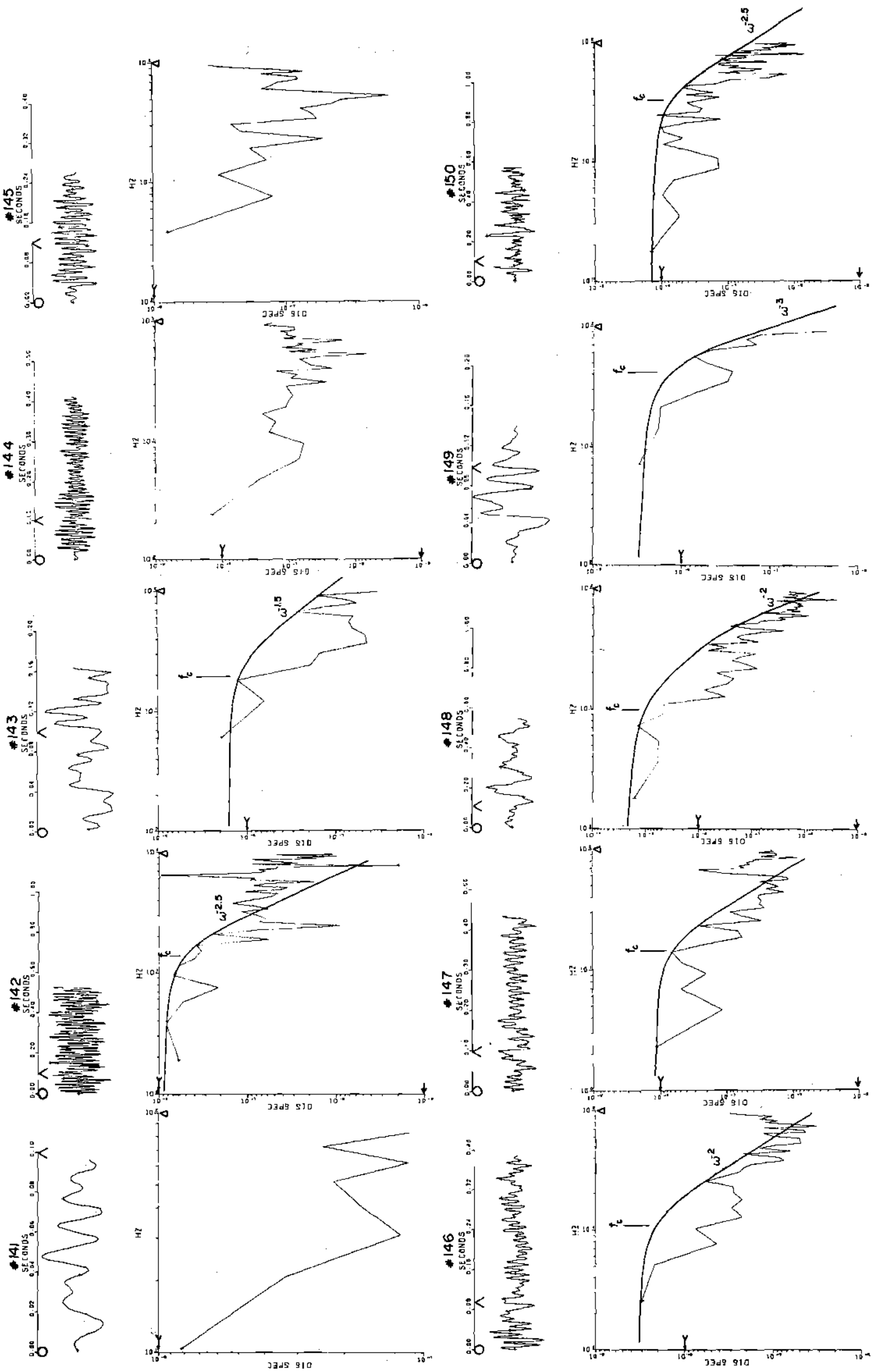

#141
SECONDS
#142
SECONDS
#143
SECONDS
#144
SECONDS
#145
SECONDS
#146
SECONDS
#147
SECONDS
#148
SECONDS
#149
SECONDS
#150
SECONDS
HZ
DIS SPEC
f_c
$\omega^{-2.5}$
$\omega^{-1.5}$
ω^{-2}
ω^{-3}

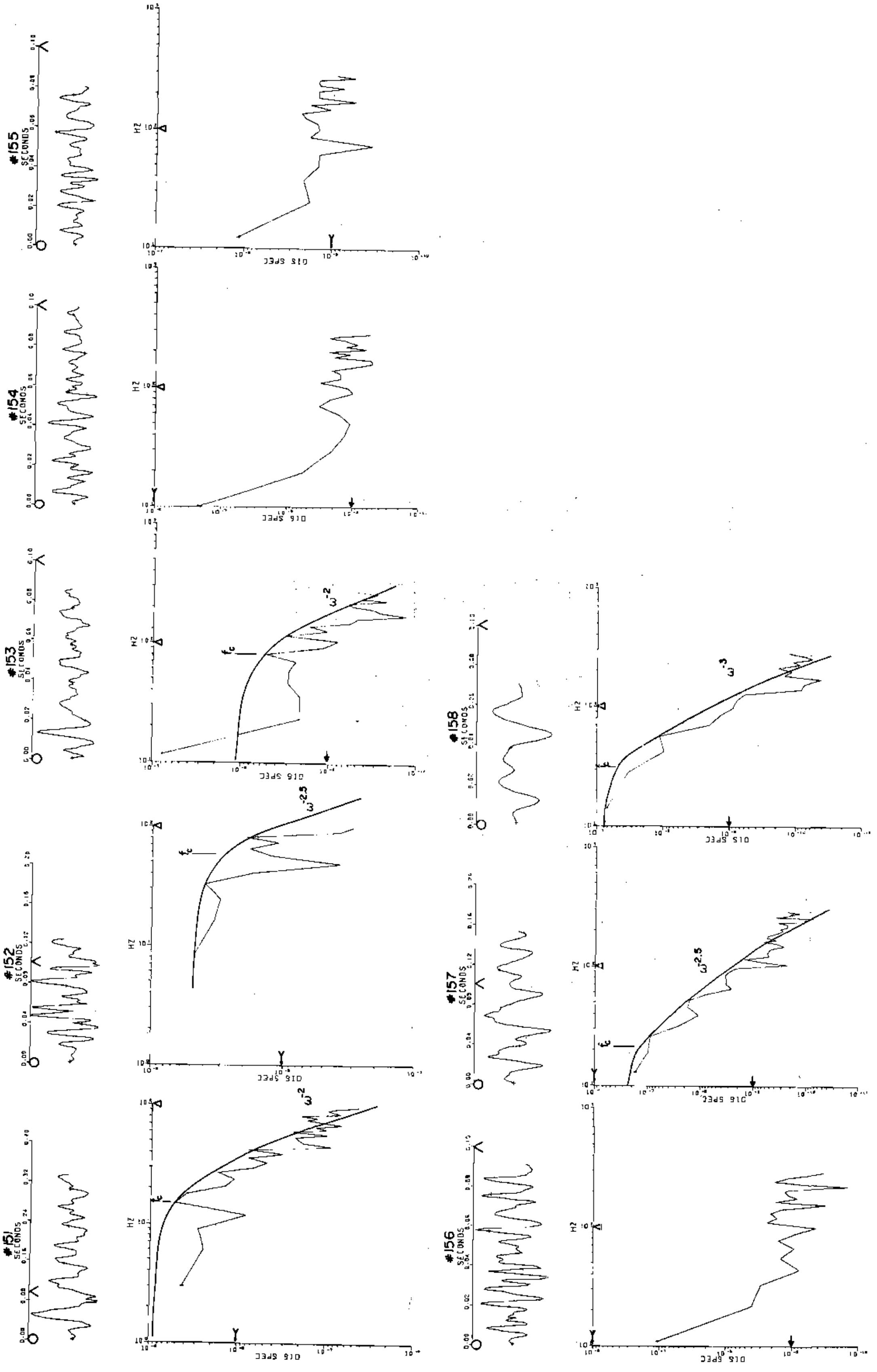
#151
SECONDS
#152
SECONDS
#153
SECONDS
#154
SECONDS
#155
SECONDS
#156
SECONDS
#157
SECONDS
#158
SECONDS
HZ
DIS SPEC
ω^{-2}
$\omega^{-2.5}$
ω^{-3}
f_c

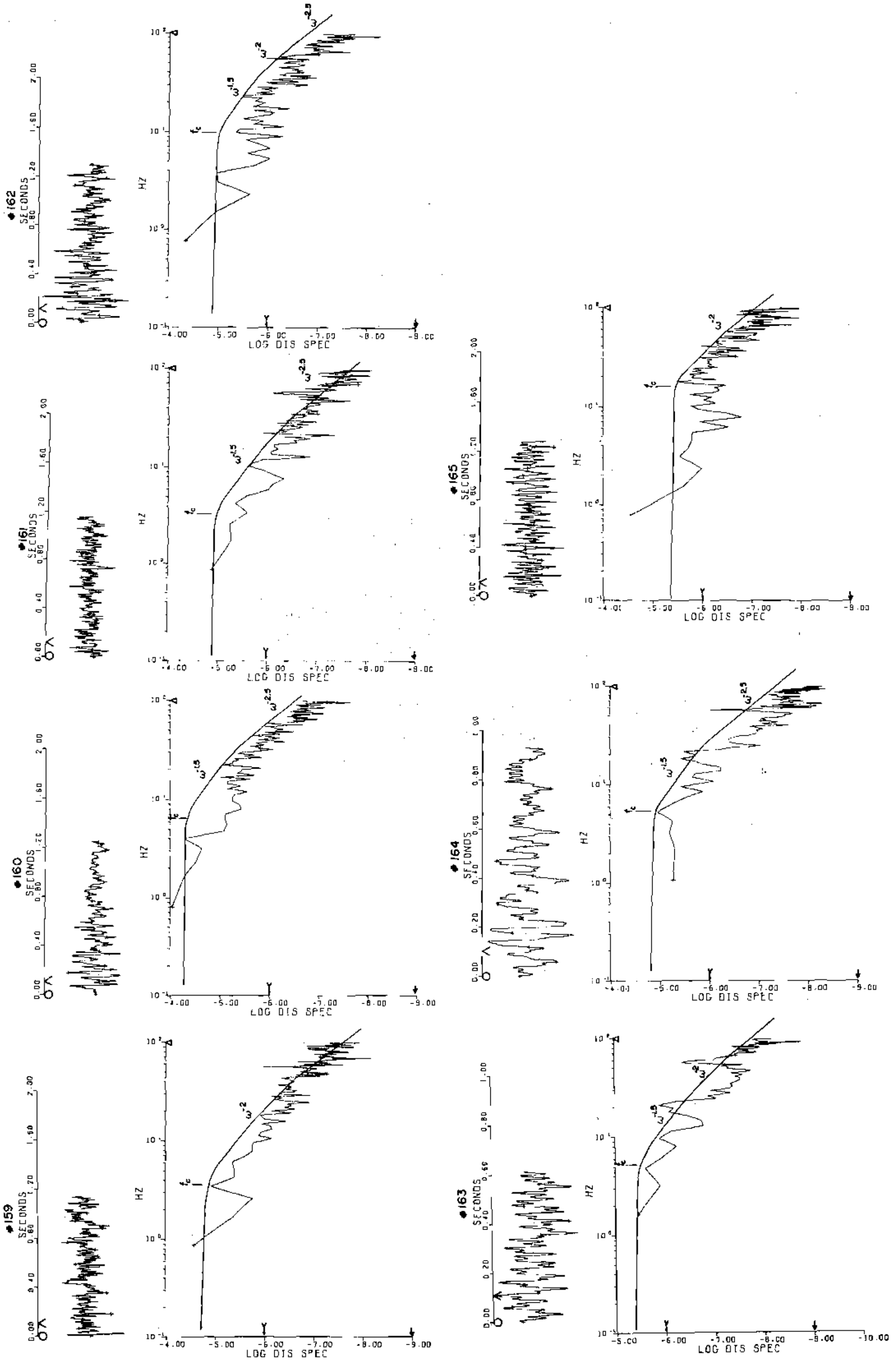
#159
#160
#161
#162
#163
#164
#165
SECONDS
HZ
LOG DIS SPEC
f_c
$\omega^{-1.5}$
ω^{-2}
$\omega^{-2.5}$

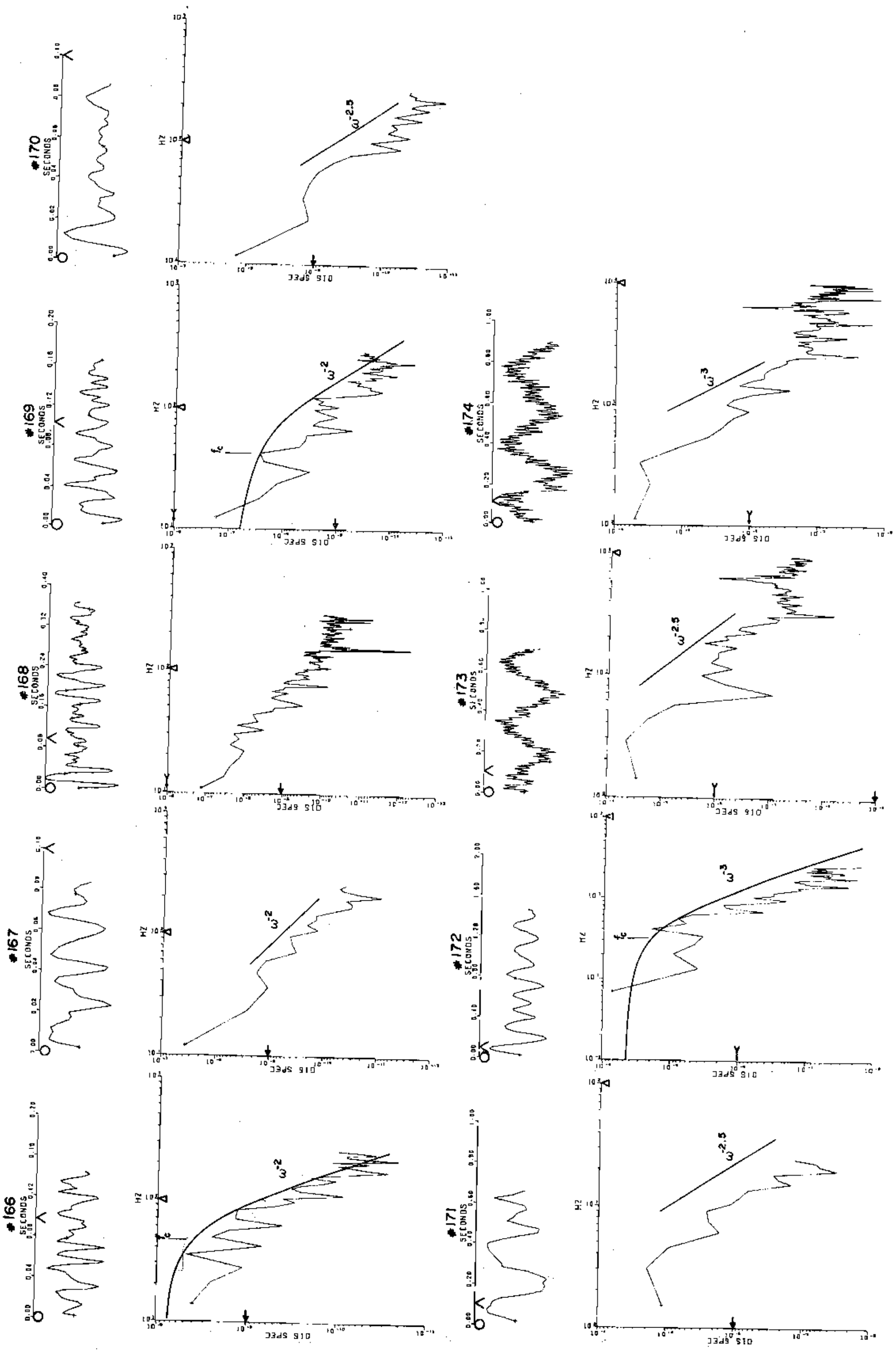
#166
SECONDS
#167
SECONDS
#168
SECONDS
#169
SECONDS
#170
SECONDS
#171
SECONDS
#172
SECONDS
#173
SECONDS
#174
SECONDS
HZ
DIS SPEC
f_c
ω^{-2}
$\omega^{-2.5}$
ω^{-3}

APPENDIX H

COMPUTER PROGRAM

The computer program, SPECT2, consists of a number of subroutines and a main driving program. A flow chart is used to explain the operation of the driving program. All subroutines are explained in the printout of the program itself; however, additional comments are presented for a select few.

Subroutine STLNFT uses the method of least squares to find a best fit line to the data. The equations can be found in many introduction calculus texts, such as Hocking (1970).

Subroutines TIC and GITTUC are used to correct spectra for instrument response. The programs are essentially a programming of response curves. GITTUC uses Figure 11. TIC uses Figure 32 which is the response of the Honeywell tape recorder system used for the MTA data and for the CHRA data at station FRT.

Subroutine SERTA is used to transform the digitized data into the frequency domain. Basically, a Fourier sine- and cosine-transformation is used (from Churchill, 1972)

$$\int_0^{\infty} F(x)\sin \omega x \, dx = \mathrm{Imag}\ (F(\omega)) \tag{65}$$

$$\int_0^{\infty} F(x)\cos \omega x \, dx = \mathrm{Real}\ (F(\omega)) \tag{66}$$

The phase is found by examining the phase angle between the sine and cosine transformations.

$$\phi = \mathrm{ATAN}\ (\mathrm{Real}/\mathrm{Imag}) \tag{67}$$

The spectral amplitude is given by

$$\text{Spec. Amp.} = (R^2 + I^2)^{1/2} \tag{68}$$

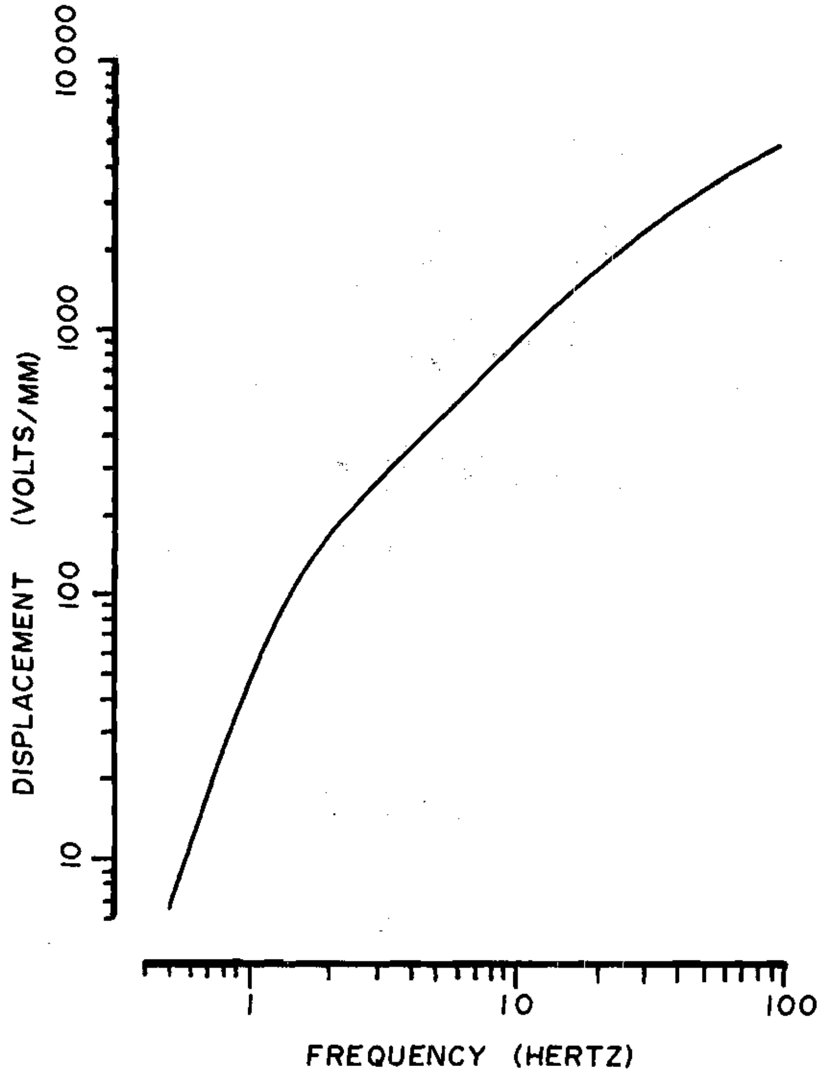

Figure 35. Displacement Response of TIC.

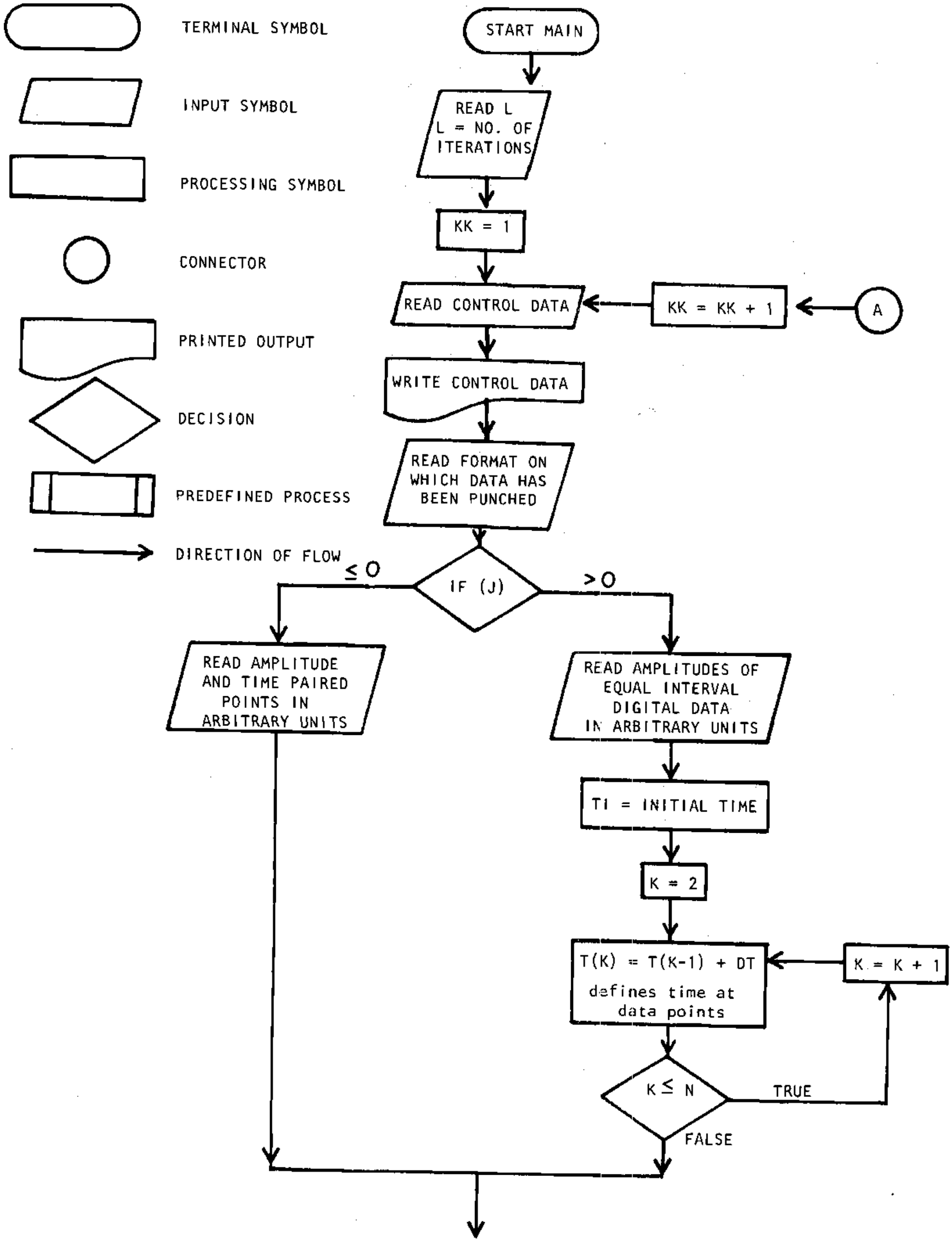
TERMINAL SYMBOL
INPUT SYMBOL
PROCESSING SYMBOL
CONNECTOR
PRINTED OUTPUT
DECISION
PREDEFINED PROCESS
DIRECTION OF FLOW
START MAIN
READ L
L = NO. OF ITERATIONS
KK = 1
READ CONTROL DATA
KK = KK + 1
A
WRITE CONTROL DATA
READ FORMAT ON WHICH DATA HAS BEEN PUNCHED
IF (J)
≤ 0
> 0
READ AMPLITUDE AND TIME PAIRED POINTS IN ARBITRARY UNITS
READ AMPLITUDES OF EQUAL INTERVAL DIGITAL DATA IN ARBITRARY UNITS
TI = INITIAL TIME
K = 2
T(K) = T(K-1) + DT
defines time at data points
K = K + 1
K ≤ N
TRUE
FALSE

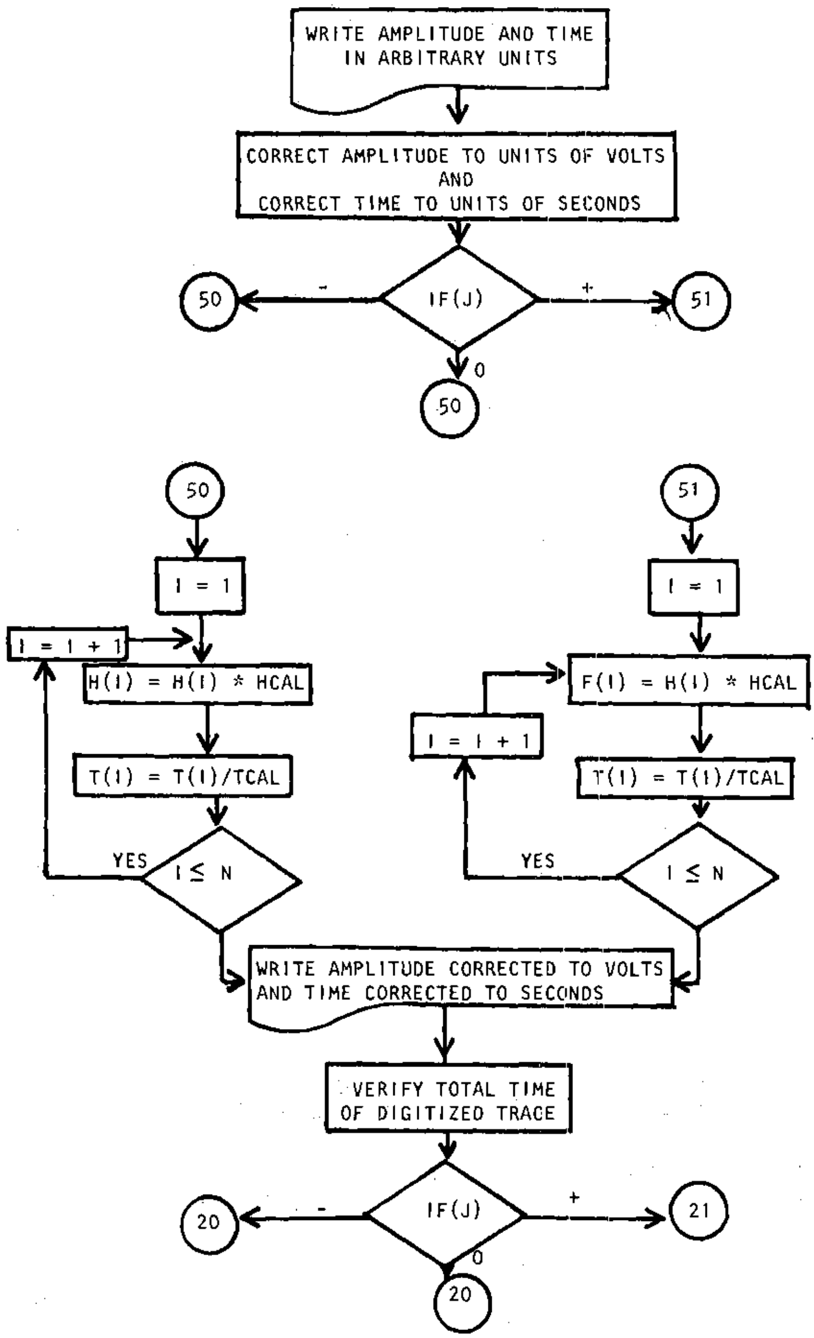

WRITE AMPLITUDE AND TIME IN ARBITRARY UNITS
CORRECT AMPLITUDE TO UNITS OF VOLTS AND CORRECT TIME TO UNITS OF SECONDS
IF(J)
-
+
0
50
51
50
50
51
I = 1
I = 1
I = I + 1
H(I) = H(I) * HCAL
F(I) = H(I) * HCAL
I = I + 1
T(I) = T(I)/TCAL
T(I) = T(I)/TCAL
YES
I ≤ N
YES
I ≤ N
WRITE AMPLITUDE CORRECTED TO VOLTS AND TIME CORRECTED TO SECONDS
VERIFY TOTAL TIME OF DIGITIZED TRACE
IF(J)
-
+
0
20
21
20

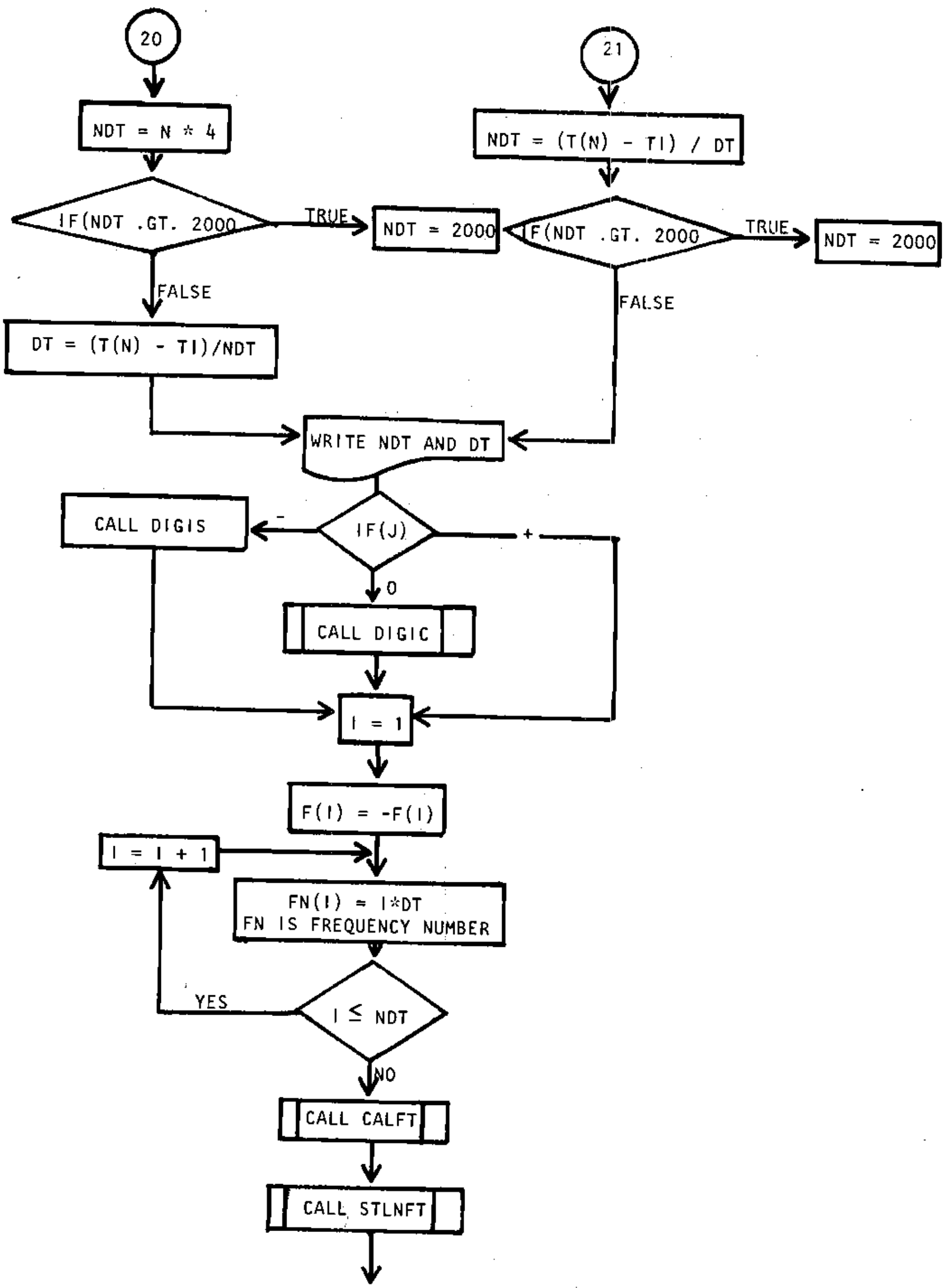
20
NDT = N * 4
IF(NDT .GT. 2000
TRUE
NDT = 2000
FALSE
DT = (T(N) - TI)/NDT
21
NDT = (T(N) - TI) / DT
IF(NDT .GT. 2000
TRUE
NDT = 2000
FALSE
WRITE NDT AND DT
CALL DIGIS
-
IF(J)
+
0
CALL DIGIC
I = 1
F(I) = -F(I)
I = I + 1
FN(I) = I*DT
FN IS FREQUENCY NUMBER
YES
I ≤ NDT
NO
CALL CALFT
CALL STLNFT

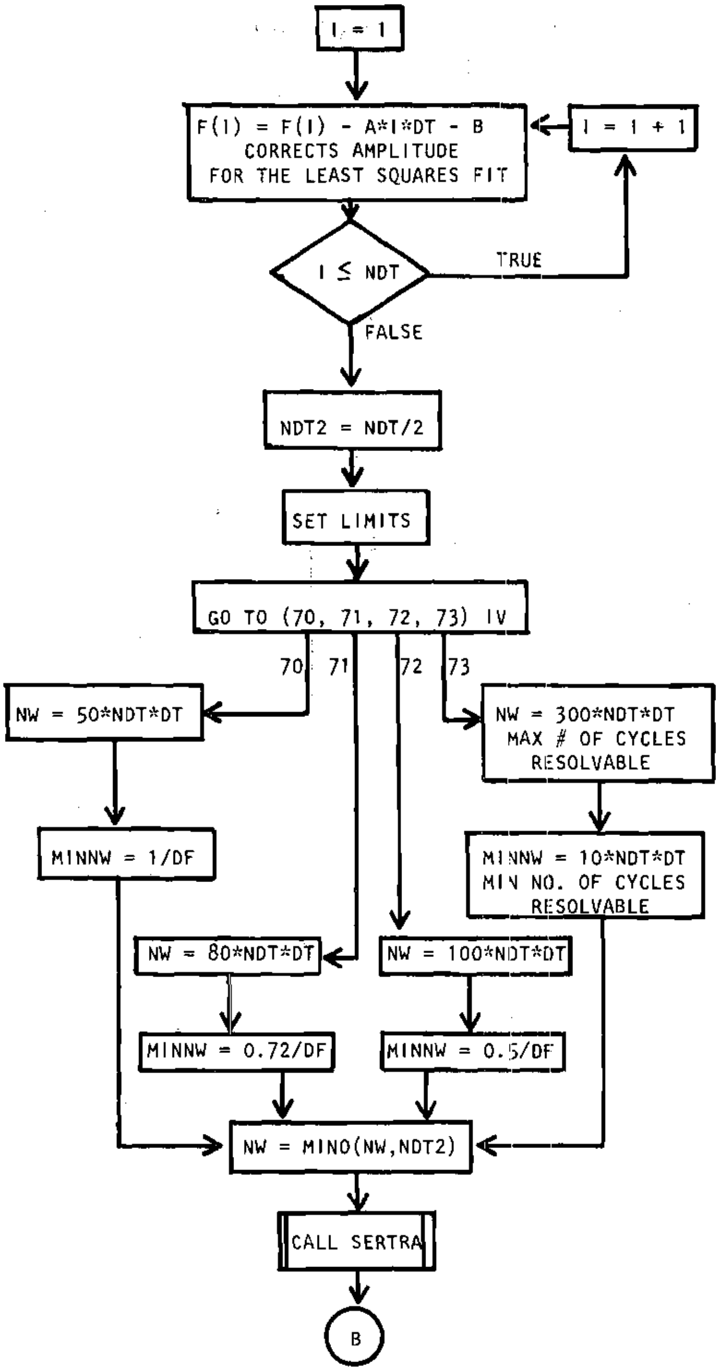
I = 1
F(I) = F(I) - A*I*DT - B
CORRECTS AMPLITUDE
FOR THE LEAST SQUARES FIT
I = I + 1
I ≤ NDT
TRUE
FALSE
NDT2 = NDT/2
SET LIMITS
GO TO (70, 71, 72, 73) IV
70
71
72
73
NW = 50*NDT*DT
MINNW = 1/DF
NW = 300*NDT*DT
MAX # OF CYCLES
RESOLVABLE
MINNW = 10*NDT*DT
MIN NO. OF CYCLES
RESOLVABLE
NW = 80*NDT*DT
MINNW = 0.72/DF
NW = 100*NDT*DT
MINNW = 0.5/DF
NW = MINO(NW,NDT2)
CALL SERTRA
B

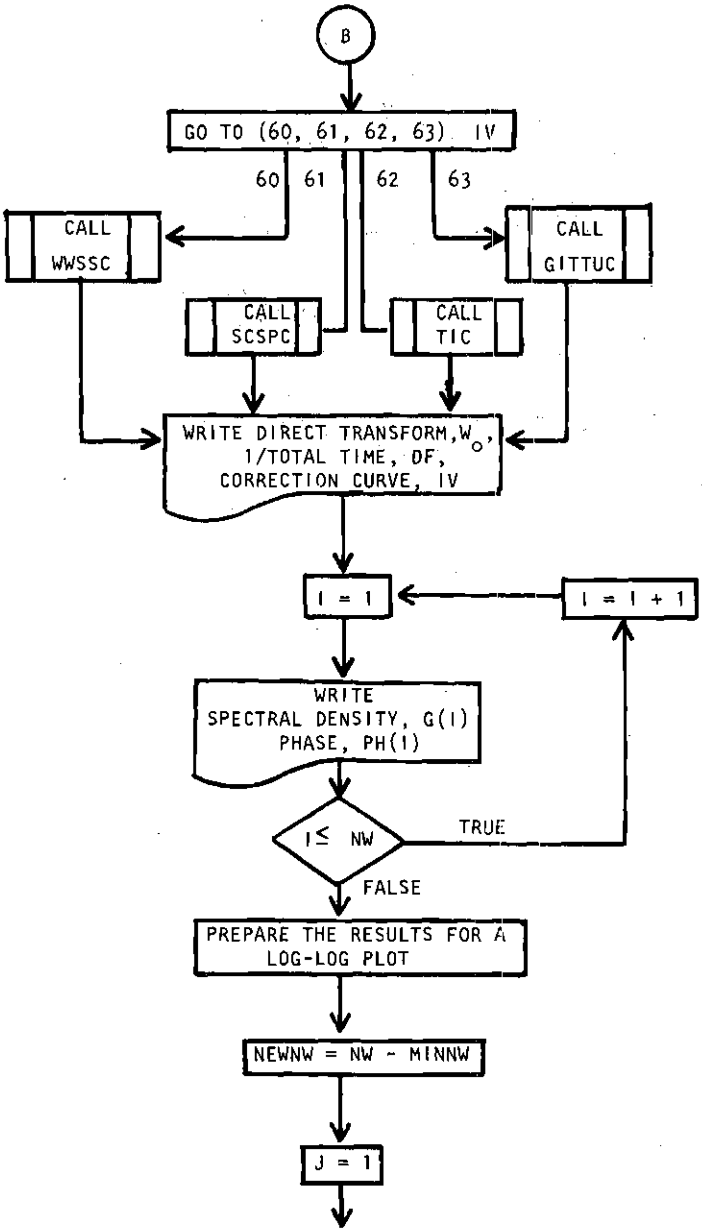
B
GO TO (60, 61, 62, 63) IV
60
61
62
63
CALL WWSSC
CALL SCSPC
CALL TIC
CALL GITTUC
WRITE DIRECT TRANSFORM, W_o, 1/TOTAL TIME, DF, CORRECTION CURVE, IV
I = 1
I = I + 1
WRITE SPECTRAL DENSITY, G(I) PHASE, PH(I)
I ≤ NW
TRUE
FALSE
PREPARE THE RESULTS FOR A LOG-LOG PLOT
NEWNW = NW - MINNW
J = 1

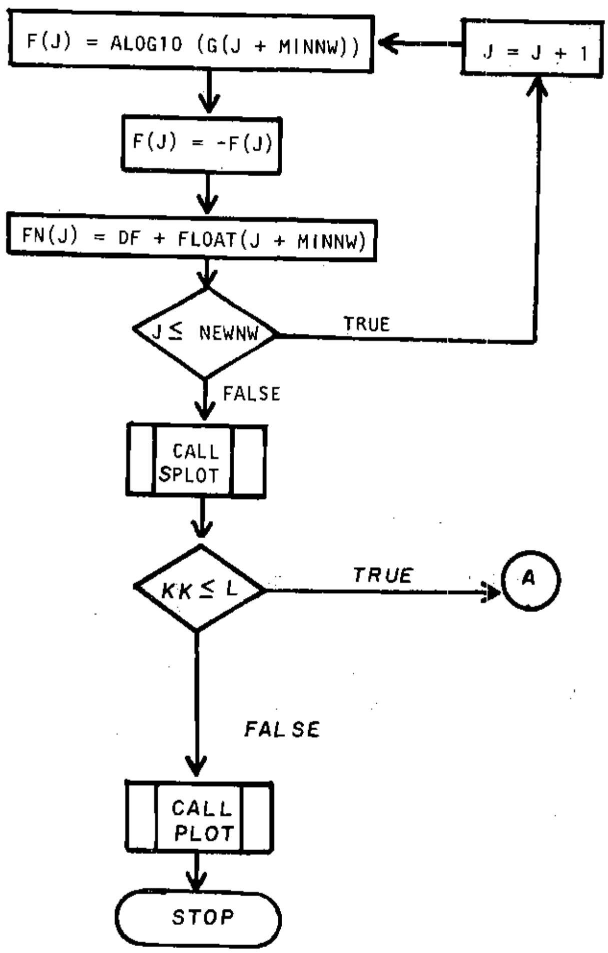
F(J) = ALOG10 (G(J + MINNW))
J = J + 1
F(J) = -F(J)
FN(J) = DF + FLOAT(J + MINNW)
J ≤ NEWNW
TRUE
FALSE
CALL SPLOT
KK ≤ L
TRUE
A
FALSE
CALL PLOT
STOP

```
      PROGRAM MAIN(INPUT,OUTPUT,PUNCH,TAPE5=INPUT,TAPE6=OUTPUT)
C
C
C  THIS PROGRAM CALCULATES AMPLITUDE SPECTRAL DENSITY AS A FUNCTION OF
C  FREQUENCY AND PLOTS THE RESULTS AS A LOG-LOG CALCOMP PLOT.
C
C
C G=SPECTRAL DENSITY (I.E. SPECTRAL AMPLITUDE) IN UNITS OF MM-SEC.
C PH=PHASE.
C T=TIME.
C H=AMPLITUDE OF RAW DATA IN ARBITRARY UNITS.
C F=AMPLITUDE CORRECTED TO UNITS OF VOLTS.
C FN=FREQUENCY NUMBER (I.E. PERIOD) IN UNITS OF TIME.
C NDT2=NDT/2 (I.E. FOLDING FREQUENCY).
C NW=NDT/2 PRIOR TO DEFINING LIMITS.  IT MAY BE CHANGED TO THE
C    MAXIMUM NUMEER OF CYCLES (UPPER LIMIT FOR RESPONSE CURVE CORRECTION)
C MINNW=LOWER LIMIT FOR RESPONSE CURVE CORRECTION IN UNITS OF CYCLES.
C NEWNW=UPPER LIMIT MINUS LOWER LIMIT.  THIS DEFINES THE NUMBER OF
C        POINTS TO BE INCLUDED IN THE LOG-LOG PLOT.
C PLOTS=INITIALIZES THE PLOT PROGRAM.
C IBUFF=THE ARRAY USED TO INITIALIZE THE PLOT PROGRAM.
C FACTOR=USED TO SCALE THE PLOTS TO FIT ON A THESIS PAGE.
C  N= NUMBER OF DATA POINTS
C  NDT = NUMBER OF INTERVALS.   NDT=N-1.
C  DT = TIME INTERVAL BETWEEN READINGS.
C  TI = INITIAL TIME, USUALLY 0.0
C  TCAL = TIME CALIBRATION.
C  HCAL = AMPLITUDE CALIBRATION.
C  LAB = LABEL FOR THE SPECTRUM.
C  IV = CORRECTION CURVE
C       1=WWSSC
C       2=SCSPC
C       3=TIC
C       4=GITTUC
C  J = TYPE OF FIT
C      - OR 0 = PAIRED POINTS
C      + = EQUAL INTERVAL DATA
C  L IS THE NUMBER OF DATA SETS TO BE READ.
C  DF IS THE LOWEST FREQUENCY RESOLVABLE.
C  TTIME IS THE TOTAL TIME INTERVAL.
C   FORMAT  DETERMINES THE FORMAT USED IN READING DATA.
C
C
      DIMENSION G(2000),PH(2000),T(2000),H(2000),F(2002),LAB(3),FN(2002)
      DIMENSION IBUFF(512),FORMAT(8)
C
      CALL PLOTS(IBUFF,512,9,00)
      CALL FACTOR(0.69)
C
C
      READ(5,4) L
    4 FORMAT(I3)
C
      DO 6 KK = 1,L
C
      READ (5,101) N,NDT,DT,TI,TCAL,HCAL,LAB,IV,J
101   FORMAT (2I5,4F10.8,2A10,A6,I1,I2)
C
      IF(EOF(5))999,998
998   CONTINUE
C
      IF(J) 30,30,31
C
   30 WRITE (6,103) N,NDT,DT,TI,TCAL,HCAL,LAB,IV,J
```

```
  103 FORMAT(1H1,I5,44H  PAIRS OF POINTS ARE TO BE INTERPOLATED AT ,I5
     *,7H POINTS,F10.8,14H SECONDS APART,//16H BEGINNING AT T=,F10.3/
     *6H TCAL=, F10.3, 10H UNITS/SEC/6H HCAL=,F10.3,10H VOLT/UNIT//
     *1X,2A10,A6/1X,16HTYPE CORRECTION=,1X,I2/1X,2HJ=,I2/)
C
      GO TO 32
C
   31 WRITE(6,33) N,NDT,DT,TI,TCAL,HCAL,LAB,IV,J
   33 FORMAT (1H1,9X,I5,35H  POINTS ARE TO BE INTERPOLATED AT ,I5
     *,7H POINTS,F10.8,14H SECONDS APART,//16H BEGINNING AT T=,F10.3/
     *6H TCAL=, F10.4, 10H UNITS/SEC/6H HCAL=,F10.8,10H VOLT/UNIT//
     *1X,2A10,A6/1X,16HTYPE CORRECTION=,1X,I2/1X,2HJ=,I2/)
C
   32 TTIME = DT*NDT
      NW = NDT / 2
      DF = 1.0 / TTIME
C
      READ(5,8) FORMAT
    8 FORMAT(8A10)
C
C  THE RAW DATA IS READ INTO THE PROGRAM
C  THE 46 OPTION IS FOR PAIRED POINTS.
C  THE 47 OPTION IS FOR EQUAL INTERVAL DATA.
C
      IF(J) 46,46,47
C
   46 READ(5,FORMAT) (H(I),T(I),I=1,N)
      GO TO 45
   47 READ(5,FORMAT) (H(I),I=1,N)
      T(1) = TI
      DO 5 K=2,N
       T(K)=T(K-1)+DT
    5  CONTINUE
C
C
C  THE RAW DATA IS WRITTEN.
C
   45 WRITE (6,104) (H(I),T(I),I=1,N)
  104 FORMAT(1X, 10F10.3)
C
C  THE RAW DATA IS CORRECTED FOR AMPLITUDE CALIBRATION AND TIME
C  CALIBRATION.
C
      IF(J) 50,50,51
C
   50 DO 52 I = 1,N
       F(I)= H(I) * HCAL
       T(I) =T(I) / TCAL
   52 CONTINUE
      WRITE (6,80)
   80 FORMAT(1H1, "VALUES OF H AND T CORRECTED TO VOLT AND SEC"/)
      WRITE(6,81) (H(I),T(I),I=1,N)
   31 FORMAT(1X,10F10.3)
      GO TO 55
   51 DO 53 I = 1,N
       F(I) = H(I) * HCAL
       T(I) =T(I) / TCAL
   53 CONTINUE
      WRITE(6,180)
  180 FORMAT(1H1, "VALUES OF H AND T CORRECTED TO VOLT AND SEC"/)
      WRITE(6,105) (F(I),T(I),I=1,N)
  105 FORMAT(1X,10F10.3)
C
C  THE TIME INTERVAL IS VERIFIED.
```

```
C
   55 IF(TTIME-T(N)+TI.LE.0.00001) GO TO 54
C
      IF(J) 20,20,21
C
   20 NDT=N*4
      IF(NDT.GT.2000) NDT=2000
      DT = (T(N)-TI)/NDT
      WRITE(6,7) NDT,DT
    7 FORMAT(1X,39HYOUR VALUES OF NDT AND DT ARE IN ERROR.,/1X,56HIT HAS
     * ASSUMED A VALUE OF 4 TIMES N. THE NEW VALUES ARE ,/1X,5HNDT= ,I5,
     *10X,4HDT= ,F10.8)
      GO TO 54
   21 NDT=(T(N)-TI)/DT
      IF(NDT.GT.2000) NDT=2000
      WRITE(6,9) NDT,DT
    9 FORMAT(1X,39HYOUR VALUES OF NDT AND DT ARE IN ERROR.,/1X,68HIT HAS
     * ASSUMED DT TO BE CORRECT AND COMPUTED NDT. THE NEW VALUES ARE ,/
     *1X,5HNDT= ,I5,10X,4HDT= ,F10.8)
C
   54 IF(J) 2,3,600
C
    2 CALL DIGIS (H,T,TI,NDT,DT,F)
      GO TO 600
    3 CALL DIGIC (H,T,TI,NDT,DT,F)
  600 CONTINUE
C
   48 DO 10 I=1,NDT
       F(I)=-F(I)
   10 FN(I)=I*DT
C
C  CALFT DRAWS A TIME AXIS AND THE WAVE FORM.
C  STLNFT DETERMINES A LEAST SQUARES FIT.
C
      CALL CALFT (FN,F,NDT,LAB)
      CALL STLNFT(FN,F,NDT,A,B,SGA,SGB)
C
C  THIS STEP CORRECTS THE AMPLITUDES FOR THE LEAST SQUARES FIT.
      DO 11 I=1,NDT
   11 F(I)=F(I)-A*I*DT-B
C
C  THIS SECTION SETS THE LIMITS ACCORDING TO THE FREQUENCY RESPONSE
C  OF THE INSTRUMENT USED.
C
      NDT2=NDT/2
C
      GO TO (70,71,72,73),IV
C
   70 NW=50*NDT*DT
      MINNW=.1/DF
      GO TO 79
   71 NW=80*NDT*DT
      MINNW=.72/DF
      GO TO 79
   72 NW=100*NDT*DT
      MINNW=.5/DF
      GO TO 79
   73 NW=300.*NDT*DT
      MINNW=10.*NDT*DT
C
   79 NW=MIN0(NW,NDT2)
C
C  SERTRA CALCULATES THE AMPLITUDE SPECTRAL DENSITY.
      CALL SERTRA(0.0,NDT,NW,DF,G,PH,WO,F)
```

```
C
C  THE FOLLOWING SECTION IS USED TO CORRECT THE AMPLITUDE SPECTRAL
C  DENSITY FOR THE DISPLACEMENT RESPONSE OF THE TOTAL SYSTEM.
C
      GO TO (60,61,62,63),IV
C
   60 CONTINUE
      CALL WWSSC(NW,DF,G,PH)
       GO TO 602
   61 CONTINUE
      CALL SCSFC (NW,DF,G,PH)
       GO TO 602
   62 CONTINUE
      CALL TIC (NW,DF,G,PH)
      GO TO 602
   63 CONTINUE
      CALL GITTUC (NW,DF,G,PH)
C
  602 CONTINUE
C
C  THIS SECTION WRITES THE RESULTS.
C
      WRITE(6,112) WO,DF,IV,(G(I),PH(I), I=1,NW)
  112 FORMAT(17H DIRECT TRANSFORM,6H WO = ,E14.7/4H DF=,E14.7/
     *18H CORRECTION TYPE =,I2//1X,17HMODULUS AND PHASE/1X,5(E15.6,F10.2
     *))
C
C  THIS SECTION PREPARES THE SPECTRAL RESULTS FOR A LOG-LOG PLOT.
C
      NEWNW= NW-MINNW
C
      DO 12 J=1,NEWNW
      F(J)=ALOG10(G(J+MINNW))
      F(J)=-F(J)
   12 FN(J)=DF*FLOAT(J+MINNW)
C
      CALL SPLOT (F,FN,NEWNW,LAB)
C
    6 CONTINUE
C
      CALL PLOT(5.0,-1.0,999)
C
C
  999 STOP
      END
```

```
      SUBROUTINE DIGIS (H,T,TI,NDT,DT,F)
C
C     SUBROUTINE FOR STRAIGHT LINE FIT
C
      DIMENSION H(2000),T(2000),F(2002)
      PI=3.1415926536
      I=0
      DO 20 J=1,NDT
      TIME=TI + (J-1)*DT
   22 IF (T(I+1).GT.TIME) GO TO 20
      I=I+1
      GO TO 22
   20 F(J)=H(I)+(TIME-T(I))*(H(I+1)-H(I))/(T(I+1)-T(I))
      RETURN
      END


      SUBROUTINE DIGIC (H,T,TI,NDT,DT,F)
C
C     SUBROUTINE FOR COS FIT
C
      DIMENSION H(2000),T(2000),F(2002)
      PI=3.1415926536
      I=0
      DO 20 J=1,NDT
      TIME=TI + (J-1)*DT
   22 IF (T(I+1).GT.TIME) GO TO 20
      I=I+1
      GO TO 22
   20 F(J)=(H(I)+H(I+1))*0.5+(H(I)-H(I+1))*0.5*COS(PI*(TIME-T(I))/(T(I+1
     C)-T(I)))
      RETURN
      END


      SUBROUTINE CALFT (FN,F,NDT,LAB)
C
C THIS SUBROUTINE PLOTS A TIME AXIS AND RECONSTRUCTS THE WAVE FORM.
C
      DIMENSION FN(2002),F(2002),LAB(3)
C
C SET THE ORIGIN TO THE LEFT EDGE OF THE PAGE.
      CALL PLOT(2.0,-10.0,-3)
C
C SET THE ORIGIN 3 INCHES FROM THE LEFT EDGE OF THE PAGE.
      CALL PLOT(0.0,+3.0,-3)
C
C WRITE THE LABEL.
      CALL SYMBOL (-1.0,0.0,0.14,LAB,90.,26)
C
C SCALE THE AMPLITUDE AND TIME TO FIT THE SPACE ALLOWED.
      CALL SCALE (F(1),2.0,NDT,+1)
      CALL SCALE (FN(1),5.0,NDT,+1)
C
C DRAW THE WAVE.
      CALL LINE(F(1),FN(1),NDT,+1,40,3)
C
C DRAW AND LABEL A TIME AXIS.
      CALL AXIS(0.0,0.0,7HSECONDS, 7,5.0,90.,FN(NDT+1),FN(NDT+2))
C
C RESET ORIGIN FOR USE BY SPLOT.
      CALL PLOT (2.0,0.0,-3)
      RETURN
      END
```

```
      SUBROUTINE STLNFT(X,Y,N,A,B,SGA,SGB)
C
C X=FN (I.E. PERIOD)
C Y=F (I.E. AMPLITUDE).
C N=NOT.
C A=SLOPE
C B=Y-INTERCEPT
C SGA=ERROR IN CALCULATING A
C SGB=ERROR IN CALCULATING B.
C SX=THE SUMMATION OF X FROM 1 TO N.
C SXX=THE SUMMATION OF X-SQUARE FROM 1 TO N.
C SY=THE SUMMATION OF Y FROM 1 TO N.
C SYY=THE SUMMATION OF Y-SQUARE FROM 1 TO N.
C SXY=THE SUMMATION OF X*Y FROM 1 TO N.
C
      DIMENSION X(N), Y(N)
      SX =0.0
      SXX =0.0
      SY =0.0
      SYY =0.0
      SXY =0.0
C
      DO 325 I=1,N
       SX = SX + X(I)
       SXX = SXX + X(I)*X(I)
       SY = SY + Y(I)
       SYY =SYY +Y(I)*Y(I)
       SXY = SXY +X(I)*Y(I)
  325 CONTINUE
C
      AN = N
      DNOM = AN*SXX -SX*SX
      A = (AN*SXY -SX*SY)/DNOM
      B = (SY*SXX - SX*SXY)/DNOM
      D2 = SYY -A*SXY-B*SY
      SGA = SQRT (AN*D2/(DNOM*(AN-2.)))
      SGB = SQRT(SX*SX*D2/(DNOM*(AN-2.)))
      D2=SQRT(D2/AN)
C
      WRITE(6,326) A,SGA,B,SGB,D2
  326 FORMAT (//30H LEAST SQUARE FIT, Y = A*X + B/3H A=,E12.6,5H +OR-,
     1E12.6/3H B=,E12.6,5H +OR-,E12.6/1X,14HMIN DEVIATION=,E12.6)
C
      RETURN
      END


      SUBROUTINE SERTRA(DET,N,NW,DF,G,PH,WO,T)
C
C DET=A CONSTANT USED TO DETERMINE THE TRANSFORMATION.
C       DET=0.0 SIGNIFIES A TRANSFORMATION FROM THE TIME DOMAIN TO THE
C       FREQUENCY DOMAIN.
C       DET=ANY VALUE OTHER THAN ZERO SIGNIFIES
C       AN INVERSE TRANSFORMATION.
C N=NOT=NUMBER OF DIVISIONS.
C NW=NOT/2=FOLDING FREQUENCY.
C DF=1/TOTAL TIME.
C G=SPECTRAL DENSITY IN UNITS OF MM-SEC RETURNED TO THE MAIN PROGRAM.
C PH=PHASE.
C WO=DIRECT TRANSFORM.
C T=F=AMPLITUDE CORRECTED TO UNITS OF VOLTS.
C X=FOURIER COSINE TRANSFORMATION
C Y=FOURIER SINE TRANSFORMATION.
C ATAN2(-Y,-X)=THE PHASE ANGLE BETWEEN THE COSINE AND SINE TRANSFORMS.
C
```

```
      DIMENSION G(NW),PH(NW),T(N),CFN(2000),SFN(2000)
      PI = 3.1415926536
      CF = 0.0174532925
      AN = N
C
      DO 119 I = 1,N
       A = I
       ARG = (6.28318531*A)/AN
       SFN(I) = SIN(ARG)
  119 CFN(I) = COS(ARG)
      IF (DET) 131,132,131
C
  132 DO 133 I = 1,NW
       G(I) = 0.0
  133 PH(I) = 0.0
C
      WO = 0.0
      DO 139 J = 1,NW
       X = 0.0
       Y = 0.0
       DO 140 I = 1,N
        IJ = I*J - N*((I*J-1)/N)
        X = X + T(I)*CFN(IJ)
  140  Y = Y - T(I)*SFN(IJ)
       PH(J)=(ATAN2(-Y,-X))/CF +180.
  139 G(J) = (1.0/(AN*DF*6.28318531))*SQRT(X*X + Y*Y)
C
      DO 134 I = 1,N
  134 WO = WO +T(I)
C
      WO = (1.0/(AN*DF*6.28318531))*WO
      WRITE(6,112) WO,DF, (G(I),PH(I), I = 1,NW)
  112 FORMAT(//17H DIRECT TRANSFORM,6H WO = ,E14.7/6H DF = ,E14.7//
     *18H MODULUS AND PHASE/ (1X,E15.6,F10.2,E15.6,F10.2,E15.6,F10.2,
     *E15.6,F10.2,E15.6,F10.2))
       RETURN
C
  131 DO 142 I = 1,N
  142  T(I) = WO/2.0
      DO 143  J = 1,NW
       NSG = (PH(J)/360.)*AN
      DO 143 I = 1,N
       IJ = I*J + NSG -N*((I*J + NSG - 1)/N)
  143 T(I) =T(I) + G(J)*CFN(IJ)
      DO 144 I = 1,N
  144 T(I) = 12.5663706*DF*T(I)
      DT = (1.0)/(AN*DF)
       RETURN
       END


      SUBROUTINE WWSSC(NW,DF,G,PH)
C
C WORLD WIDE SEISMIC SYS. CORRECTION FROM FREQ RESPONSE CURVE
C WWSSC (NW,G,DF,ISTART,ISTOP)
C NW=NO. OF PTS. IN SPECTRUM
C G=MODULUS OF SPECTRUM
C DF=FREQ INCREMENT  1/T
C T=TOTAL TIME
C  SEE SUBROUTINE GITTUC FOR FURTHER DETAILS.
C
      DIMENSION GCOR(11),FREQ(11),G(NW),PH(NW)
      DATA GCOR/.65,300.0,400.0,540.0,580.0,610.0,590.0,480.0,
     *310.0,38.0,1.8/
```

```
      DATA FREQ/.1,.8,1.0,1.25,1.43,1.67,2.00,2.50,
     *3.33,10.0,50.0/
      FMIN=0.1
      FMAX=50.0
      IF(DF.LT.0.1) GO TO 7
      FMIN=DF
    7 IF(NW*DF.GT.FMAX) GO TO 8
      FMAX=NW*DF
    8 ISTART=FMIN/DF+0.00001
      ISTOP=FMAX/DF
      NW=ISTOP
      J=1
      DO 18 I=ISTART,ISTOP
      FQ=I*DF
   40 IF(FQ.LT.FREQ(J)) GO TO 42
      J=J+1
      GO TO 40
   42 VAL=GCOR(J-1)+(GCOR(J)-GCOR(J-1))*(FQ-FREQ(J-1))/
     *(FREQ(J)-FREQ(J-1))
      G(I)=G(I)/VAL
   18 CONTINUE
      WRITE(6,1066) ISTART,ISTOP,DF
 1066 FORMAT(1H1,55HDATA CORRECTED FOR DISPLACEMENT RESPONSE BETWEEN IST
     *ART,I5,3H*DF,10HAND ISTOP ,I5,3H*DF,/6H DF = ,F8.3)
      RETURN
      END


      SUBROUTINE SCSPC (NW,DF,G,PH)
C
C  SOUTH CAROLINA SEISMIC PROGRAM, FROM DISPLACEMENT RESPONSE CURVE.
C  CORRECTION FOR STATIONS SGS,JKS OF THE SOUTH CAROLINA NET
C  SEE SUBROUTINE GITTUC FOR FURTHER DETAILS.
C
      DIMENSION GSOR(18),FRES(18),G(NW),PH(NW)
      DATA FRES/.72,.8,.9,1.,1.2,2.0,3.,5.,7.,10.,14.,20.,
     *30.,40.,50.,60.,70.,80./
      DATA GSOR/20.,22.,30.,38.,72.,120.,180.,310.,420.,580.,
     *790.,1010.,1050.,1075.,1080.,1067.,1060.,1020./
      FMIN=0.72
      FMAX=80.0
      IF(DF.LT.0.72) GO TO 7
      FMIN=DF
    7 IF(NW*DF.GT.FMAX) GO TO 8
      FMAX=NW*DF
    8 ISTART=FMIN/DF +0.00001
      ISTOP=FMAX/DF
      NW=ISTOP
      J=1
      DO 18 I=ISTART,ISTOP
      FQ=I*DF
   40 IF(FQ.LT.FRES(J)) GO TO 42
      J=J+1
      GO TO 40
   42 VAL=GSOR(J-1)+(GSOR(J)-GSOR(J-1))*(FQ-FRES(J-1))/
     *(FRES(J)-FRES(J-1))
   18 G(I)=G(I)/VAL
      WRITE(6,1066) ISTART,ISTOP,DF
 1066 FORMAT(1H1,55HDATA CORRECTED FOR DISPLACEMENT RESPONSE BETWEEN IST
     *ART,I5,3H*DF,10HAND ISTOP ,I5,3H*DF,/6H DF = ,F8.3)
      RETURN
      END
```

```
      SUBROUTINE TIC (NW,DF,G,PH)
C
C  GEORGIA TECH CORRECTION PROGRAM FOR THE HALL-SEARS SYSTEMS.
C  DERIVED FRCM DISPLACEMENT RESPONSE CURVES.
C  SEE SUBROUTINE GITTUC FOR FURTHER DETAILS.
C
      DIMENSION GTOR(23),FRET(23),G(NW),PH(NW)
C
      DATA FRET/.5,.75,1.0,1.25,1.5,1.75,2.0,2.5,3.0,4.0,5.0,
     *7.5,10.0,15.0,20.,30.,40.,50.,60.,70.,80.,90.,100./
C
      DATA GTOR/6.6,23.6,50.9,78.3,111.2,135.2,161.0,204.6,
     *253.,343.,435.,653.,871.,1306.,1689.,2454.,3061.,
     *3695.,4117.,4433.,4750.,5106.,5278./
C
      FMIN=0.50
      FMAX=100.0
      IF(DF.LT.0.50) GO TO 7
      FMIN=DF
    7 IF(NW*DF.GT.FMAX) GO TO 8
      FMAX=NW*DF
    8 ISTART=FMIN/DF +0.00001
      ISTOP=FMAX/DF
      NW=ISTOP
C
      J=1
      DO 18 I=ISTART,ISTOP
      FQ=I*DF
   40 IF(FQ.LT.FRET(J)) GO TO 42
      J=J+1
      GO TO 40
   42 VAL=GTOR(J-1)+(GTOR(J)-GTOR(J-1))*(FQ-FRET(J-1))/
     *(FRET(J)-FRET(J-1))
   18 G(I)=G(I)/VAL
C
      WRITE(6,1066) ISTART,ISTOP,DF
 1066 FORMAT(1H1,55HDATA CORRECTED FOR DISPLACEMENT RESPONSE BETWEEN IST
     *ART,I5,3H*DF,10HAND ISTOP ,I5,3H*DF,/6H DF = ,F8.3)
      RETURN
      END


      SUBROUTINE GITTUC (NW,DF,G,PH)
C GEORGIA INSTITUTE OF TECHNOLOGY TAPE UNIT CORRECTION
C DERIVED FROM DISPLACEMENT RESPONSE CURVES FOR THE TOTAL SYSTEM.
C       INPUT UNITS ARE VOLT-SEC
C       OUTPUT UNITS ARE MM-SEC
C  PH = PHASE
C
      DIMENSION GSOR(19),FRES(19),G(NW),PH(NW)
C
C  DATA REFERS TO THE DIGITIZED VALUES OF THE INSTRUMENT RESPONSE CURVE.
C
C  GSOR IS DISPLACEMENT IN VOLT/MM.
      DATA GSOR/163.0,2639.0,8482.0,13331.0,24192.0,38026.0,50768.0,
     *58610.0,70372.0,106500.0,127235.0,150796.0,154000.0,154566.0,
     *153000.0,145000.0,124407.0,102102.0,58434.0/
C
C  FRES IS FREQUENCY IN HZ.
      DATA FRES/10.0,15.0,18.0,20.5,27.0,34.0,40.0,44.0,50.0,75.0,
     *90.0,125.0,140.0,150.0,160.0,175.0,200.0,250.0,300.0/
```

```
C
C MINIMUM FREQUENCY TO WHICH THE TOTAL SYSTEM WILL RESPOND.
      FMIN=10.0
C MAXIMUM FREQUENCY TO WHICH THE TOTAL SYSTEM WILL RESPOND.
      FMAX=300.0
C
C  THIS SECTION PREVENTS THE CALCULATION OF SPECTRA OUTSIDE THE
C  RESOLVABLE RANGE OF THE INSTRUMENTS AND/OR OF THE DIGITIZING
C  INTERVAL.
      IF(DF.LT.10.0) GO TO 7
      FMIN=DF
    7 IF(NW*DF.GT.FMAX) GO TO 8
      FMAX=NW*DF
    8 ISTART=FMIN/DF +0.00001
      ISTOP=FMAX/DF
      NW=ISTOP
      J=1
C
      DO 18 I=ISTART,ISTOP
       FQ=I*DF
   40  IF(FQ.LT.FRES(J)) GO TO 42
       J=J+1
       GO TO 40
   42  VAL=GSOR(J-1)+(GSOR(J)-GSOR(J-1))*(FQ-FRES(J-1))/
     * (FRES(J)-FRES(J-1))
   18 G(I)=G(I)/VAL
C
      WRITE(6,1066) ISTART,ISTOP,DF
 1066 FORMAT(1H1,55HDATA CORRECTED FOR DISPLACEMENT RESPONSE BETWEEN IST
     *ART,I5,3H*DF,10HAND ISTOP ,I5,3H*DF,//6H DF = ,F8.3)
C
      RETURN
      END


      SUBROUTINE SPLOT (F,FN,NW,LAB)
C
C SPLOT IS THE SPECTRAL PLOT SUBROUTINE.
C SPLOT DRAWS LOG-LOG AXES AND PLOTS THE DATA.
C F = AMPLITUDE SPECTRAL DENSITY
C FN = FREQUENCY NUMBER
C THE PLOTS ARE SCALED TO A COMMON SIZE.
C
      DIMENSION FN(2002),F(2002),LAB(3)
C
C THIS SETS THE ORIGIN AT THE FAR LEFT EDGE OF THE PAPER.
      CALL PLOT(1.0,-10.0,-3)
C THIS MOVES THE ORIGIN 3 INCHES ALONG THE Y-AXIS.
      CALL PLOT(0.0,+3.0,-3)
C
C THIS OBTAINS A MINIMUM AND MAXIMUM VALUE OF AMPLITUDE.
      AMIN = F(1)
      FMAX=F(1)
      DO 1 I=2,NW
      AMIN = AMIN1(AMIN,F(I))
      FMAX=AMAX1(FMAX,F(I))
1     CONTINUE
C
C THIS CALCULATES THE NUMBER OF LOG CYCLES NEEDED FOR THE
C SPECTRAL DENSITY (I.E. AMPLITUDE) AXIS.
      IMIN = AMIN
      CYCLES=IFIX(FMAX)-IMIN+1.
      AXLENG=6.6
      RESET=AXLENG+4.0
C
```

```
C THIS OBTAINS A REFERENCE VALUE FOR LABELING THE SPECTRAL DENSITY AXIS
      N=-1*(IFIX(FMAX)+1)
C LGSCAL SCALES THE LINEAR DATA FOR A LOG10 PLOT.
      CALL LGSCAL(FN,6.,NW,1)
      F(NW+1)=IMIN
C LENGTH PER CYCLE IN INCHES
      F(NW+2)=CYCLES/AXLENG
C LGLINE DRAWS THE SPECTRUM OF F VS FN FOR NW POINTS PRODUCING
C A + MARK EVERY 40 POINTS.
      CALL LGLINE(F,FN,NW,1,40,3,1)
C REFERENCE VALUE FOR LABELING THE FIRST CYCLE
      F(NW+1)=10.**N
C LGAXIS DRAWS THE LOG10 AXIS FOR FREQUENCY ADJUSTED TO THE RESPONSE
C RANGE BY FN(NW+1) AND FN(NW+2).
      CALL LGAXIS (0.0,+0.0,2HHZ,+2,6.0,90.,FN(NW+1),FN(NW+2))
C LGAXIS DRAWS THE LOG10 AXIS FOR THE SPECTRAL DENSITY.
      CALL LGAXIS(AXLENG,0.0,8HDIS SPEC,+8,AXLENG,180.0,
     *F(NW+1),F(NW+2))
C MOVES THE ORIGIN IN PREPERATION FOR THE NEXT PLOT.
      CALL PLOT (RESET,0.0,-3)
C
      RETURN
      END
```

APPENDIX I

STRIPCHARTS OF MICROEARTHQUAKES

The characteristics of microearthquakes can often be identified from their "signatures" or wave traces. Figure 36 shows three extremely small microearthquakes from the CHRA. The data have been played onto one channel and time pulses have been played onto the other channel. This trace was made with the stripchart running at 25 mm/sec. Figure 37 shows a very similar event which was recorded at 125 mm/sec. Note the improved resolution. Note the extreme similarity of the general shape of the spectra in Figure (36) and (37). This similarity suggests that the events passed along similar propagation paths after being produced by similar sources. Figure 38 shows a CHRA microearthquake that is decidedly different from those of Figure 36 and 37. Figure 39 shows a microearthquake played onto both channels at different amplitude settings. A great majority of the wave traces from the CHRA and the JRA are very similar to one of these four traces.

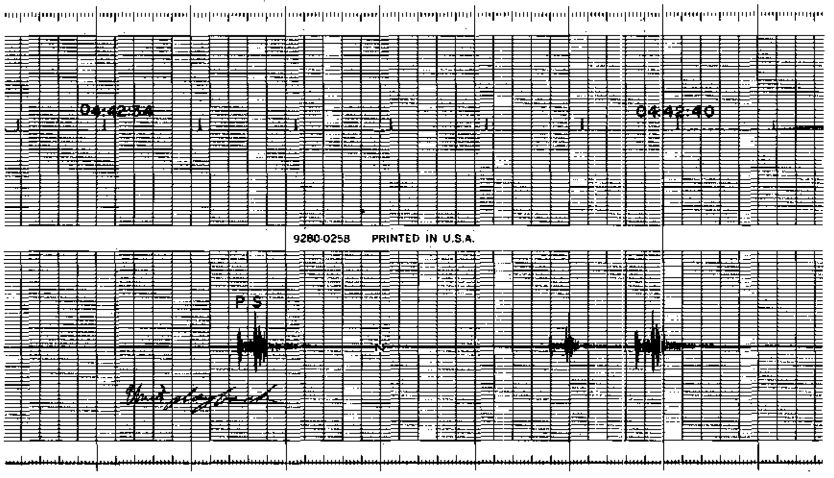

Figure 36. Stripchart Showing Seismic Data and Time Marks. (Stripchart for numbers 15 - 20 of Table 1.)

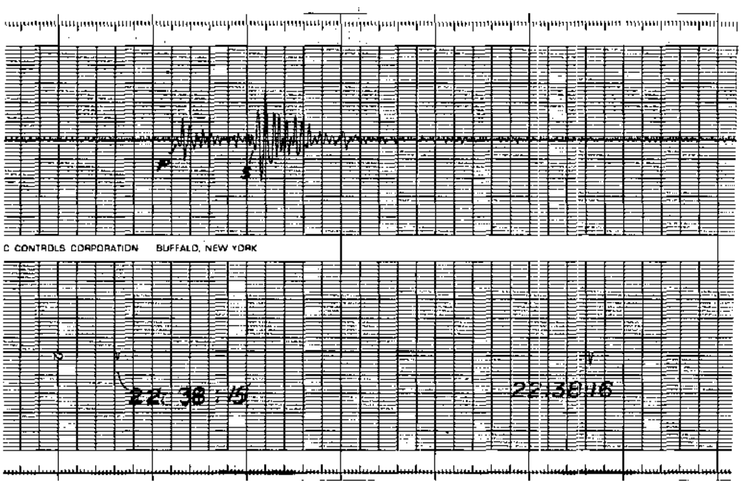

Figure 37. Stripchart Showing Improved Resolution of Faster Recording Speed.

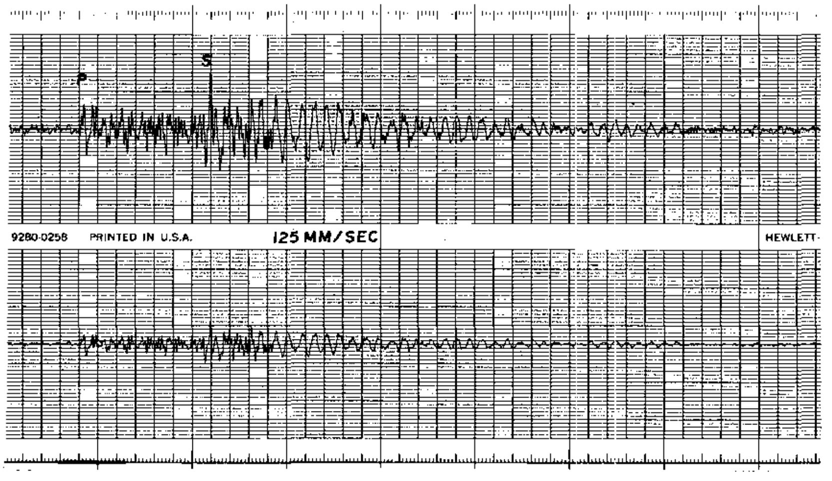

Figure 38. A Representative CHRA Microearthquake Played at Different Gains.

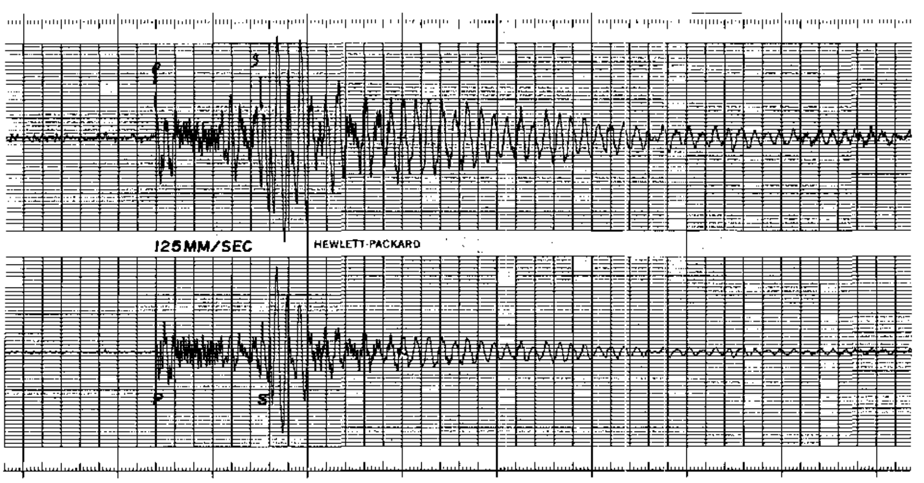

Figure 39. A Representative CHRA Microearthquake Played at Different Gains.

BIBLIOGRAPHY

Aki, Keiti (1967). Scaling law of seismic spectrum. J. Geophys. Res., 72(4), 1217-1231.

Archambeau, C. B. (1968). General theory of elastodynamic source fields. Rev. Geophys., 6(3), 241-288.

Bakun, W. H., C. G. Bufe, and R. M. Stewart (1976). Body-wave spectra of central California earthquakes. Bull. Seismol. Soc. Am., 66(2), 363-384.

Beers, Yardley (1958). Introduction to the Theory of Error. Addison-Wesley Publishing Company, Inc., pp. 9-35.

Bollinger, G. A., C. J. Langer, and S. T. Harding (1976). The eastern Tennessee earthquake sequence of October through December, 1973. Bull. Seismol. Soc. Am., 66(2), 525-547.

Bridges, S. R. (1975). Evaluation of Stress Drop of the August 2, 1974 Georgia-South Carolina Earthquake and Aftershock Sequence. Georgia Institute of Technology, 103 pages.

Brune, James N. (1970). Tectonic stress and the spectra of seismic shear waves from earthquakes. J. Geophys. Res., 75(26), 4997-5009.

Brune, James N. (1971). Correction. J. Geophys. Res. 76(20), p. 5002.

Brune, J. N., and C. R. Allen (1967). Low stress drop, low magnitude earthquake with surface faulting: the Imperial, California, earthquake of March 4, 1966. Bull. Seismol. Soc. Am., 57(3), 501-514.

Burridge, R. (1975). The effect of sonic rupture on the ratio of S- to P-corner frequencies. Bull. Seismol. Soc. Am., 65, 667-675.

Burridge, R., and G. S. Halliday (1971). Dynamic shear cracks with friction as models for shallow focus earthquakes. Geophys. J. R. astr. Soc., 25, 261-283.

Burridge, R., and L. Knopoff (1964). Body force equivalents for seismic dislocations. Bull. Seismol. Soc. Am., 54(6), 1875-1888.

Burridge, Robert, and Cesar Levy (1974). Self-similar circular shear cracks lacking cohesion. Bull. Seismol. Soc. Am., 64(6), 1809-1824.

Chowns, T. M. (1976). Introduction. Stratigraphy, Structure, and Seismicity in Slate Belt Rocks Along the Savannah River. Georgia Geological Society, Guidebook 16, pp. 2-8.

Churchill, Ruel V. (1972). Operational Mathematics. Third edition, McGraw-Hill, pp. 348-355.

Dahlen, F. A. (1974). On the ratio of P-wave to S-wave corner frequencies for shallow earthquake sources. Bull. Seismol. Soc. Am., 64(4), 1159-1180.

Denman, H. E., Jr. (1974). Implications of Seismic Activity at the Clark Hill Reservoir. Georgia Institute of Technology.

Dobrin, M. B. (1960). Introduction to Geophysical Prospecting. Second edition, McGraw-Hill, pp. 20-21.

Douglas, B. M., and Alan Ryall (1972). Spectral characteristics and stress drop for microearthquakes near Fairview Peak, Nevada. J. Geophys. Res., 77(2), 351-359.

Fogle, G. H., R. M. White, A. F. Benson, L. T. Long, and G. F. Sowers (1976). Reservoir induced seismicity at Lake Jocassee, northwestern South Carolina. EOS Trans., Am. Geophys. Union, 57(10), 759.

Fossum, A. F., and L. B. Freund (1975). Nonuniformly moving shear crack model of a shallow focus earthquake mechanism. J. Geophys. Res., 80(23), 3345-3347.

Hanks, T. C., and Max Wyss (1972). The use of body-wave spectra in the determination of seismic-source parameters. Bull. Seismol. Soc. Am., 62(2), 561-589.

Haskell, N. A. (1964). Total energy and energy spectra density of elastic wave radiation from propagating faults. Bull. Seismol. Soc. Am., 54(6), 1811-1841.

Hocking, John G. (1970). Calculus with an Introduction to Linear Algebra. Holt, Rinehart, and Winston, Inc., p. 557.

Housner, G. W., and M. D. Trifunac (1967). Analysis of accelerograms: Parkfield earthquake. Bull. Seismol. Soc. Am., 57(6), 1193-1220.

Hsiao, Helmut Y. A. (1977). The Stress Amplification Mechanism for Intraplate Earthquakes Applied to Southeast United States. Georgia Institute of Technology, in preparation.

Johnson, L. R., and T. V. McEvilly (1974). Near-field observations and source parameters of central California earthquakes. Bull. Seismol. Soc. Am., 64, 1855-1886.

Kanasewich, E. R. (1975). Time Sequence Analysis in Geophysics. Second edition, University of Alberta Press, 364 pages.

Keilis-Borok, V. I. (1959). On estimation of the displacement in an earthquake source and of source dimensions. Ann. Geofis., 12, 205-214.

Keilis-Borok, V. I. (1960). Investigation of the mechanism of earthquakes. Sov. Res. Geophys., 201 pages.

Lighthill, M. J. (1958). Introduction to Fourier Analysis and Generalized Functions. Cambridge University Press, pp. 54-55.

Long, L. T., and H. Y. A. Hsiao (1976). The "stress amplification" mechanism for intraplate earthquakes applied to the southeast United States. Geol. Soc. Am., abstracts with programs, Northeastern/Southeastern Sections, p. 221.

Madariaga, Raul (1976). Dynamics of an expanding circular fault. Bull. Seismol. Soc. Am. 66(3), 639-666.

Marion, Jerry B. (1970). Classical Dynamics of Particles and Systems. Second edition, Academic Press, pp. 94-95.

Mark Products, Inc. (1975). Specifications: L-4C 5500.

McGarr, A. (1976). Seismic moments and volume changes. J. Geophys. Res., 81(8), 1487-1494.

Mogi, Kiyoo (1973). Rock fracture. Annual Rev. of Earth and Planetary Sci., 1, 63-84.

Molnar, Peter, B. E. Tucker, and J. N. Brune (1973). Corner frequencies of P- and S-waves and models of earthquake sources. Bull. Seismol. Soc. Am., 63(6), 2091-2104.

Overstreet, W. C., and Henry Bell, III (1961). Provisional geologic map of the crystalline rocks of South Carolina. U. S. Geol. Survey, map.

Paris, T. A. (1976). The Geology of the Lincolnton 7.5' Quadrangle. University of Georgia, 191 pages.

Raisz, Erwin (1970). Physiography. Goode's World Atlas. Thirteenth edition, Rand McNally Co., pp. 60-61.

Randall, M. J. (1964). Seismic energy generated by a sudden volume change. Bull. Seismol. Soc. Am., 54(5), 1291-1298.

Randall, M. J. (1966). Seismic radiation from a sudden phase transition. J. Geophys. Res., 71(22), 5297-5302.

Randall, M. J. (1973A). Spectral peaks and earthquake source dimensions. J. Geophys. Res., 78(14), 2609-2611.

Randall, M. J. (1973B). The spectral theory of seismic sources. Bull. Seismol. Soc. Am., 63(3), 1133-1144.

Savage, J. C. (1965). The stopping phase on seismograms. Bull. Seismol. Soc. Am., 55(1), 47-58.

Savage, J. C. (1966A). Radiation from a realistic model of faulting. Bull. Seismol. Soc. Am., 56(2), 577-592.

Savage, J. C. (1966B). Thermoelastic attenuation of elastic waves by cracks. J. Geophys. Res., 71(16), 3929-3938.

Savage, J. C. (1972). Relation of corner frequency to fault dimensions. J. Geophys. Res., 77(20), 3788-3795.

Savage, J. C. (1974). Relation between P- and S-wave corner frequencies in the seismic spectrum. Bull. Seismol. Soc. Am., 64(6), 1621-1627.

Scheffler, P. K. (1976). The McCormick County, South Carolina, Earthquake of 2 August, 1974: Geological and Geophysical Investigations. University of South Carolina, 65 pages.

Thatcher, Wayne, and Hanks, T. C. Source parameters of southern California earthquakes. J. Geophys. Res., 78(35), 8547-8576.

Tucker, B. E., and J. N. Brune (1973). Seismograms, S-wave spectra, and source parameters for aftershocks of San Fernando earthquake. San Fernando, California, Earthquake of February 9, 1971. NOAA Publication, Vol. 3, pp. 69-121.

Walsh, J. B. (1966). Seismic wave attenuation in rocks due to friction. J. Geophys. Res., 71(10), 2591-2599.

White, J. E. (1965). Seismic Waves: Radiation, Transmission, and Attenuation. McGraw-Hill, pp. 222-223.

Wu, Francis Taming (1966). Lower Limit of the Total Energy of Earthquakes and Partitioning of Energy Among Seismic Waves. California Institute of Technology, 251 pages.

Wyss, Max, and Brune, J. N. (1968). Seismic moment, stress, and source dimensions for earthquakes in the California-Nevada region. J. Geophys. Res., 73(14), 4681-4694.